ARL-CR-0767 • MAR 2015

US Army Research Laboratory

US Army Research Laboratory Materials Center of Excellence

Dynamic Behavior and Optimization of Advanced Armor Ceramics: January–December 2012 Annual Report

edited by RA Haber
Recipient Program Manager
Director, Center for Ceramic Research
Rutgers, The State University of New Jersey
607 Taylor Road, Piscataway, NJ 08854-8065

and

JW McCauley (Emeritus)
Cooperative Agreement Manager
US Army Research Laboratory
Weapons and Materials Research Directorate, ARL
Aberdeen Proving Ground, MD 21005-5066

under contract W911NF-06-2-0007

NOTICES

Disclaimers

The findings in this report are not to be construed as an official Department of the Army position unless so designated by other authorized documents.

Citation of manufacturer's or trade names does not constitute an official endorsement or approval of the use thereof.

Destroy this report when it is no longer needed. Do not return it to the originator.

ARL-CR-0767 ● MAR 2015

US Army Research Laboratory

US Army Research Laboratory Materials Center of Excellence

Dynamic Behavior and Optimization of Advanced Armor Ceramics: January–December 2012 Annual Report

edited by RA Haber
Recipient Program Manager
Director, Center for Ceramic Research
Rutgers, The State University of New Jersey
607 Taylor Road, Piscataway, NJ 08854-8065

and

JW McCauley (Emeritus)
Cooperative Agreement Manager
US Army Research Laboratory
Weapons and Materials Research Directorate, ARL
Aberdeen Proving Ground, MD 21005-5066

under contract W911NF-06-2-0007

REPORT DOCUMENTATION PAGE	Form Approved OMB No. 0704-0188

1. REPORT DATE *(DD-MM-YYYY)*	2. REPORT TYPE	3. DATES COVERED (From - To)
March 2015	Final	1 January–31 December 2012

4. TITLE AND SUBTITLE
US Army Research Laboratory Materials Center of Excellence

Dynamic Behavior and Optimization of Advanced Armor Ceramics: January–December 2012 Annual Report

5a. CONTRACT NUMBER
W911NF-06-2-0007

5b. GRANT NUMBER

5c. PROGRAM ELEMENT NUMBER

6. EDITOR(S)
RA Haber and JW McCauley (Emeritus)

5d. PROJECT NUMBER
BH64

5e. TASK NUMBER

5f. WORK UNIT NUMBER

7. PERFORMING ORGANIZATION NAME(S) AND ADDRESS(ES)
Center for Ceramic Research
Rutgers, The State University of New Jersey
607 Taylor Road
Piscataway, NJ 08854-8065

US Army Research Laboratory
RDRL-WM
Aberdeen Proving Ground, MD
21005-5069

8. PERFORMING ORGANIZATION REPORT NUMBER
ARL-CR-0767

9. SPONSORING/MONITORING AGENCY NAME(S) AND ADDRESS(ES)
US Army Research Laboratory
ATTN: RDRL-WM
Aberdeen Proving Ground, MD 21005-5069

10. SPONSOR/MONITOR'S ACRONYM(S)
ARL

11. SPONSOR/MONITOR'S REPORT NUMBER(S)

12. DISTRIBUTION/AVAILABILITY STATEMENT
Approved for public release; distribution is unlimited.

13. SUPPLEMENTARY NOTES

14. ABSTRACT
This Materials Center of Excellence program has been conducted as a seamless, synergistic collaboration among the following institutions: Rutgers Malcolm G McLaren Center for Ceramic Research, Penn State Particulate Research Center, the Johns Hopkins Center for Advanced Metal and Ceramic Systems, and the US Army Research Laboratory's Weapons and Materials Research Directorate. The following tasks are reviewed: Nanostructured Armor Ceramics: Focus on Boron Carbide; The Role of Microstructure in the Impact Resistance for Silicon Carbide; Education and Outreach; Defining Microstructural Tolerance Limits of Defects for Silicon Carbide Armor Ceramics; and Nondestructive Ultrasound Characterization of High-Density, High-Hardness Ceramics.

15. SUBJECT TERMS
armor, boron carbide, silicon carbide, ceramics, MCOE

16. SECURITY CLASSIFICATION OF:			17. LIMITATION OF ABSTRACT	18. NUMBER OF PAGES	19a. NAME OF RESPONSIBLE PERSON
a. REPORT	b. ABSTRACT	c. THIS PAGE			James W McCauley
Unclassified	Unclassified	Unclassified	UU	130	19b. TELEPHONE NUMBER (*Include area code*) 410-306-0711

Standard Form 298 (Rev. 8/98)
Prescribed by ANSI Std Z39 18

Contents

List of Figures

List of Tables

INTENTIONALLY LEFT BLANK.

1. Introduction

This Materials Cooperative Research Program will be conducted as a seamless, synergistic collaboration among Rutgers University's Malcolm G. McLaren Center for Ceramic Research and the US Army Research Laboratory's (ARL's) Weapons and Materials Research Directorate. This will enable the program to utilize the capabilities of each organization to focus the program on substantial improvement and continuous improvement of the scientific and technical understanding of advanced armor ceramics, including the following.

1.1 Core Programs

- Task 1: Nanostructured Armor Ceramics
- Task 2: The Role of Microstructure in the Ballistic Performance for Silicon carbide (SiC)
- Task 3: Education and Outreach

1.2 Mod-Shared with the Ceramic, Composite and Optical Materials Center (CCOMC)

- Task 4: Defining Microstructural Tolerance Limits of Defects for SiC Armor
- Task 5: Nondestructive Ultrasound Characterization (NDC) of High-Density, High-Hardness Ceramics

2. Task 1: Nanostructured Armor Ceramics, Materials Center of Excellence (MCOE) Core Program

Core Faculty: R Haber, D Niesz

ARL Leaders: J McCauley, J LaSalvia, T Jessen, R Dowding

Research Faculty: W Rafaniello

Research Associate: S Miller

Graduate Student: F Toksoy

2.1 Long-Range Objectives

- Synthesize "clean" single-phase, submicron, equiaxed, stoichiometric boron carbide (B_4C) powder with a narrow size distribution.
- Develop superior dense bodies.
- Determine residual graphite effect on amorphization.
- Clarify the source of carbon (C) from strain.
- Provide a means of doping B_4C C-C-C chain with silicon (Si) or aluminum (Al) to alter amorphization and properties.
- Silicon carbide (SiC)-B_4C binary would provide a density benefit to SiC.
- Potential clarification of B_4C phase diagram.

2.2 Background

B_4C is one the hardest known materials and, as such, is particularly useful as an armor ceramic material. For this application, it is desirable to use highly pure, single-phase, equiaxed, monodispersed B_4C powders with an average grain size of less than 1 µm. Such powders, when subjected to densification through hot pressing or spark plasma sintering (SPS) should yield a higher quality ceramic part.

Most commercial B_4C powder is manufactured by carbothermically reducing boron oxide (B_2O_3) in an electric arc furnace in the presence of a C source. Most commercial methods use coal or petroleum coke as a C source, which leads to a final product containing the impurities found in the raw material. The use of an electric arc furnace results in very high localized heating and slow conductive heating of the remaining batch. The entire heating and cooling process takes place over a period of days. This results in nonuniform process conditions and

nonuniform chemical composition in the final product, i.e., unreacted raw materials and variations in final product stoiciometry may be realized. Further, the kinetics and thermodynamics of the slow heating process causes the B_2O_3 to pass through the liquid phase, resulting in a nucleation limited step and the formation of large grains.

Ultrafine B_4C powders have been synthesized by vapor phase reactions of B and C containing compounds using laser pyrolysis. These powders were shown to be equiaxed and have a narrow size distribution. They were fully densified into superior parts with a fine microstructure and hardness values higher than those reported for high quality B_4C powders produced by more traditional methods such as in an electric arc furnace. However, this method is not suited for high-quantity production and would not be cost effective.

Approximately 20 years ago, work done at Dow Chemical Company by William (Bill) Rafaniello and others demonstrated that the rapid heating of a highly reactive mixture containing B_2O_3 and a C source for a sufficient length of time resulted in the formation of a uniform submicron B_4C powder. For this work a specific furnace design was implemented that allowed for raw materials to be maintained at nonreactive temperatures until just prior to exposure to sufficiently high temperatures for a vapor phase reaction—similar to spray pyrolysis. This furnace was capable of producing quantities above laboratory scales. In addition to demonstrating the ability to make a monodisperse submicron powder, these powders were also shown to be of high purity and could be consolidated into a ceramic part with superior properties.

Since the rapid heating process avoids many of the negative attributes of traditional B_4C synthesis, such as the presence of unreacted C and variations in B_2O_3 stoichiometry, it is believed that a furnace of this type can be used to investigate of the impact of C on the amorphization of B_4C in high strain-rate applications, provide a means of doping the B_4C structure with appropriate elements, leading to potential property improvements, and potentially lead to a SiC-B_4C binary system. Additionally, the ability to produce a superior B_4C part with a pure, monodispersed, submicron powder can be reconfirmed.

2.3 Current Status of the Rapid Carbothermic Reduction Furnace

The work on this project began in May 2010. Several meetings were held with Bill Rafaniello to discuss the important aspects of the furnace. The most important aspect discussed was the ability of the furnace to keep the precursor temperature below 450 °C prior to entering the furnace hot zone, where the temperature will be

maintained at 1,700 °C or higher. From these discussions, the general furnace design shown in Fig. 2.1 was developed. An existing 3.5- × 6-inch (hot zone size) graphite furnace (Thermal Technologies) was completely rebuilt, and the hot zone size was expanded to 4.5 × 6 inches to accommodate the graphite components, which are necessary to maintain the appropriate temperature and manage movement of reaction gases out of the furnace. The previously mentioned graphite components were designed by the Rutgers team and machined by Weaver Industries. All assembly of the furnace body and internal components have been completed and tested.

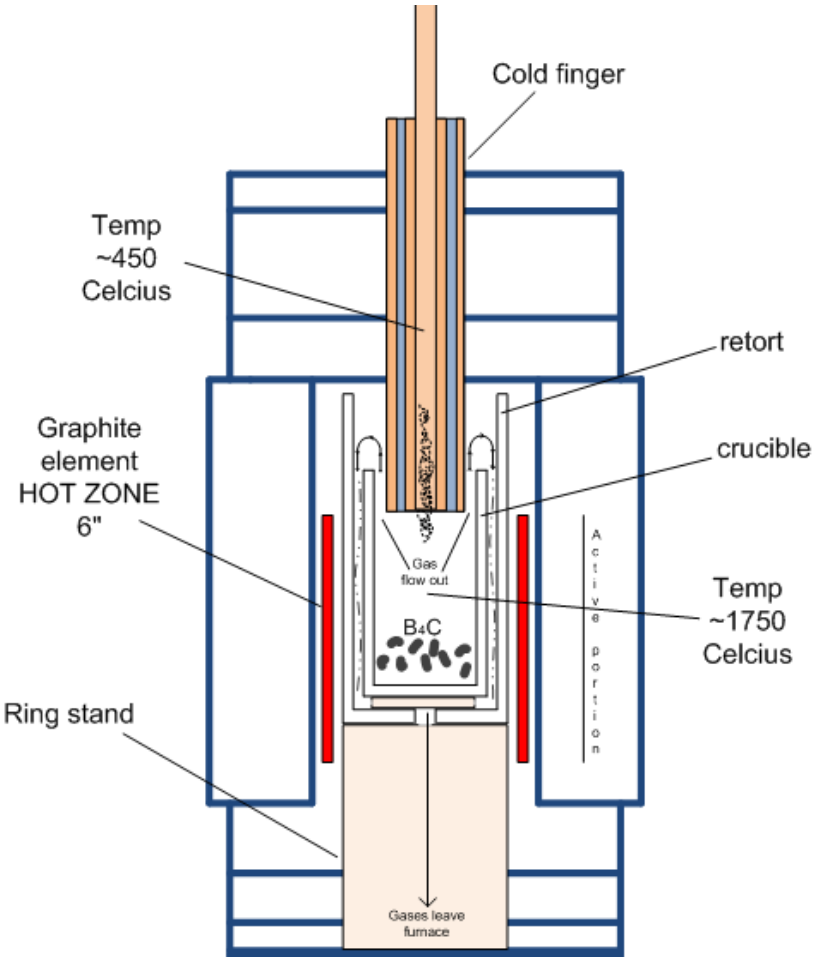

Fig. 2.1 Rapid carbothermic reduction furnace design

To maintain the precursor temperature below 450 °C before entering the furnace hot zone, a cold finger design was used. This is a jacketed copper tube through which chilled water is pumped. Copper was being used because of its high thermal conductivity. To minimize the number of solder joints, it was being constructed of

3 interlocking components bored from solid copper. The final design of the copper cold finger is shown in Fig. 2.2. It was built by the Rutgers Physics Department machine shop and has been helium leak tested and installed in the furnace.

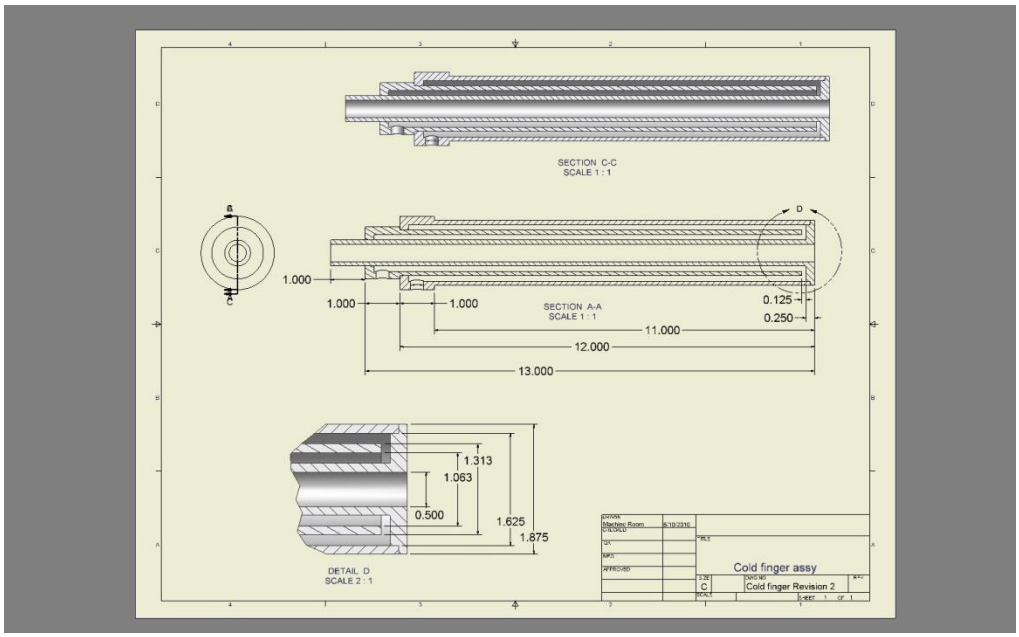

Fig. 2.2 Copper cold finger design

Control of the system was accomplished by installing the furnace body and copper cold finger on an existing Astro Refractory (tungsten) Furnace System. This included changing the power supply to match the new graphite element, upgrading the power monitoring system to include data logging features, new temperature controller, and alterations to the gas supply and vacuum systems. The feeding of precursor materials is accomplished through 1 of 2 methods: 1) a drop system for rapid experimentation where a fixed amount is loaded into a hopper and released through a ball valve and 2) a screw feed system for generating larger samples based on the results from the drop system. The screw feed system was designed and constructed using Swagelok and other off-the-shelf components. Figure 2.3 shows the completed furnace with the copper cold finger and screw feed installed. A series of inline flow-through thermocouples and process/temperature meters to monitor water temperature in and out of the cold finger have been installed. Flow switches have been integrated into an interlock system for protection of the furnace in the event of water flow interruption. The furnace and screw feed system have been tested and is operational.

Fig. 2.3 Rapid carbothermic reduction furnace with copper cold finger and screw feed

2.4 B_2O_3 Precursor Preparation

The chemical reaction equation for the B_2O_3 by carbothermic reduction is

$$2\ B_2O_3(l,g) + 7C\ (s) \rightarrow B_4C(s) + 6CO(g). \quad (1)$$

From this equation it is clear that preparing an intimate mixture of B_2O_3 and C is a necessary and important part of the rapid carbothermic reduction process. Figure 2.4 shows a basic flowchart of the B_4C precursor preparation process.

[redacted]

Fig. 2.4 Basic B_4C precursor preparation method

Simply, boric acid is dissolved in warm water and mixed with a C-water slurry and thoroughly stirred. The mixture is dried of unbound water and pulverized. The mixture is then calcined at a temperature sufficient to dehydrate the boric acid, converting it to B_2O_3, and liquify the B_2O_3 ($T_m \approx 450$ °C). After cooling, the precursor material is milled to the desired particle size.

There are several aspects to this process that can affect the efficacy of the precursor material. The choice of the C source is particularly important. Various C blacks and toner inks are a source of very pure, high-surface-area, and highly reactive C. However, these C sources can be difficult to make into stable slurries, as the C tends to flocculate. So far, we have produced precursors using lampblack (lower surface area) and Vulcan XC-72 (higher surface area), a commercially produced C source (Cabot, Inc.). The aid of a dispersant such as Triton X-100 was necessary to produce a slurry using the Vulcan product. In both cases, constant mixing during the drying process is necessary to prevent separation of the C and B_2O_3 as the water is removed. The use of each of these in the production of B_4C was successful, but no conclusion as to the benefit of each has been drawn.

The use of corn starch as an organic C source is also being investigated. Cornstarch is easily dispersed in water, and during the calcining process may form B complexes that help maintain the intimate mixture necessary for an effective precursor. Initial results with cornstarch have been promising.

The thermodynamics of the carbothermic reduction process favor a reaction above 1,542 °C, where it becomes exothermic. However, the sublimation temperature of B_2O_3 is approximately 1,500 °C. Therefore, even when this reaction occurs rapidly, maintaining a completely stoichiometric reaction is difficult. Since unreacted C is difficult to remove from B_4C and excess B_2O_3 is easily removed to through mild acid washing, completely reacting all the C is necessary. This can be achieved by preparing precursor materials with an amount of B_2O_3 in excess of which is necessary for a stoichiometric reaction. We have prepared precursors with excess B_2O_3 in the amounts of 20%, 30%, and 50% in excess of stoichiometry. Initial results suggest 30% excess B_2O_3 may be sufficient to completely react with all the C while easily removing any excess B_2O_3.

2.5 Production of B_4C in the Rapid Carbothermic Reduction Furnace

Using the rapid carbothermic reduction furnace described, B_4C production experiments may be carried out in the following 3 ways:

- A static (batch) process where the precursor is placed in a graphite crucible inside the hot zone of the furnace. It is then heated at a predetermined rate to the reaction temperature, held at that temperature, and allowed to cool.
- A drop test where a small amount of precursor is allowed to drop through the copper cold finger into a crucible in the hot zone of the furnace already at the reaction temperature. The drop test serves 2 functions: It simulates what might be dropped during a single pulse of a screw feed and it allows for rapid experimentation where many parameters may be subject to variation (temperature, cold finger position, etc.).
- A screw feed process where large amounts of precursor (currently up to ~200 g) are placed in a hopper and a screw feed mechanism allows the precursor to fall through the cold finger at a fixed rate into the preheated crucible in the hot zone of the furnace. In its current configuration the screw feed allows for feed rates of 0.75–2.50 g/min.

As of the writing of this report, 25 B_4C synthesis runs have been made. Table 2.1 provides a summary of those runs.

Table 2.1 Summary of Rutgers carbide±C produced by rapid carbothermic reduction

Powder	Precursor	Type/ Temp (°C)	Product /Charge	Analysis ID	X-Ray Diffraction (XRD)
S1P1ST25	P1 20% excess lampblack	Static 1,750	7.41g/25 g	BC-ST1	20% C per lattice and 40% free C
S2P1DR2	P1 20% excess lampblack	Drop 1,750	0.44 g/2 g	BC-DR1	20.2% C per lattice 31% free C
S3P1DR05	P1 20% excess lampblack	Drop 1,750	0.11 g/0.5 g	ND	ND
S4P2DR2	P2 50% excess lampblack	Drop 1,750	0.468 g/2 g 0.35 g after wash	BC-DR2	19.6% C per lattice 13.9% free C
S5P2DR05	P2 50% excess lampblack	Drop 1,750	0.154 g/0.5 g	ND	ND
S6P3DR2	P3 30% excess lampblack	Drop 1,750	0.4116 g/2 g	BC-DR3	19.8% C per lattice 4.4% free C
S7P3DR05	P3 30% excess lampblack	Drop 1,750	0.1 g/0.5 g	ND	ND

Table 2.2 Summary of Rutgers B_4C produced by rapid carbothermic reduction (continued)

Powder	Precursor	Type/ Temp/ (°C)	Product /Charge	Analysis ID	XRD
S8P3DR2	P3 30% excess lampblack	Drop 1,800	0.36 g/2 g	BC-DR4	19.6% C per lattice 9.4% free C
S9P3DR2	P3 30% excess lampblack	Drop 1,850	0.4 g/2 g	BC-DR5	19.8% C per lattice 3.4% free C
S10P3DR05	P3 30% excess lampblack	Drop 1,800	0.098 g/0.5 g 0.082 after wash	ND	ND
S11P3DR05	P3 30% excess lampblack	Drop 1,850	0.045 Center 0.04 Edge 0.5 g	ND	ND
S12P5DR2	P5 30% excess Vulcan	Drop 1,850	0.42 g/2 g	BC-DR6	19.9% C per lattice 1.3% free C
S13P7SF	P7 30% excess lampblack	Screwfeed 1,800 ~1 gr/cm3	9.2 g/56.1 g 8.6 g after wash	BC-SF1	19.9% C per lattice 7.7 % free C
S14P6DR2	P6 30% excess corn starch	Drop 1,850	0.37 g/2 g	BC-DR7	20.2% C per lattice no free C
S15P8DR1	P8 30% excess corn starch	Drop 1,750	0.16 g/1.1 g	ND	ND
S16P8SF	P8 30% excess corn starch	Screwfeed 1,800	47 g; 8 psi. Shut down at 40 min 4.4 g < –150 mainly B_4C 1.2 mixed mainly precursor	BC-SF2	20.9% C per lattice 8.5% free C
S17P9DR2	P9 10% excess corn starch	Drop 1,800	0.24 g/2 gr	ND	ND
S18P9SF	P9 10% excess corn starch	Screwfeed 1,800	9/13: 2.2 g/20 g clogged at 16 min 9/14: 1.8 g/15 min clogged at 14 min	BC-SF2	20.9% C per lattice 8.5% free C
S19P10SF	P10 0% patent corn starch	Screwfeed 1,800	9/20: 2.98 g/20 g clogged at 21 min 9/21: 2.3 g/15 g clogged at 14 min	BC-SF3	20% C per lattice 4% free C
S20P11SF	P11 0% patent corn starch	Screwfeed 1,800	1.5 g/10 g clogged at 10 min	ND	ND
S21P11SF	P11 0% patent corn starch	Screwfeed 1,800	2.4 g/25 g power off for 3 min and dropped to 1,690s °C	ND	ND
S22P12SF	P12 0% patent corn starch	Screwfeed 1,850 ~1.5 g/cm3	34 g clogged at 20 min, 8.4 g in the hopper, 2.5 g powder	ND	ND

ND = not determined

Table 2.1 Summary of Rutgers B_4C produced by rapid carbothermic reduction (continued)

Powder	Precursor	Type/ Temp/ (°C)	Product /Charge	Analysis ID	XRD
S23P13SF	P13 0% patent corn starch	Screwfeed 1,850 ~1.5g/cm^3	5.6 gr of 44 gr of precursor; little bit of powder around the chamber and in the exhaust	BC-SF4 Sent for XRD&C in 11/9	
S24P14SF	P14 50% lampblack	Screwfeed 1,850 ~1.3g/cm^3	7 gr of 50 gr of precursor; little bit of powder around the chamber and in the exhaust	BC-SF5 Sent for XRD&C in 11/9	
S25P15SF	P15 50% Vulcan	Screwfeed 1,850 ~1.2g/cm^3			

Whenever possible, samples are subject to the following characterization techniques: scanning electron microscopy (SEM), XRD, particle size analysis, and C and B determination (through chemical analysis). Small initial sample sizes preclude all of the analysis for many of the initial runs. What follows are results for 6 relevant samples: BC-ST1, BC-DR1, BC-DR7, BC-SF1, BC-SF4, and BC-SF5.

2.5.1 BC-ST1

This was a static run where 25 g of precursor was reacted at 1,750 °C for 30 min. The precursor used lampblack as a C source and had 20% excess B_2O_3. The average particle size, as determined using SEM micrographs similar to that in Fig. 2.5 was 6.7 µm. Using XRD, lattice C was determined to be 20.0% or $B_{4.00}C$, and free C was determined to be 40%. The SEM images show narrowly distributed, equiaxed crystallites with areas of nanosized free C distributed among the crystallites.

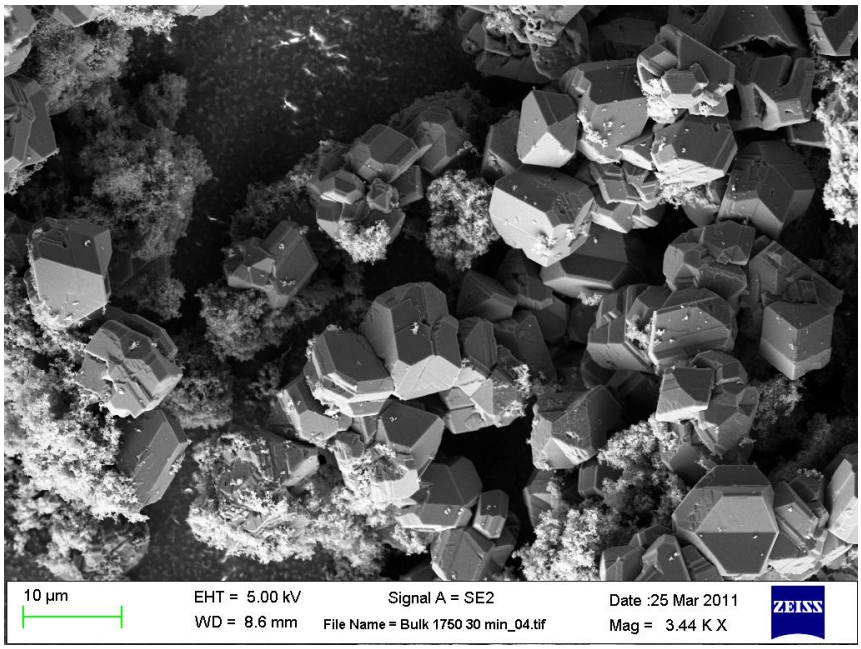

Fig. 2.5 SEM micrograph of static (batch) processed B_4C; average particle size = 6.7 µm

2.5.2 BC-DR1

This was a drop test where 2 gr of precursor material was dropped into the preheated furnace at 1,750 °C and allowed to dwell for 2 min. The precursor used lampblack as a C source and had 20% excess B_2O_3. The average particle size, as determined using SEM micrographs similar to that in Fig. 2.6 was 1.2 µm. Using XRD, lattice C was determined to be 20.2% or $B_{3.95}C$, and no free C was detected. The SEM images show narrowly distributed, equiaxed crystallites with areas of nanosized free C distributed among the crystallites.

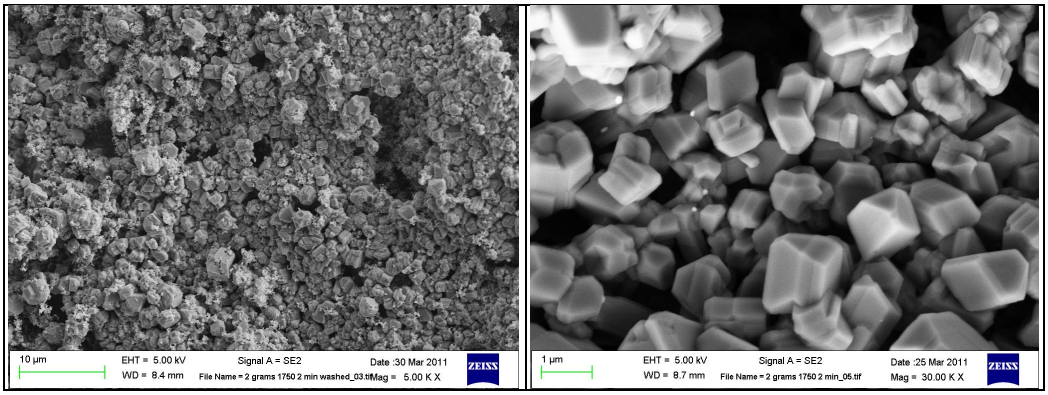

Fig. 2.6 SEM micrographs of B_4C from a 2-gr drop test using lampblack as a C source; average particle size = 1.2 µm

2.5.3 BC-DR7

This was a drop test where 2 gr of precursor material was dropped into the preheated furnace at 1,850 °C and allowed to dwell for 2 min. The precursor used corn starch as a C source and had 30% excess B_2O_3. The d(0.9) using light scattering was 1.27 µm. Using XRD, lattice C was determined to be 20.1% or $B_{3.98}C$, and free C was determined to be 31%. The SEM images, shown in Fig. 2.7, show a more widely distributed, equiaxed crystallites with no free C. Nanometer-sized crystallites can be seen with necking between them.

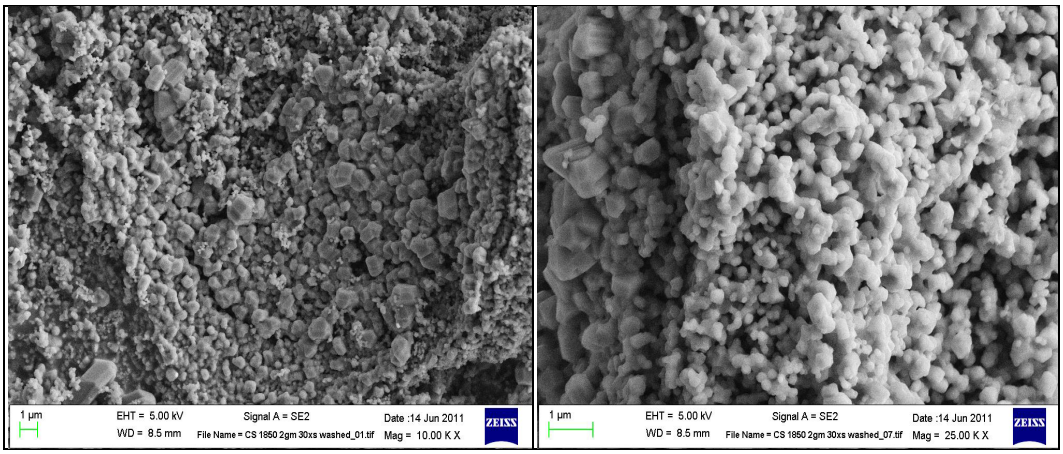

Fig. 2.7 SEM micrographs of B_4C from a 2-gr drop test using corn starch as a C source; D(0.9) = 1.27 µm

2.5.4 BC-SF1

This was a screw feed run where approximately 46 gr of precursor material was fed into the preheated furnace at 1,800 °C at a rate of 1 gr/min. The precursor used lampblack as a C source and had 30% excess B_2O_3. The d(0.9) using light scattering was 1.15 µm. Using XRD, lattice C was determined to be 19.9% or $B_{4.10}C$ and free C was determined to be 7.7%. The SEM images, shown in Fig. 2.8, show narrowly distributed, equiaxed crystallites with some free C.

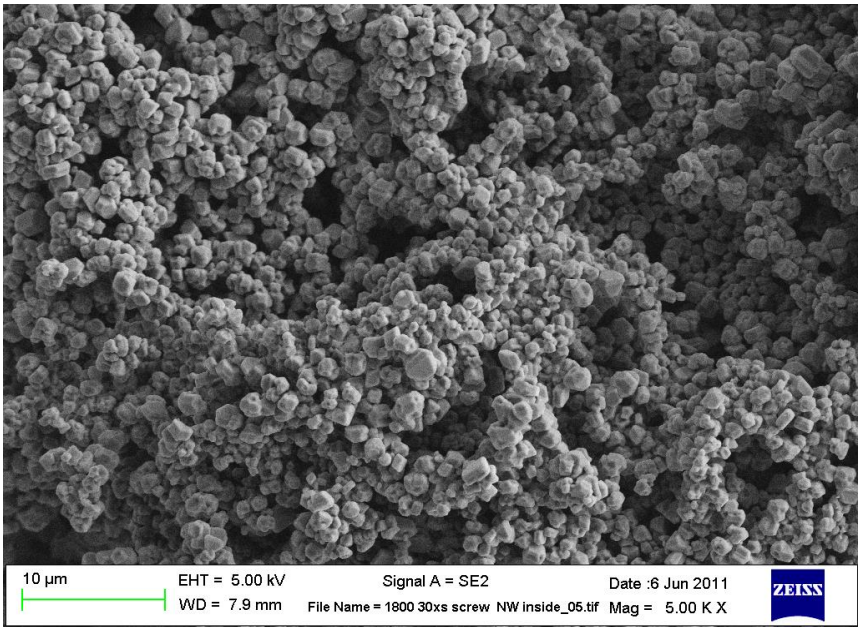

Fig. 2.8 SEM micrograph of B_4C from a screw feed sample using lampblack as a C source; average particle size = 1.15 µm

2.5.5 BC-SF4

This was a screw feed run where approximately 44 gr of precursor material was fed into the preheated furnace at 1,850 °C at a rate of approximately 1 gr/min. The precursor used cornstarch as a C source and should have 30% excess B_2O_3 based on previously performed experiments at Dow Chemical. The d(0.9) using light scattering was 0.91 µm, which is likely overstated because of equipment limitations and the high degree of necking between particles making separation difficult. Using XRD, lattice C was determined to be 19.7% or $B_{4.07}C$, and no graphitic C peak was noted. Also, XRD identified the presence of a second B-C phase with a composition of roughly $B_{25}C$ to $B_{50}C$. Based on chemical analysis, excess C in the range of 5%–6% was noted. The SEM images, shown in Fig. 2.9, show submicron, narrowly distributed, equaled crystallites with no apparent free C. As previously mentioned, a high degree of necking can be seen.

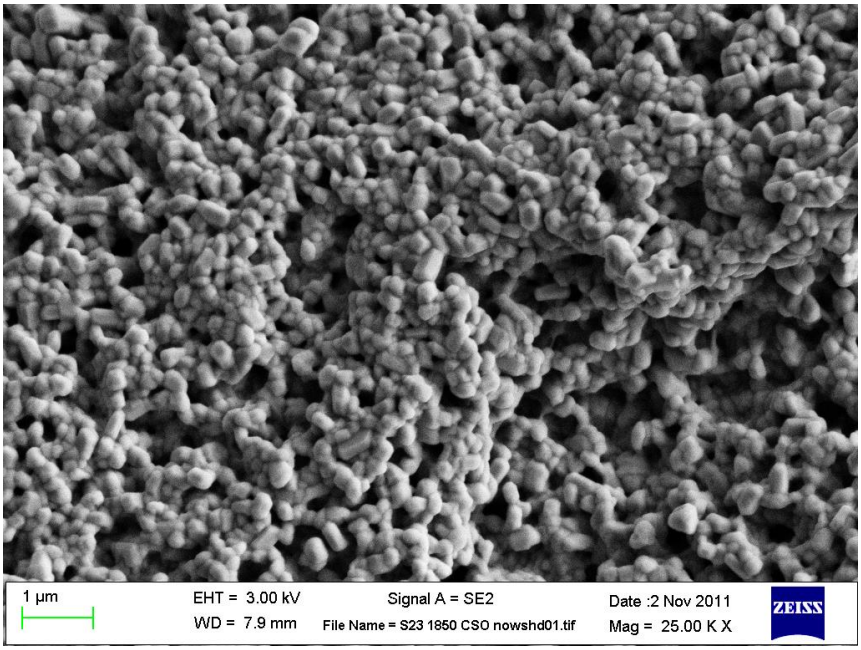

Fig. 2.9 SEM micrograph of B_4C from a screw feed sample using cornstarch as a C source; average particle size = <0.91 µm

2.5.6 BC-SF5

This was a screw feed run where approximately 50 gr of precursor material was fed into the preheated furnace at 1,850 °C at a rate of 1 gr/min. The precursor used lampblack as a C source and had 50% excess B2O3. The d(0.9) using light scattering was 1.18 µm. Using XRD, lattice C was determined to be 18.9% or $B_{4.29}C$, and no graphitic C peak was noted. As with sample BC-SF4, XRD identified the presence of a second B-C phase with a composition of roughly $B_{25}C$ to $B_{50}C$. Using chemical analysis, free C was found to be 2%–3%. The SEM images shown in Fig. 2.10 show narrowly distributed, equiaxed crystallites with some free C.

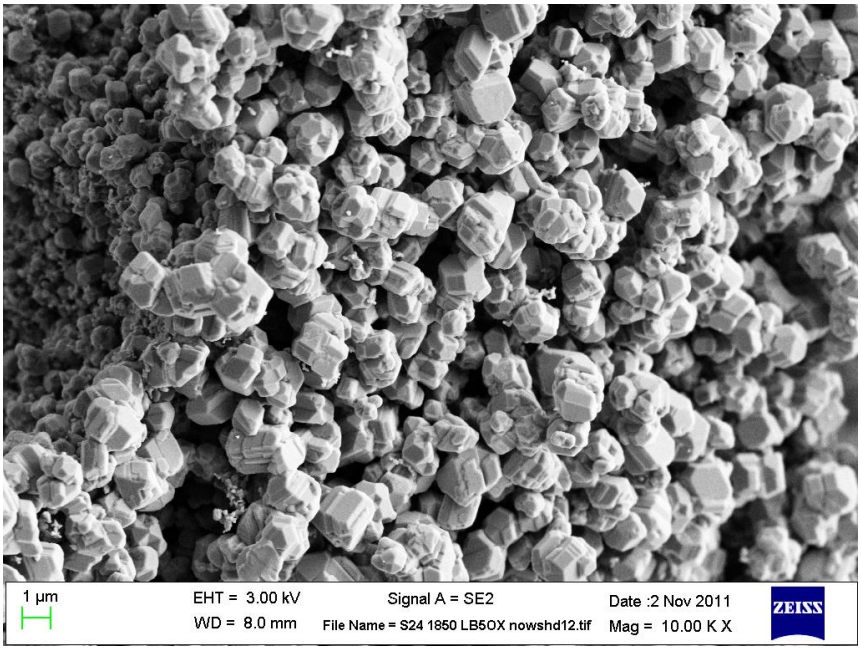

Fig. 2.10 SEM micrograph of B_4C from a screw feed sample using lampblack as a C source; average particle size = 1.18 µm

2.5.7 X-ray Diffraction

XRD analysis is used to verify the B_4C structure, estimate free C, and estimate stoichiometry. Fig. 2.11 shows the XRD spectra for samples BC-ST1, BC-DR1, and a commercial B_4C. The peak positions confirm the icosahedra-based rhombohedral lattice structure of B_4C. The C peak confirms that free C is present. However, the lower relative peak intensity and broader lines suggest less free C than the commercial B_4C and that the C is smaller—consistent with that seen in the SEM images. Additionally, the broader B_4C peaks suggest finer crystallite size than the commercial product.

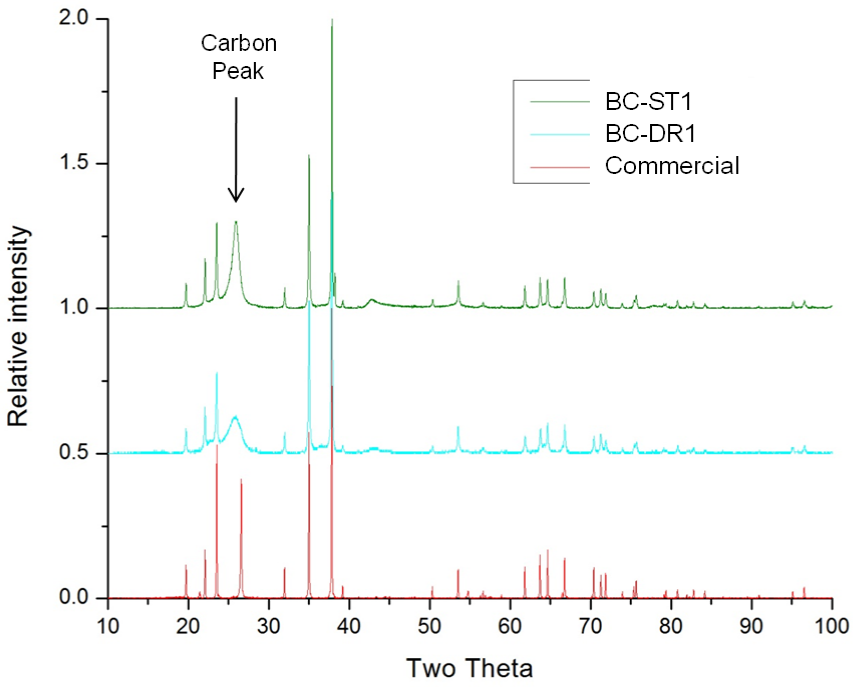

Fig. 2.11 XRD spectra for a static run (BC-ST1), a drop test run (BC-DR1), and a commercial powder

XRD may also be used to determine the stoichiometry of B_4C. Based on the work by Aselage and Tissor (1992), there appears to be a linear relationship between the lattice parameters of B_4C and the C concentration in atomic percent. Using this information and data provided by Rutgers' Dr William Mayo (personal communication, 2012, unreferenced), the lattice parameters and calculated C content for samples BC-ST1, BC-ST1, and BC-SF1 are presented in Table 2.2. Also included are the lattice parameters and calculated C content for several commercial B_4C. This table clearly demonstrates that the Rutgers B_4C produced by rapid carbothermic reduction is closer to stoichiometric B_4C.

Table 2.2 Lattice parameters and calculated C content from various commercial B_4C powders and 3 initial Rutgers B_4C powders produced by rapid carbothermic reduction

	Lattice Parameters (Å)		Calculated Carbon Content (at %)		
Sample ID	**a**	**c**	**Based on a**	**Based on c**	**Average**
Starck Grade MS	5.6096	12.097	17.0	18.1	17.5
ESK Tetrabor 3000F	5.6259	12.124	12.7	16.2	14.5
UK Abrasive 0.5µm	5.6174	12.111	15.0	17.1	16.0
UK Abrasive 1.3 µm	5.6141	12.103	15.8	17.6	16.7
Electro Abrasives 2.5 µm	5.6071	12.089	17.7	18.6	18.2
Electro Abrasives 1200	5.6029	12.079	18.8	19.3	19.1
SSI Grade B	5.6114	12.100	16.6	17.9	17.2
Superior Graphite Grade M	5.6154	12.107	15.5	17.4	16.4
Rutgers BC-DR1	5.5975	12.0687	20.2	20.0	20.1
Rutgers BC-ST1	5.5983	12.0694	20.0	20.0	20.0
Rutgers BC-SF1	5.5987	12.0785	19.9	19.3	19.6

To more clearly show how the Rutgers B_4C compares with the commercial powders, the B-to-C ratio was calculated and stack ranked against the commercial powders, as shown in Table 2.3, and their relative positions within the B_4C phase field, as shown in Fig. 2.12. While the Rutgers powders appear to be either stoichiometric B_4C or slightly B-rich as a result of increased temperature and B content in the precursor, all of the commercial powders appear to be substantially in the B-rich region of the B_4C phase field.

Table 2.3 B-to-C ratios of Rutgers and various commercial B_4C powders

Sample ID	Approximate Composition
ESK Tetrabor 3000F	$B_{5.90}C$
UK Abrasives 1.3µm, 0.5µm	$B_{4.99\text{-}5.25}C$
Superior Graphite Grade M	$B_{5.10}C$
SSI Grade B	$B_{4.81}C$
Starck Grade MS	$B_{4.71}C$
Electro Abrasives 1200, 2.5 µm	$B_{4.24\text{-}4.49}C$
Rutgers BC-SF7	$B_{4.21}C$
Rutgers BC-ST1	$B_{4.00}C$
Rutgers BC-DR1	$B_{3.98}C$

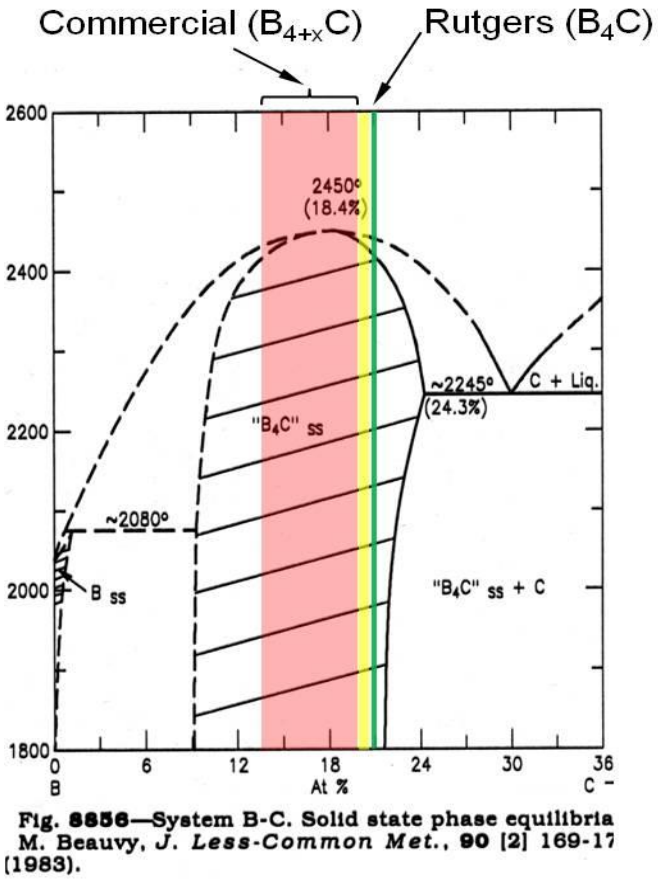

Fig. 8856—System B-C. Solid state phase equilibria
M. Beauvy, *J. Less-Common Met.*, **90** [2] 169-17
(1983).

Fig. 2.12 B-to-C ratios of Rutgers and commercial B_4C powders shown in B_4C phase field

2.6 Spark Plasma Sintered B_4C

To demonstrate the ability to densify the B_4C produced from rapid carbothermic reduction, 4 g of unrefined B_4C material from BC-SF1 (screw feed sample) was spark plasma sintered at 1,850 °C for 20 min at a pressure of 50 MPa. The density of the material was determined using the Archimedes method to be 2.485 g/cm^3. Since the unrefined B_4C powder had 7.7% free C, hardness measurements were only considered from indents where no C inclusions were present. Based on these, average Knoop hardness was determined to be 2,237. A SEM micrograph of the polished sample and a Knoop indent are shown in Fig. 2.13.

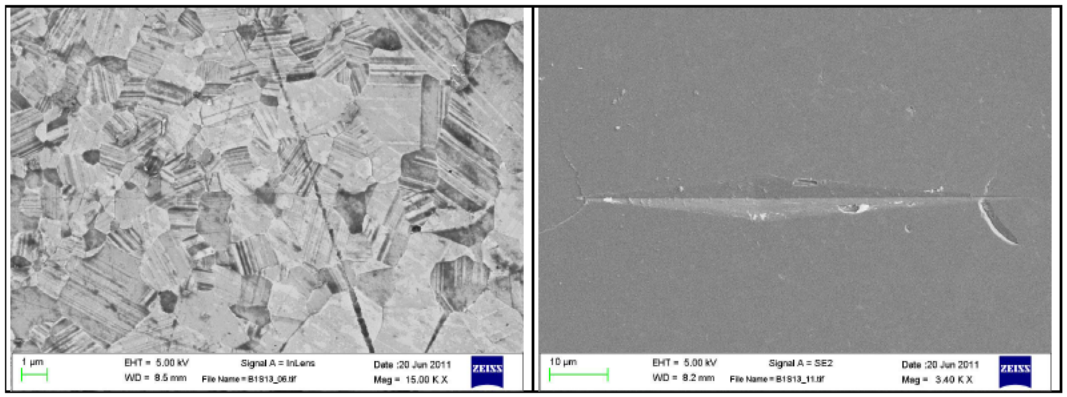

Fig. 2.13 SEM micrographs of (left) spark plasma sintered B_4C from a screw feed sample BC-SF1 using lampblack as a C source and (right) Knoop hardness indent at 1 kg

As of the writing of this report, powders from 7 screw feed runs have been densified. Density and Knoop hardness (HK) results are summarized in Table 2.4.

Table 2.4 SPS B_4C samples with density and hardness values

Sample	Conditions	C % (powder)	Density (g/cm^3)	HK Low	HK Average	HK High
Rutgers SF1	1,850 °C, 50 MPa	Lampblack 6%–8%	2.49	2,179	2,237	2,321
Rutgers SF2	1,850 °C, 50 MPa	Corn starch 7%–8%	2.40	2,163	2,216	2,268
Rutgers SF3	1,900 °C, 50 MPa	Corn starch 3%–4%	2.49	2,026	2,263	2,400
Rutgers SF4	1,850 °C, 50 MPa	Corn starch 5%–6%	2.51	2,132	2,319	2,387
Rutgers SF5	1,850 °C 50 MPa	Lampblack 2%–3%	2.49	2,333	2,373	2,412
Rutgers SF6	1,850 °C, 50 MPa	Vulcan	2.51	. . .	2,295	. . .
Rutgers SF7	1,850 °C, 50 MPa	Vulcan	2.51	. . .	2,359	. . .
Commercial 5	1,850 °C, 50 MPa	3%–4%	2.49	2,100	2,148	2,212
Commercial 1	1,900 °C, 50 MPa	3%–4%	2.492	2,223	2,350	2,392

Additional SEM micrographs of densified samples, SF5 and SF7, are shown in Fig. 2.14. It can be seen that the microstructure is consistent across samples.

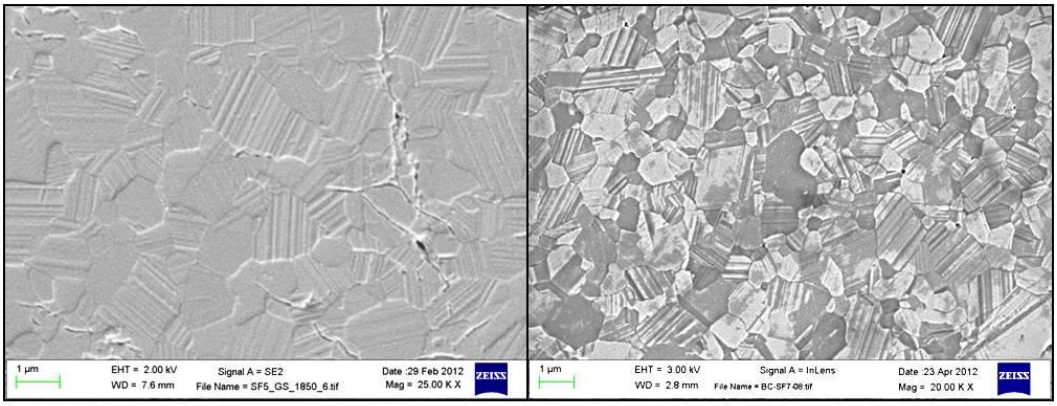

Fig. 2.14 SEM micrographs of (left) spark plasma sintered B_4C from a screw feed sample BC-SF1 using lampblack as a C source and (right) Knoop hardness indent at 1 kg

2.7 Conclusion and Future Work

The results described represent the initial attempts in synthesizing B_4C using rapid carbothermic reduction. The ability to produce submicron equiaxed B_4C has been demonstrated. Additionally, every sample has resulted in stoichiometric or very near stoichiometric (B_4C, a 4:1 B-to-C ratio) B_4C based on XRD analysis. However, further refinement of the processing parameters (precursor component ratio, temperature, feed rate, etc.) must be completed so that grain size and stoichiometry may be controlled while resulting in no free C. These efforts are ongoing. Figure 2.15 shows a multidimensional matrix that continues to be used to determine the optimal processing conditions.

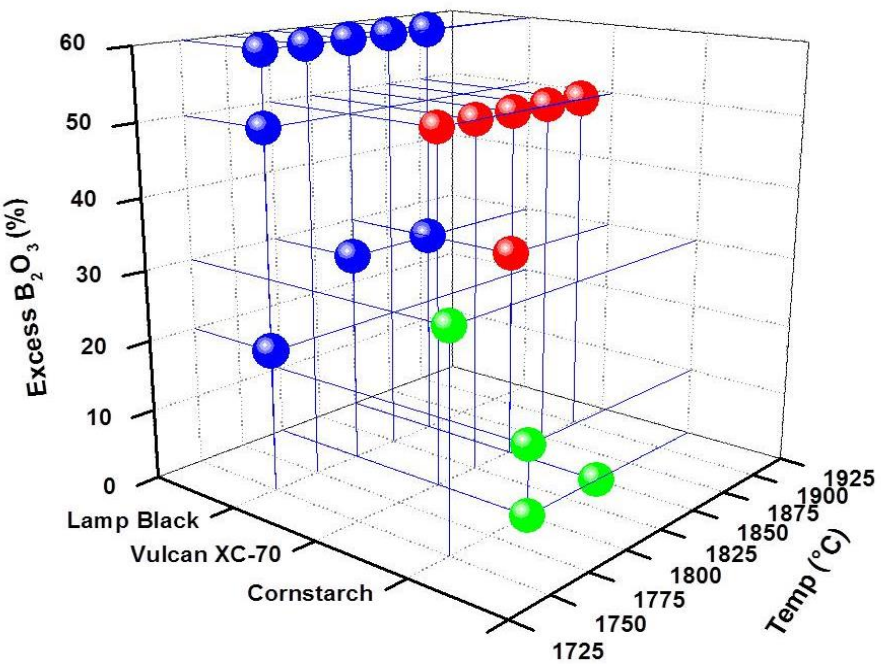

Fig. 2.15 Experiment matrix showing processing parameters

Methods for adequate B and C determination to corroborate XRD analysis are currently being established and tested.

As the processing conditions are optimized, increasing work on densification will be undertaken. Additionally, we will investigate the use of thickeners for improved mixedness in precursors using C black materials and investigate compounds to be used for Al and Si doping.

2.8 References

Weimer A, Moore W, Roach R, Hitt J, Dixit R, Pratsinis S. Kinetics of carbothermal reduction synthesis of boron carbide. J Am Ceram Soc. 1992;75(9):2509.

Knudsen A. Laser-driven synthesis and densification of ultrafine boron carbide powders. Advances in Ceramics: Ceramic Powder Science. 1987;21:237.

Rafaniello W, Moore W, inventors; The Dow Chemical Company, assignee. Heating reactive mixture of boroic oxide and carbon yields submicron size particles. United States patent US 4,804,525. 1989 Feb 14.

Aselage and Tissor. Lattice constants of boron carbide. J Am Ceram Soc. 1992;75(8):2207.

3. Task 2: The Role of Microstructure in the Impact Resistance for Silicon Carbide (SiC), Core Program

Core Faculty: RA Haber

ARL Collaborator: T Jessen

Graduate Student: S Bagienski

Undergraduate Student: M Sperling

3.1 Long-Range Goals

- To study the effect of sintering time on proprecipitated silicon carbide's (SiC's) core-rim microstructure, hardness, and material properties.
- To study the effect of varying amounts of SiC polytypes/stacking faults on the core-rim microstructure, hardness, and material properties.
- To use results of sintering time and polytype composition studies to engineer materials with optimal properties.

3.2 Background

SiC has been an industrially relevant ceramic for a wide range of applications such as an abrasive, a refractory, wear-resistant bearings, semiconductors, electronic devices, and as an armor ceramic. The strong covalent bonding in SiC between lightweight atoms makes it a suitable ceramic for armor application.[1,2]

The crystal structure of SiC can vary throughout the material but typically is hexagonal. It can be visualized more easily as an array of tetrahedral molecules with Si at the center and carbon (C) at the edges (or vice versa). The tetrahedral are joined at the corners in one plane, in this example by the C atoms. The next plane of atoms can then be arranged in either a parallel fashion where the Si atoms lies directly above the gaps between C atoms in the first plane or an antiparallel fashion where the Si atoms directly above the C atoms in the first plane (see Fig. 3.1).[3]

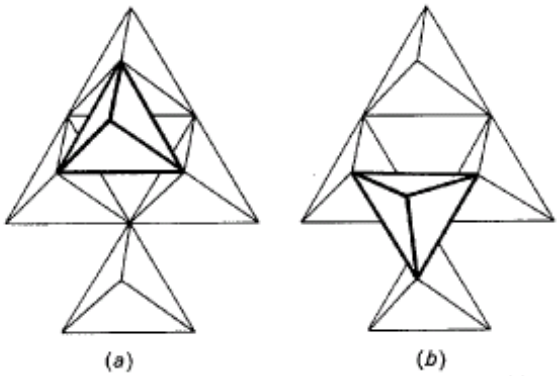

Fig. 3.1 Parallel (a) and antiparallel (b) stacking arrangement of SiC. The centers of the tetrahedra contain Si atoms, and the corners would contain C atoms (or vice versa).

This structure can result in an infinite number of combinations of different stacking layers, and to distinguish the layers, Ramsdell notation is used. Ramsdell notation designates the crystal structure as *nL* where *n* is the number of layers before the pattern repeats itself and *L* is the crystal symmetry with L = H for hexagonal, L = R for rhombohedral, and L = C for cubic symmetry. The most common of these polytypes is 4H, 6H, 15R, and cubic SiC.

Because of the nature of SiC's crystal structure, it is very likely that stacking faults exist. Stacking faults exist as a disruption in the stacking sequence of the repeating planes of atoms. There is an energy associated with creating these stacking faults that depends on the polytype of SiC. It is likely that this energy could be used as an intragranular energy abortion mechanism resulting in improved material properties.

H. Gu et al. have shown that in an aluminum nitride (AlN)-SiC system one can create a "core-rim" grain structure.[4] This core-rim structure shows a different composition within a single grain, creating an outer rim surrounding an inner core. The structure likely arises from AlN diffusing into SiC. They found that it is possible to shift 6H-SiC into 2H-SiC by adjusting the amount of AlN in their samples. If there are ways to manipulate these polytypes, and therefore their stacking fault energies, it may be possible to engineer superior ceramics for armor applications.

A method shown to improve mixedness of sintering aids and develop fine grained SiC is coprecipitation,[2] which involves precipitating the sintering aids along with a secondary phase to create a uniformly distributed composition of sintering aids (see Fig. 3.2). This results in fewer conglomerations of sintering aids and in reinforcing the grain boundary strength.

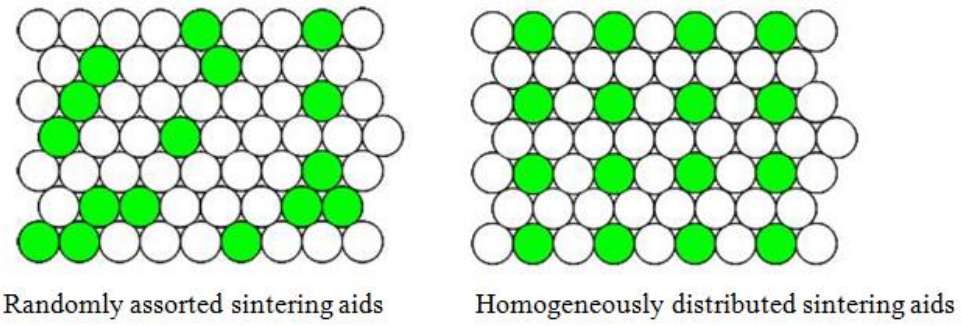

Fig. 3.2 The advantage of coprecipitation: Coprecipitated powder (right) would have more homogeneously distributed sintering aids.

The present study uses coprecipitation of AlN on to SiC particles by using yttria (Y_2O_3) as the secondary phase. Spark plasma sintering (SPS) was performed on the coprecipitated powder to densify the powder into a dense ceramic. To examine the diffusion behavior, powders were sintered at various dwell times and samples were made with varying amounts of sintering aids. The resulting samples were examined via density, hardness, and field emission scanning electron microscopy (FESEM).

3.3 Experimental Approach

The starting powder used in this study was H.C. Starck UF-25 (H.C. Starck GmbH, Goslar, Germany). This powder is a fine-grained powder produced by the Acheson process. Starck reported that it consists primarily of the 6H polytype and has an average grain size of 0.45 µm and a Brunauer-Emmett-Teller (BET) surface area of 23–26 m^2/g.

This powder was processed using a coprecipitation procedure that has been proven to facilitate SiC densification during sintering.[2] For this purpose, AlN and yttrium nitrate hexahydrate [$Y(NO_3)_3$ $6H_2O$] were used as coprecipitation agents. The amount of SiC, AlN, and $Y(NO_3)_3$ $6H_2O$ was calculated to get a resulting composition of 5-wt% AlN and Y_2O_3 additive, with a molar ratio of AlN:Y_2O_3 of 3:2. The calculated amount of SiC and AlN was measured out and placed into a 250-mL Nalgene bottle with enough isopropanol to get a paint-like viscosity. This slurry was ball-milled for 2 h with 3/16-inch SiC milling media. After milling, the slurry was sieved, pan-dried, and powder was put in a 100 °C oven overnight.

To start the coprecipitation, powder was loaded into a beaker with isopropanol and mixed by propeller for 1 h before starting the coprecipitation. The $Y(NO_3)_3$ $6H_2O$ was dissolved in isopranol and added to one buret while another buret was filled with ammonia hydroxide. A pH meter was submerged in the stirring solution to ensure that the pH remained around 9.5 throughout the coprecipitation. This is the

optimal pH required for coprecipitation to occur. Ammonia hydroxide was initially added to the AlN and SiC slurry to bring the pH to 9.5. The pH of the solution was adjusted with ammonia hydroxide as needed as the yttrium solution was added. After all of the yttrium solution was added, it continued to mix for 2 h while maintaining a pH of around 9.5.

Following this titration, the solution was allowed to settle and the organic layer was sucked off to remove most of the nitrates and organics. The slurry was washed with isopropanol, allowed to settle, and bulbed off one more time before pan-drying the powder and crushing with mortar and pestle. The powder was then further dried using a tube furnace, the purpose of which was to remove any residual organics from the coprecipitation process. The furnace was ramped up to 500 °C at 180 °C/h, dwelled at 500 °C for 1 h, and then cooled down at 240 °C/h.

The sintering cycle used was as follows:

1. First segment ramped to 600 °C at 200 °C/min and to 10 MPa at 6.6 MPa/min.
2. Second segment dwelled at 600 °C and 10 MPa for 10 s.
3. Third segment ramped to 1,400 °C at 200 °C/min and 50 MPa at 10 MPa/min.
4. Fourth segment dwelled at 1,400 °C and 50 MPa for 1 minute; the rest of the cycle stayed at 50 MPa.
5. Fifth segment ramped to 1,900 °C at 200 °C/min.
6. Final segment dwelled at 1,900 °C for either 5, 10 or 15 min depending on the sample.

A summary of the samples made are listed in Table 3.1.

Table 3.1 Summary of the synthesized samples

Sample	Additives (wt%)	Dwell Time During Sintering Cycling (min)
N1P-5	10	5
N1P-10	10	10
N1P-15	10	15
N4P-5	5	5
N4P-10	5	10
N4P-15	5	15
N3P-5	3	5
N3P-10	3	10
N3P-15	3	15

A typical polishing route on for the samples was as follows:

- 5 min on 125-µm pad
- 10 min on 70-µm pad
- 15 min on 45-µm pad
- 20 min on 15-µm pad

The speed was 210 rpm for 125- to 15-µm pads and 4 lb per sample. The remaining polishing segments were all run at 150 rpm for the following times:

- 15 min on 9-µm pad at 5 lb per sample
- 10 min on 6-µm pad at 5 lb per sample
- 10 min on 6-µm pad at 5 lb per sample
- 15 min on 1-µm pad at 5 lb per sample
- 10 min on 0.25- µm pad at 5 lb per sample.

However, some samples required more time on certain steps to minimize the amount of scratches as well as the amount of pullout. This was monitored with an optical microscope.

The density of the sintered samples was determined using the Archimedes method. Hardness measurements were performed on a Leco hardness tester using a Knoop indenter at 1- and 2-kg loads. Hardness data were averaged over 20 measurements on each sample.

FESEM images were also obtained on the 10-wt% samples. Samples were removed from the mounted polished samples and carefully cut with a diamond saw, then cleaned by ultrasonification in acetone before mounting onto the SEM studs. The SEM used was a Zeiss Sigma FESEM (Carl Zeiss AG, Germany). Images of the 10-wt% sample were taken at a working distance of around 7 mm at an extra-high tension of 2.5 kV (see Figs. 3.3–3.5). Images of the remaining samples were not taken yet due to required repairs for the plasma etching system. The N1P images had better contrast due to the larger amount of additives.

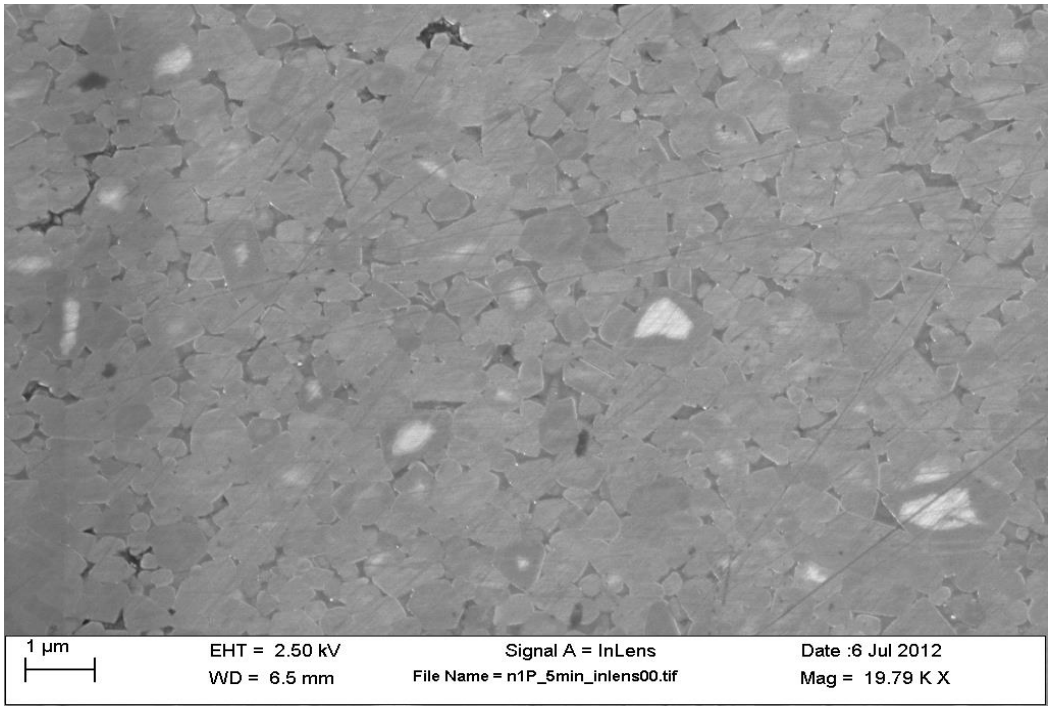

Fig. 3.3 In-lens FESEM image of the 10-wt%, 5-min dwell time sample with no prior etching

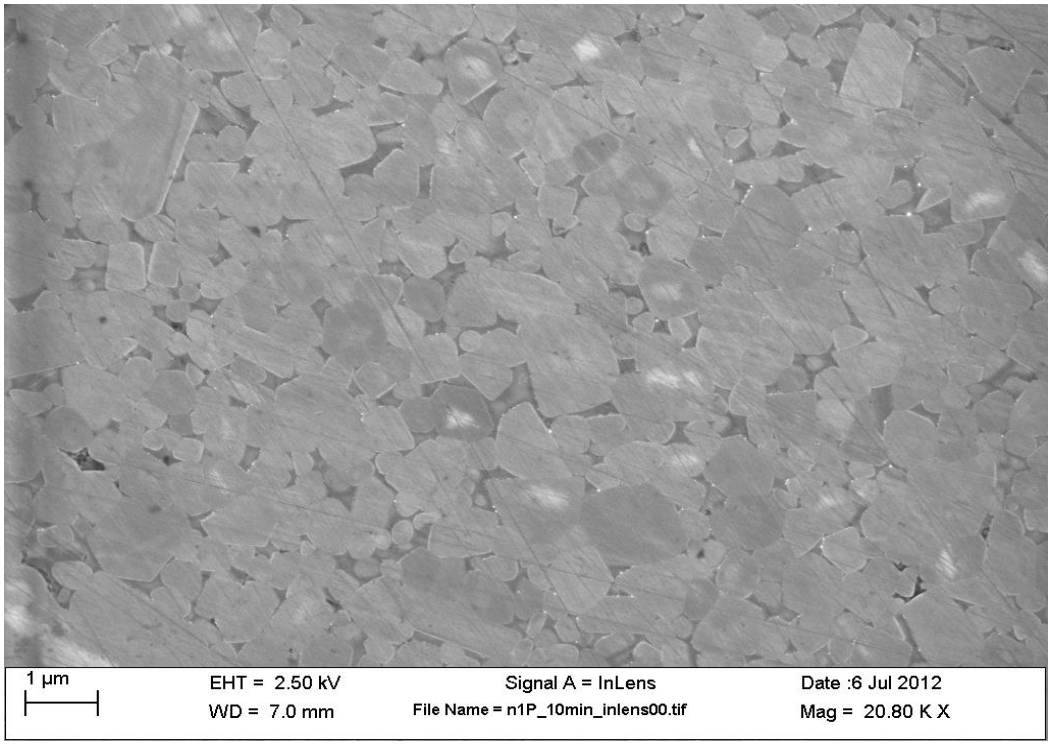

Fig. 3.4 In-lens FESEM image of the 10-wt%, 10-min dwell time sample with no prior etching

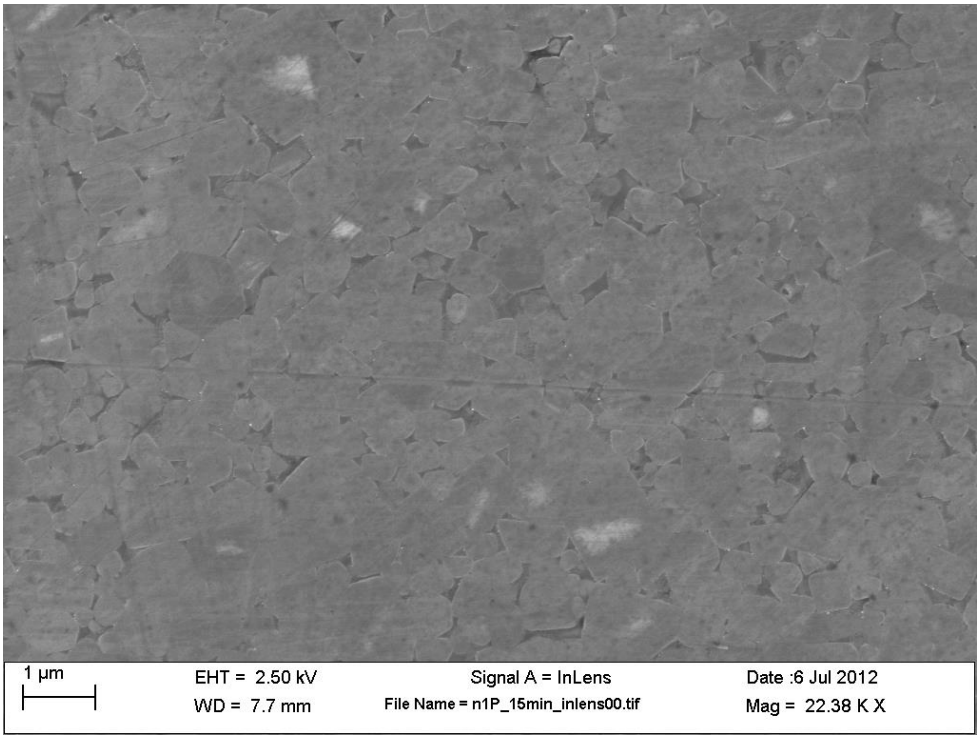

Fig. 3.5 In-lens FESEM image of the 10-wt%, 15-min dwell time sample with no prior etching

3.4 Results and Discussion

The results from the density and hardness measurements are presented in Table 3.2. Mean values are presented and error limits were estimated as standard error of the mean. A small decrease in the densities are seen with longer dwell times in the 5- and 10-wt% additives, but no significant difference in the 3-wt% additives sample. This may be an indication that whatever differences are observed are indeed due to the presence of the additives, and that there simply were not enough additives in the 3-wt% sample to discern any appreciable difference.

Table 3.2 Density and Knoop hardness of coprecipitated SiC samples

Sample	Density (g/cm^3)	Relative Density ($\%\rho_{th}$)	Knoop hardness (kgf/mm^2)
N1P-5	3.291 ± 0.002	97.6	1,542 ± 15
N1P-10	3.287 ± 0.002	97.5	1,569 ± 10
N1P-15	3.270 ± 0.003	97	1,02 ± 28
N4P-5	3.256 ± 0.001	100	1,773 ± 8
N4P-10	3.243 ± 0.001	99.7	1,750 ± 7
N4P-15	3.187 ± 0.001	97.9	1,785 ± 12
N3P-5	3.213 ± 0.003	99.3	1,773 ± 15
N3P-10	3.222 ± 0.003	99.6	1,639 ± 11
N3P-15	3.219 ± 0.002	99.5	1,757 ± 9

The 10-wt% sample does not show a significant decrease in density until a dwell time of 15 min. This could indicate that the diffusion process of AlN into the grains requires a dwell time of 10–15 min before we see start seeing it affect its density. While preliminary results show a decrease in density, it may go through a minimum density due to overheating effects of much longer dwell times.

The hardness results showed no clear trend with the dwell time in the samples. For the 10-wt% sample, the hardness increases with the sintering time, but, interestingly, the increase is much more pronounced from the 10- to 15-min dwell time despite having a decrease in density as noted. The 5-wt% sample shows no significant difference between the 5- to 15-min sample but both of these are have a higher hardness than the 10-min sample. This relation is also seen in the 3-wt% sample. It is possible that these discrepancies are due to competing sintering mechanisms that are sensitive to the amount of additives present.

FESEM images of the 10-wt% sample are shown in Figs. 3.3–3.5. The most apparent distinction between the images is that of the grains exhibiting a core-rim structure, the boundary between the core and rim is much sharper and more distinct in the samples with shorter dwell times. As the dwell time increases, the boundary becomes fuzzier, which likely indicates diffusion occurring. The grain boundaries are also much more distinct with shorter dwell times, which could be an indication that not as much solution reprecipitation occurred compared to samples that had sufficient time for reprecipitation to take place.

3.5 Future Work

Plasma etching on all samples will be done to obtain suitable SEM images on all samples. Chemical analysis via energy dispersive x-ray spectroscopy on the SEM will also be carried out to gain a better understanding of the diffusing atoms during the sintering process. A larger increment in the dwell time of samples will also be used to examine more significant differences in densities and hardness. Additionally, plans to use a hydrogen fluoride wash for the powders are under consideration for removing excess oxygen and metal impurities. Physical and mechanical properties of the sintered samples will be evaluated and correlated with the diffusion behavior of the sintering additives.

3.6 References

1. Opportunities in protection materials science and technology for future Army applications. Washington (DC): National Research Council; 2011. [accessed 2012]. http://www.nap.edu/openbook.php?record_id=13157&page=R1.

2. Mercurio SR, Ph.D. [Thesis]. [New Brunswick (NJ)]: Rutgers University; 2011.

3. Shaffer PTB. A review of the structure of silicon carbide. Acta Cryst. 1969;B25:477–488.

4. Hu J, Gu H, Chen Z, Tan S, Jiang D, Rühle M. Core-shell structure from the solution-reprecipitation process in hot-pressed AlN-doped SiC ceramics. Acta Materialia. 2007;55(16):5666-5673.

4. Task 3: Education and Outreach Activities, Core Program

Core Faculty: R Haber, D Niesz

ARL Leaders: J McCauley, J LaSalvia

4.1 Long-Range Objectives

- Educational components, as determined
- Outreach component, national and international activities

4.2 Objectives for the Period

- Hold one-day topical workshop of the Ceramic Armor Industrial Subgroup of the Rutger University's Ceramic and Composite Materials Center (CCMC) at the Cocoa Beach/Daytona Meeting of the American Ceramic Society.
- Hold one-day topical workshops of the Ceramic Armor Industrial Subgroup at Rutgers University.
- Hold one-day topical workshop at the US Army Research Laboratory (ARL).

4.3 Progress on Objectives

4.3.1 Ceramic Armor Industrial Group Workshops

This group has been formed as a subgroup within the Ceramic, Composite and Optical Materials Center (CCOMC). It is serving as a focal point for outreach to the industrial armor producers. It is also being used to identify and focus on key scientific and technical issues for ceramic armor manufacture and to provide real-time feedback to the armor producers for the results of this program. BAE Systems, Ceradyne/ESK Ceramics, CoorsTek, Corning, M Cubed, Morgan Advanced Materials, Schott North America, Saint Gobain, Kennametal, Industrie Bitossi, Superior Graphite, Greenleaf, Washington Mills, and the US Army (ARL, US Army Tank Automotive Research, Development and Engineering, and the Natick Soldier Center) are the current members of the group. Several other companies are considering membership. A one-day workshop that focused on transparent ceramics was held for the group in conjunction with a meeting of the Engineering Ceramics Division of the American Ceramic Society on 26 January 2012. At this meeting the National Academy of Science study on Protection Materials Science

and Technology for Future Army Applications was presented. The workshop had 99 attendees. A second workshop was held on 25 April 2010 at Rutgers University in conjunction with the semiannual review meeting of the CCMC. A third workshop was held at Clemson University in conjunction with the semiannual review meeting of the CCMC on 31 October 2012

4.3.2 Review/Planning Meetings

A review meeting/workshop was held at ARL on 8 June 2012.

5. Task 4: MoD Mod-Shared with the Ceramic, Composite and Optical Materials Center (CCOMC)

Primary Investigator: Richard A Haber, Rutgers University

Researcher: Douglas M Slusark, graduate student

5.1 Long-Range Goal

This project aims to define the upper limit of acceptable defects (i.e., porosity and inclusions) in commercial microstructures of SiC used in armor applications. The key goal within this program is to develop an understanding of the factors critical to the design, fabrication, and testing of micro-/macro-tailored ceramics with enhanced multihit dynamic performance. This understanding will establish a good/bad acceptance criterion for the selection of armor materials.

5.2 Background

A study was undertaken to determine if a correlation exists between nondestructive evaluation by ultrasound and mechanical properties and microstructure in commercially available SiC armor plates. The aim of the work is to determine the contribution of porosity, inclusions such as boron carbide (B_4C) and carbon (C), and grain size to the strength and acoustic properties of these materials. This study was performed to build upon the work done at Rutgers by MV Demirbas and RA Brennan. Demirbas used a number of techniques for the quantification of a microstructure and the spatial analysis of defects. These techniques included nearest-neighbor distance distributions, tessellation analysis, average pore size, and pore size distributions. It was found that these methods did provide indications as to whether a microstructure was clustered or random.[1,2,3] In collaboration with RA Brennan, a sintered SiC tile was examined by ultrasound scanning to determine if a link existed between C-scan image maps and microstructural quantification methods. A distinction was made between “high” and “low” amplitude regions in the nondestructive evaluation (NDE) image maps. Serial sectioning of the tile was performed to determine if a difference in microstructure existed between the 2 regions. Statistical analysis showed that the difference in size of the largest defect between the high and low regions was significant, while it was also found that clustering of defects did occur in certain low amplitude regions.[4]

5.3 Initiation of Study/NDE/Tile Selection

Forty-one pressureless-sintered SiC tiles were received from Saint-Gobain in July 2008. All tiles were approximately 101.5 × 101.5 × 14 mm. Archimedes density measurements by immersion were carried out on all 41 tiles, resulting in an average value of 3.17 g/cm^3.

NDE of the tiles was carried out by ultrasound C-scan using an Olympus 20-MHz planar unfocused transducer in pulser/receiver configuration. Scanning parameters included a 0.1-mm lateral step size, resulting in NDE maps containing more than one million data points. The transducer used has a frequency range of 16–32 MHz, as shown in Fig. 5.1. The bandwidth of the transducer was determined at the wavelengths where the emission had decreased to 1/4 the amplitude at the central frequency.[5]

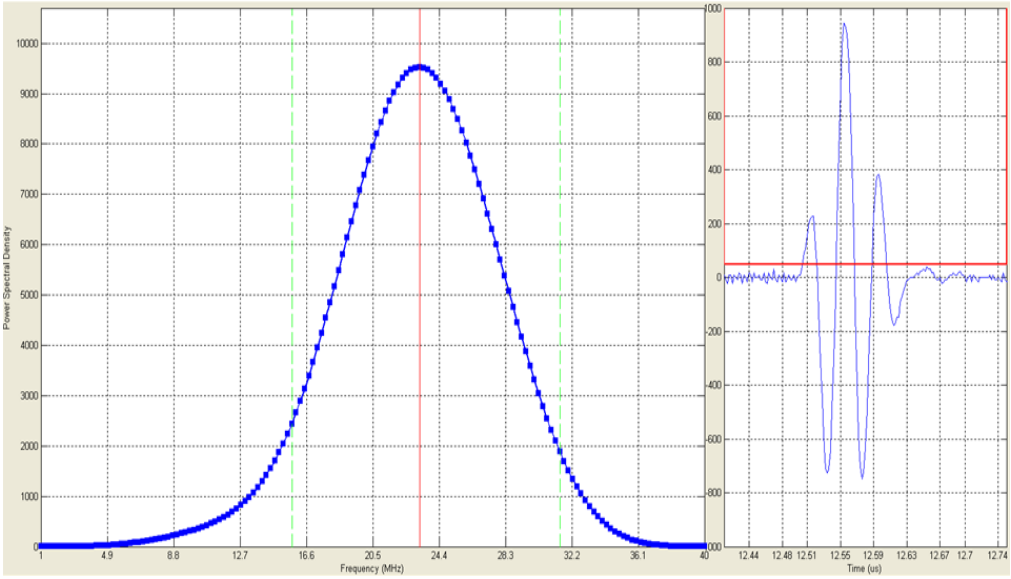

Fig. 5.64 Acoustic spectrum of Olympus ultrasound transducer[5]

At each scanning position, an oscilloscope trace of amplitude versus time, or A-scan, is recorded. A representative A-scan, shown in Fig. 5.2, contains characteristic peaks that correspond to reflections of ultrasound energy from the top and bottom surfaces of the tile. From the position of the surface reflection peaks, it is possible to determine the longitudinal wave and shear wave times of flight ($TOF_{Longitudinal}$ and TOF_{Shear}), as well as the thickness of the sample (x). Knowing these, the longitudinal (c_L) and shear velocity (c_S) can be calculated, and from these, Poisson's ratio (υ) and the elastic modulus (E).[6,7]

$$c_L = \frac{2x}{TOF_{Longitudinal}} . \quad (1)$$

$$c_S = \frac{2x}{TOF_{Shear}} . \quad (2)$$

$$\nu = \frac{1-2\left(\frac{c_S}{c_L}\right)^2}{2-2\left(\frac{c_S}{c_L}\right)^2} . \quad (3)$$

$$E = {c_L}^2 \rho \frac{(1-2\nu)(1+\nu)}{(1-\nu)} . \quad (4)$$

$$\alpha = -\frac{8.686}{2x} ln\left(\frac{A}{A_0}\right)^2 . \quad (5)$$

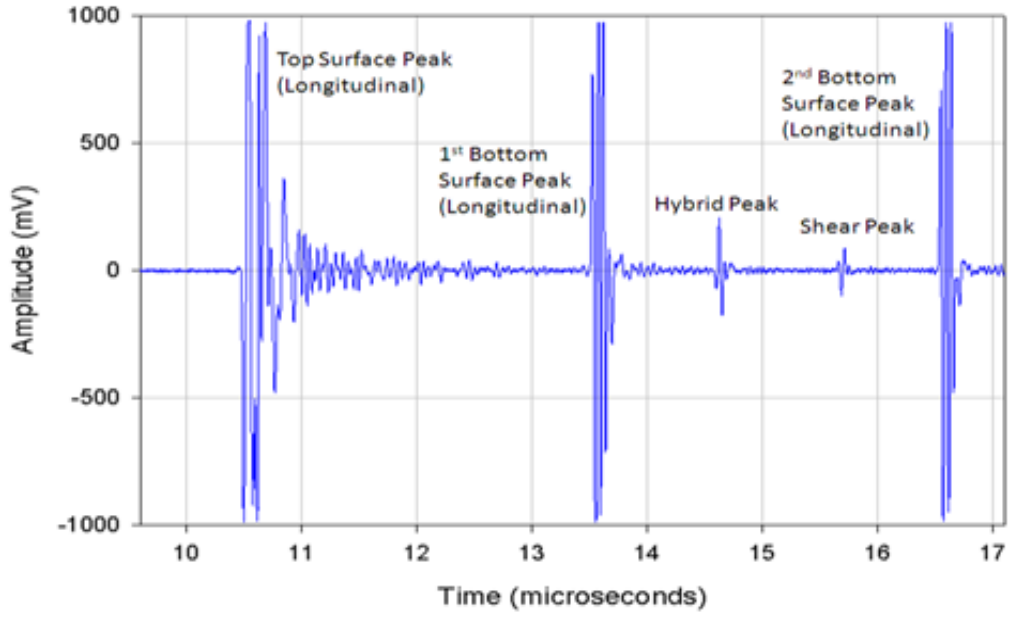

Fig. 5.65 Representative ultrasound trace[5]

Where this work differed from previous NDE studies done at Rutgers was in the use of the acoustic attenuation coefficient (α). In the work of Demirbas and Brennan,[4] areas of the tile were chosen for serial sectioning and microstructural analysis based upon the amplitude of the first bottom surface reflection peak. In contrast, the acoustic attenuation coefficient is calculated by using a modification of the Beer-Lambert law.[8] This involves taking a ratio of the amplitude of the first and second bottom surface reflection peaks. It was found that this method was less susceptible to surface finish irregularities than previously employed methods.[9]

Following the scanning process, the data was compiled into ultrasound NDE maps. At the time that this study was taking place, these ultrasound methods represented the state of the art. Based upon these results, 6 group headings were devised with

the tiles divided into the 6 groups. Groups 1–4 were compiled based upon the quantitative results of the NDE scans. Groups 5 and 6 were chosen based upon differences seen in the NDE maps. The group headings were the following:

1) High mean attenuation coefficient
2) High mean longitudinal velocity/Young's modulus
3) High mean shear velocity/shear modulus
4) Low mean attenuation coefficient
5) High zone variations
6) Low zone variations

As the tiles within each group showed differences in acoustic properties, it was hoped that they would show a corresponding difference in mechanical properties.

One tile from each group was designated for machining into ASTM B-type modulus of rupture (MOR) bars.[12] In some instances, a tile may have had the highest average value in more than one category. When this occurred, a tile with a slightly lower value was selected for machining. The breakdown of which tile from each group was chosen for machining was Group 1: tile 8; Group 2: tile 11; Group 3: tile 4; Group 4: tile 31; Group 5: tile 2; and Group 6: tile 19.

The NDE maps for these 6 tiles can be found in Figs. 5.3–5.8. As detailed in Table 5.1, the NDE maps for Groups 1, 4, 5, and 6 are attenuation coefficient maps, while the maps for Groups 2 and 3 are longitudinal velocity and shear modulus maps, respectively. The scale has been tailored for each individual map ne to account for the spread in values in each map, along with highlighting map features such as regions of variation and the presence of any acoustic anomalies. Included in Table 5.1 are the scales used in each map, the average value, and the standard deviation.

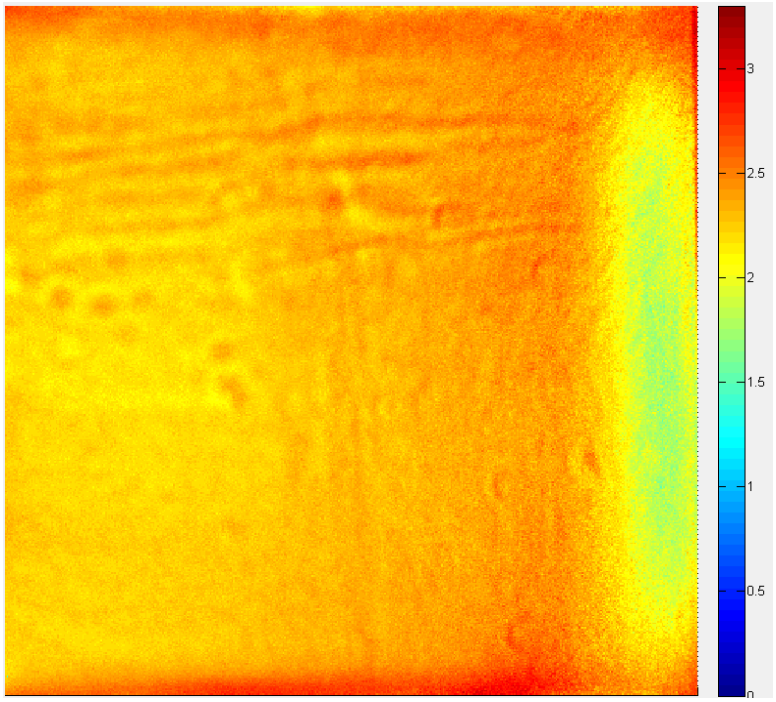

20MHz Attenuation Coefficient NDE Map

Fig. 5.66 Group 1, tile 8; high mean attenuation coefficient

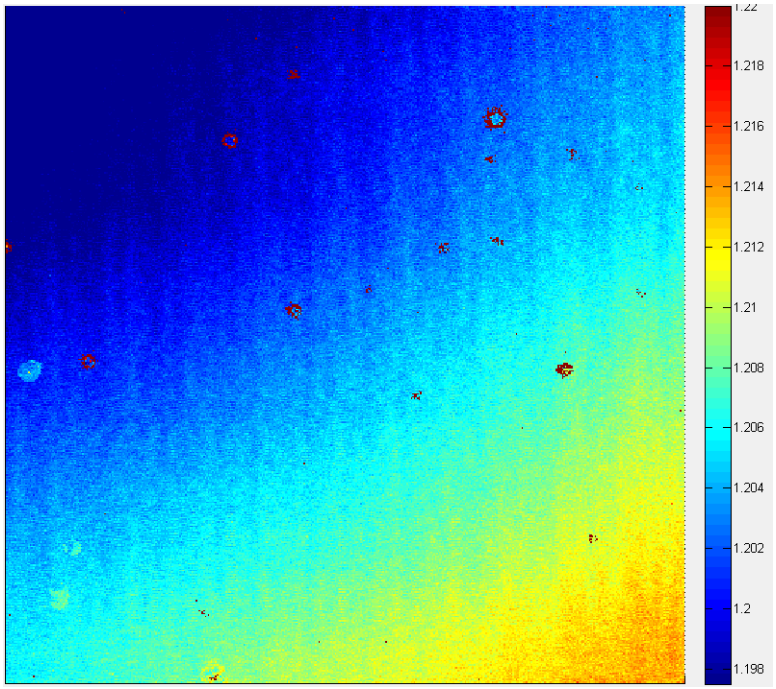

Longitudinal Velocity NDE Map

Fig. 5.67 Group 2, tile 11; high mean longitudinal velocity

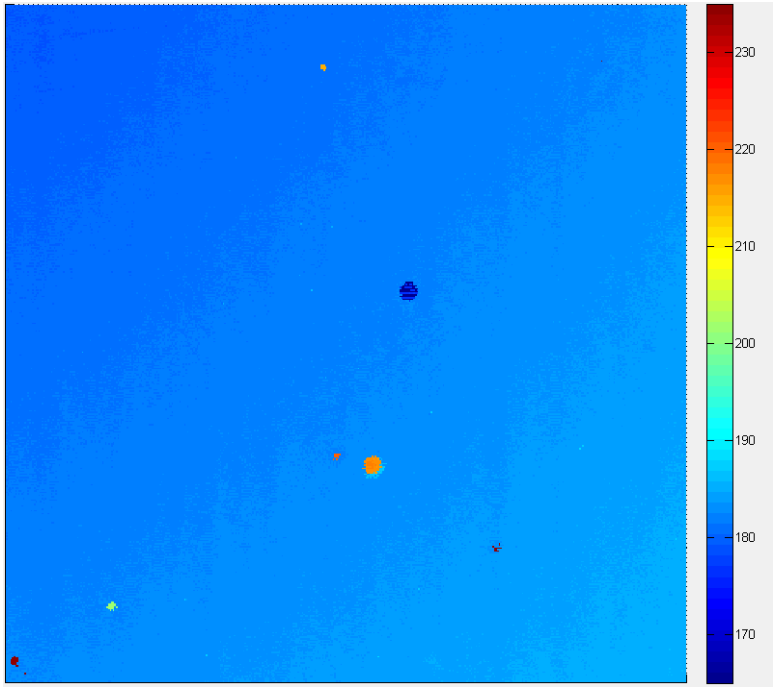

Shear Modulus NDE Map

Fig. 5.68 Group 3, tile 4; high mean shear modulus

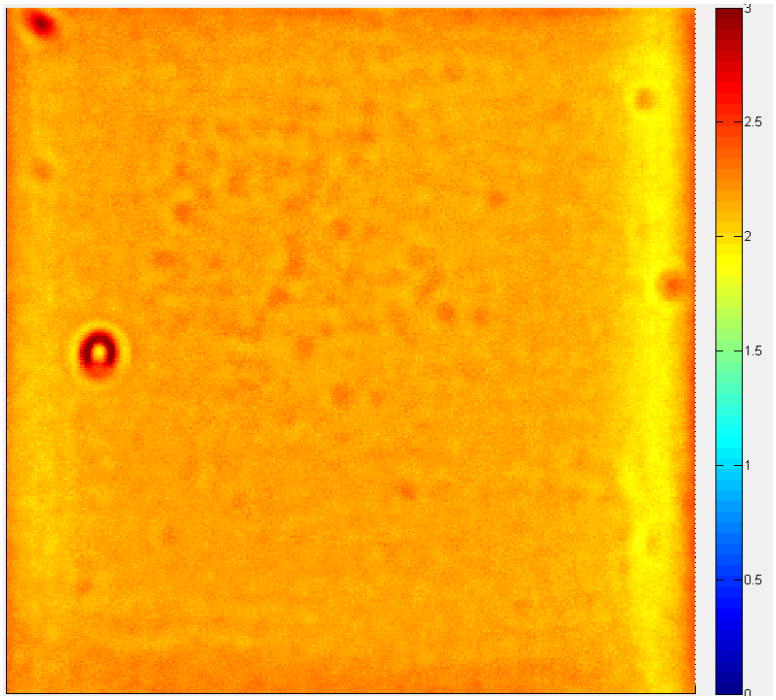

20MHz Attenuation Coefficient NDE Map

Fig. 5.69 Group 4, tile 31; low mean attenuation coefficient

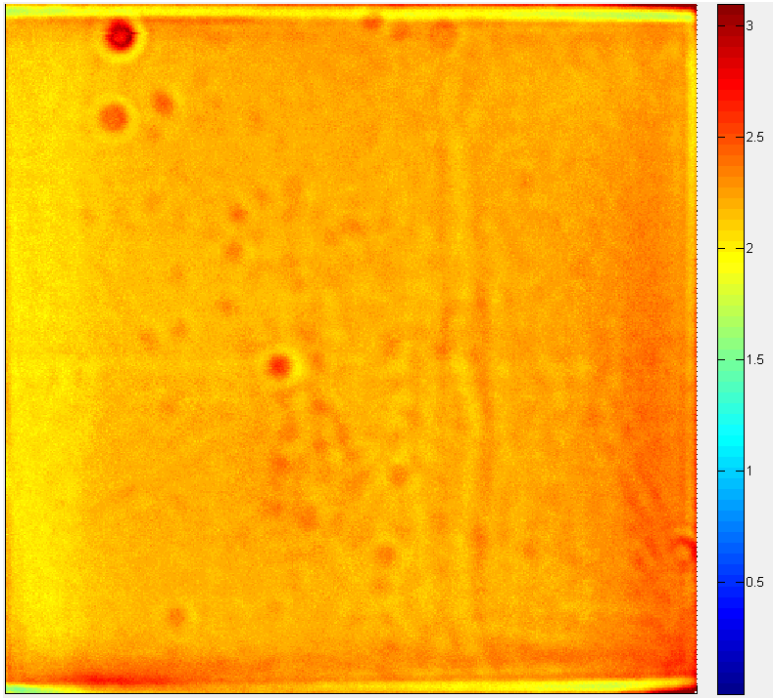

20MHz Attenuation Coefficient NDE Map

Fig. 5.70 Group 5, tile 2; high zone variations

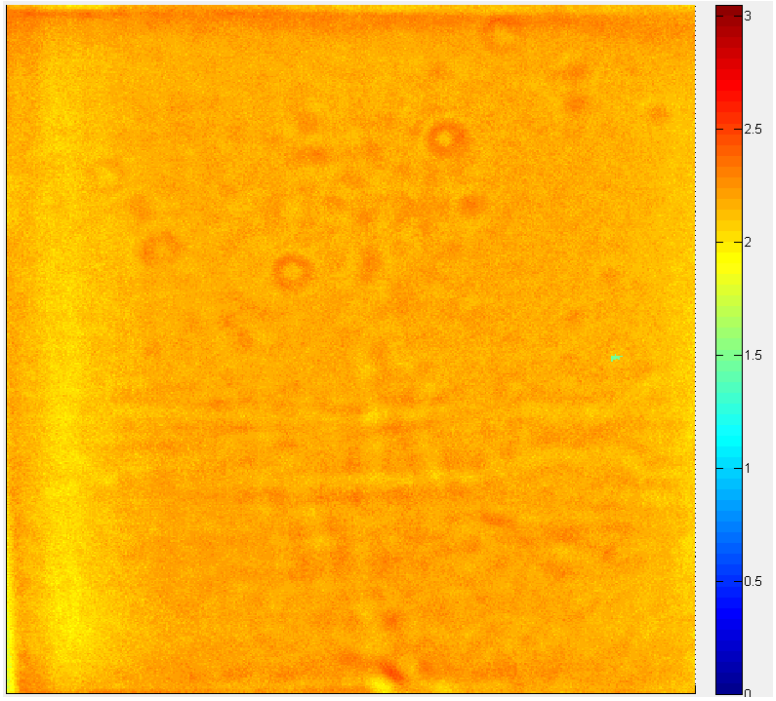

20MHz Attenuation Coefficient NDE Map

Fig. 5.71 Group 6, tile 19; low zone variations

Table 5.1 Group breakdown/NDE map type and values

Tile No.	Type of Map	Unit	Scale (max)	Scale (min)	Average Value	Std. Dev.
8	Att. coefficient	dB/cm	3.25	0	2.31	0.09
11	Speed of sound	m/s	12,200	11,975	12,044	113
4	Shear modulus	GPa	235	165	182	3
31	Att. coefficient	dB/cm	3.00	0	2.15	0.05
2	Att. coefficient	dB/cm	3.10	0	2.21	0.07
19	Att. coefficient	dB/cm	3.05	0	2.17	0.05

5.4 Bend Bar Machining

The selected tiles were machined into B-type bend bars (50 × 4 × 3 mm).[10] As shown in Fig. 5.9, tile 11 (the first tile processed) was machined into 102 bend bars: 17 rows of bars, a left and a right column, and a top, middle, and bottom layer of bars. The remaining 5 tiles (2, 4, 8, 19, and 31) were machined into 108 bend bars. The machinist was able to reduce the distance between slices, resulting in an extra row of bars. The additional row of bars had the effect of improving the resolution of the MOR analysis and microstructural evaluation. Overall, the machining operation of the 6 tiles resulted in 630 bend bars, as 12 bars were lost to machining difficulties.

One of the key aspects of the machining process was to keep track of the position, identity, and orientation of the bend bars in relation to the original tile. This was to allow for the correlation of the properties of the bend bars to features within the NDE maps.

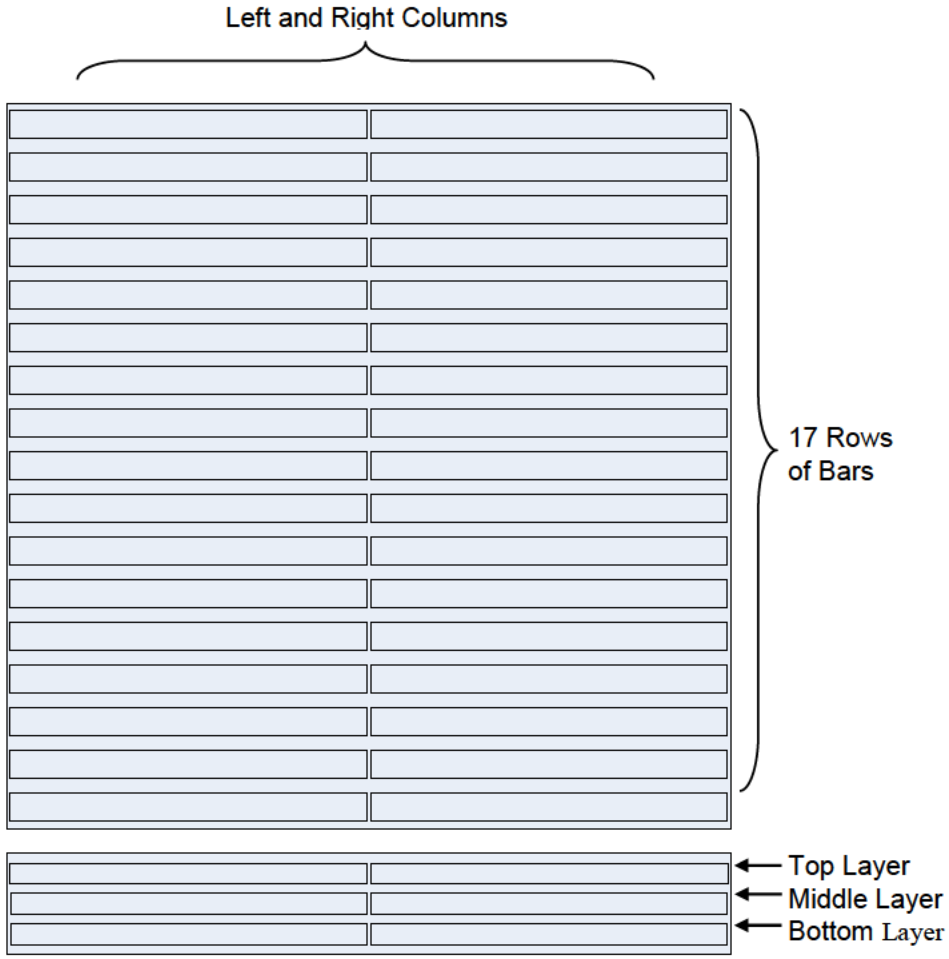

Fig. 5.72 Bend bar machining diagram, tile 11

5.5 MOR/Weibull Analysis

After machining, 4-pt flexure testing was carried out to determine the MOR of each bar. This testing was done on an Instron 4500/4505 testing system, using a semiarticulating test fixture with a crosshead speed of 0.5 mm/min. A further 6 bars were destroyed without result during flexure testing. The MOR results for the remaining 624 bars are shown in Tables 5.2–5.7, which contain the minimum, maximum, average strength, and standard deviation for each layer of bars from each tile. The ranking of the tiles by average strength, in order from strongest to weakest, is 2, 4, 19, 11, 8, and 31.

Table 5.2 Tile 8. MOR/Weibull moduli

MOR Summary	Max.	Min.	Avg.	Std. Dev.	m
Top layer	569	357	480	50	11.5
Middle layer	565	255	458	59	8.0
Bottom layer	555	246	466	64	7.6
Entire tile	569	246	468	58	8.7

Table 5.3 Tile 11. MOR/Weibull moduli

MOR Summary	Max.	Min.	Avg.	Std. Dev.	m
Top layer	564	275	471	67	7.8
Middle layer	600	246	466	92	5.2
Bottom layer	565	279	475	64	8.2
Entire tile	600	246	470	75	6.9

Table 5.4 Tile 4. MOR/Weibull moduli

MOR Summary	Max.	Min.	Avg.	Std. Dev.	m
Top layer	595	287	486	68	7.8
Middle layer	583	351	489	56	10.4
Bottom layer	592	333	484	68	8.2
Entire tile	595	287	488	61	10.3

Table 5.5 Tile 31. MOR/Weibull moduli

MOR Summary	Max.	Min.	Avg.	Std. Dev.	m
Top layer	537	367	452	47	11.5
Middle layer	576	370	454	56	9.7
Bottom layer	522	314	435	60	8.6
Entire tile	576	314	447	55	9.9

Table 5.6 Tile 2. MOR/Weibull moduli

MOR Summary	Max.	Min.	Avg.	Std. Dev.	m
Top layer	561	389	483	49	11.7
Middle layer	561	408	497	33	18.5
Bottom layer	595	431	504	45	13.5
Entire tile	595	389	494	43	14.0

Table 5.7 Tile 19. MOR/Weibull moduli

MOR Summary	Max.	Min.	Avg.	Std. Dev.	m
Top layer	581	369	490	56	10.4
Middle layer	555	284	470	55	9.3
Bottom layer	537	325	467	53	10.5
Entire tile	581	284	475	55	10.3

Weibull statistics were used to analyze the MOR results to examine the distribution of strength within each tile and throughout the total data set. Weibull diagrams for each group of bend bars are shown in Figs. 5.10–5.15. For many of the tiles, it was originally found that a bimodal Weibull distribution better represented the strength data. This was reflective of the high degree of spread within the data, despite the fact that the original 6 tiles were fully dense production tiles of the same material. A significant amount of fractography work went into determining the causes of the bimodal distributions using a stereo optical and FESEM. It was eventually found that errant, deep machining scratches on the tensile and side surfaces of particular bend bars led to the bimodal distributions.

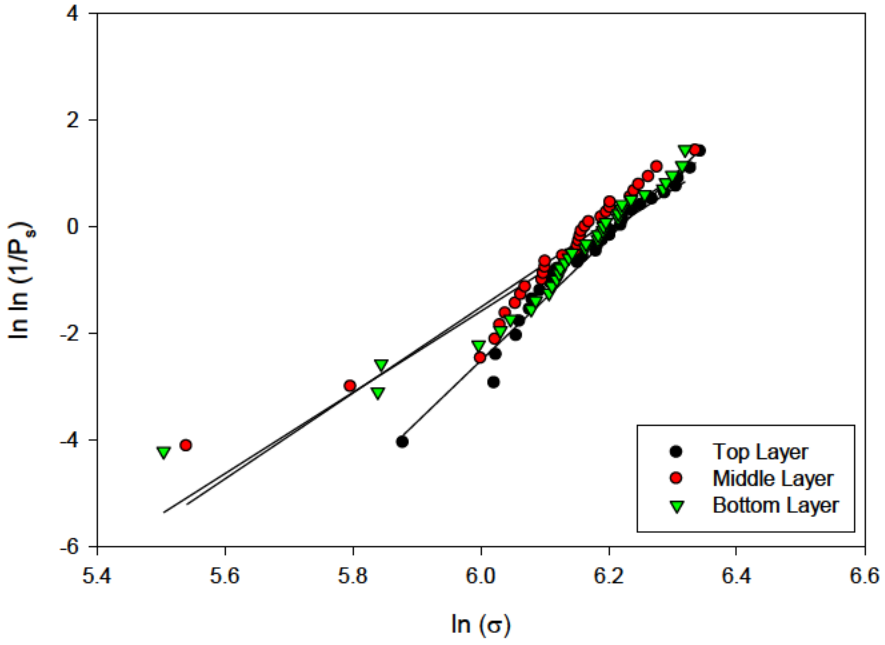

Fig. 5.73 Weibull analysis: Group 1, tile 8

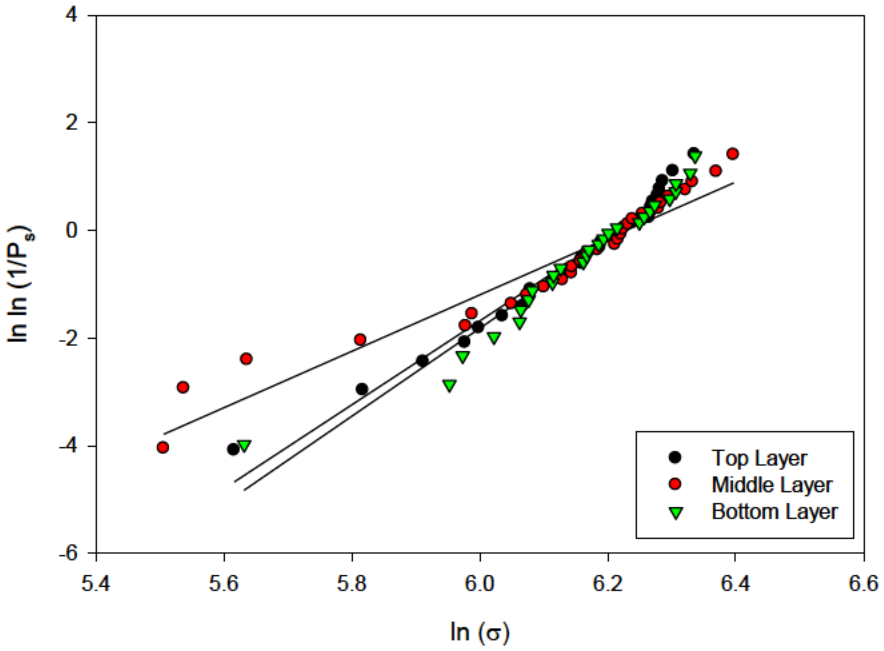

Fig. 5.74 Weibull analysis: Group 2, tile 11

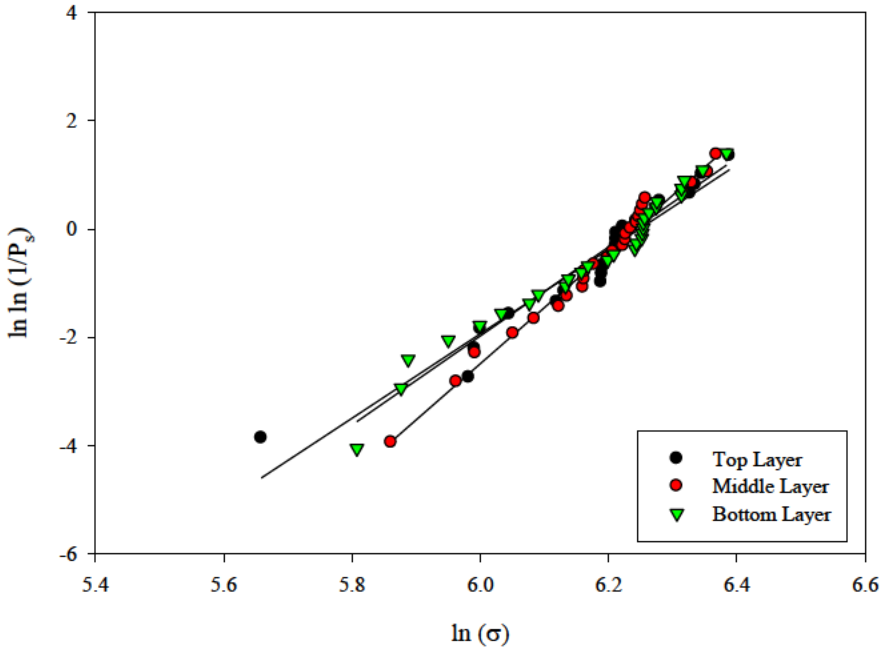

Fig. 5.75 Weibull analysis: Group 3, tile 4

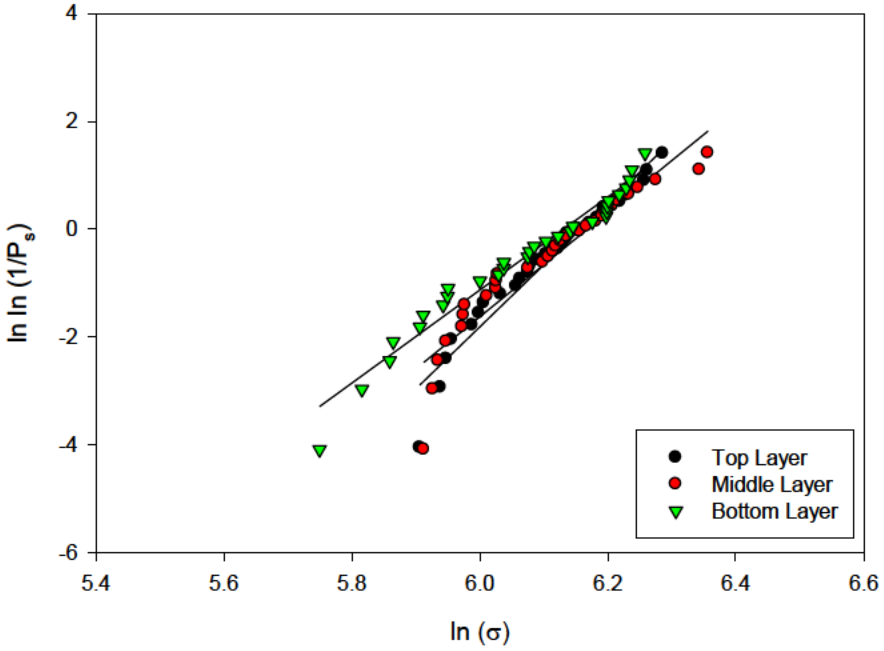

Fig. 5.76 Weibull plot: Group 4, tile 31

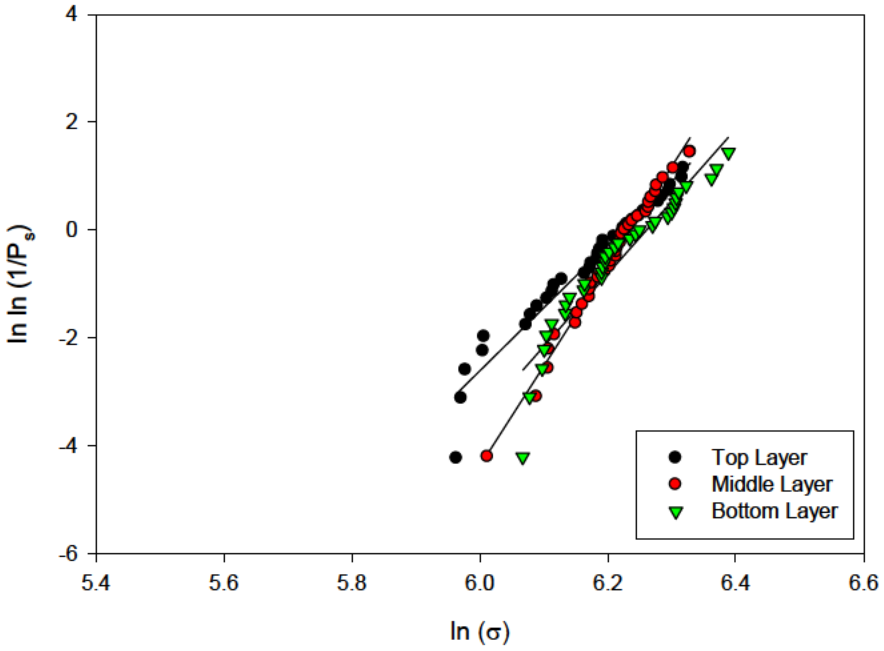

Fig. 5.77 Weibull plot: Group 5, tile 2

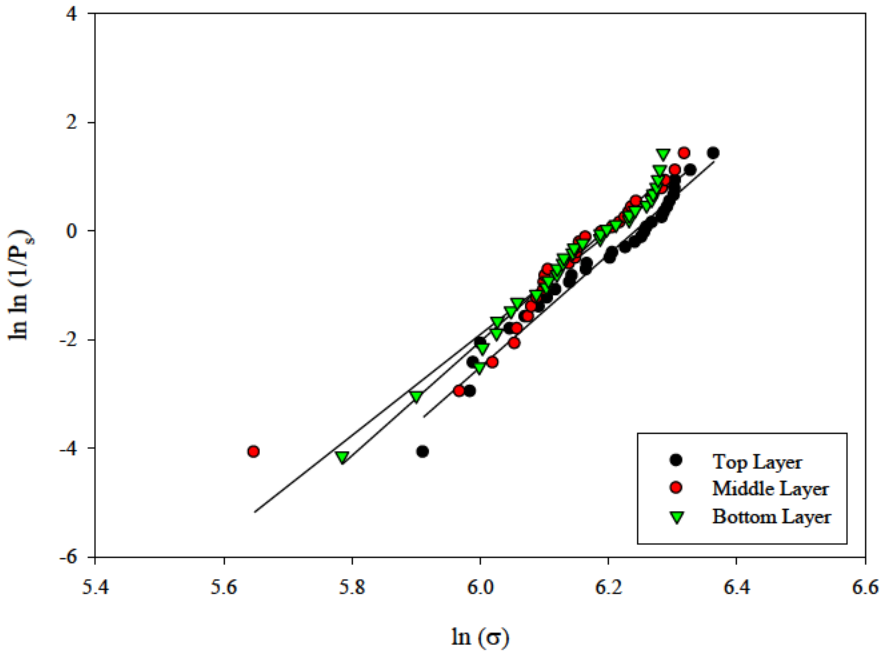

Fig. 5.78 Weibull plot: Group 6, tile 19

Figure 5.16 shows a FESEM image of the tensile surface of a very low strength, broken bend bar, containing a very evident example of this type of damage. There are a number of scratches that can be seen in the image, 2 of which have been indicated by long black arrows. Although these scratches can be challenging to discern in the FESEM, they become much more evident when viewed with an optical microscope. The scratch believed to have been the initiation point of fracture makes an angle of approximately 75° with the long axis of the bend bar. In the area the crack initiated, it followed the machining scratch for a period of time. This is denoted by the 2 short horizontal arrows in the image. As the applied stress field changed during fracture, the fracture initiating crack changed direction and grew perpendicularly to the long axis of the bend bar.

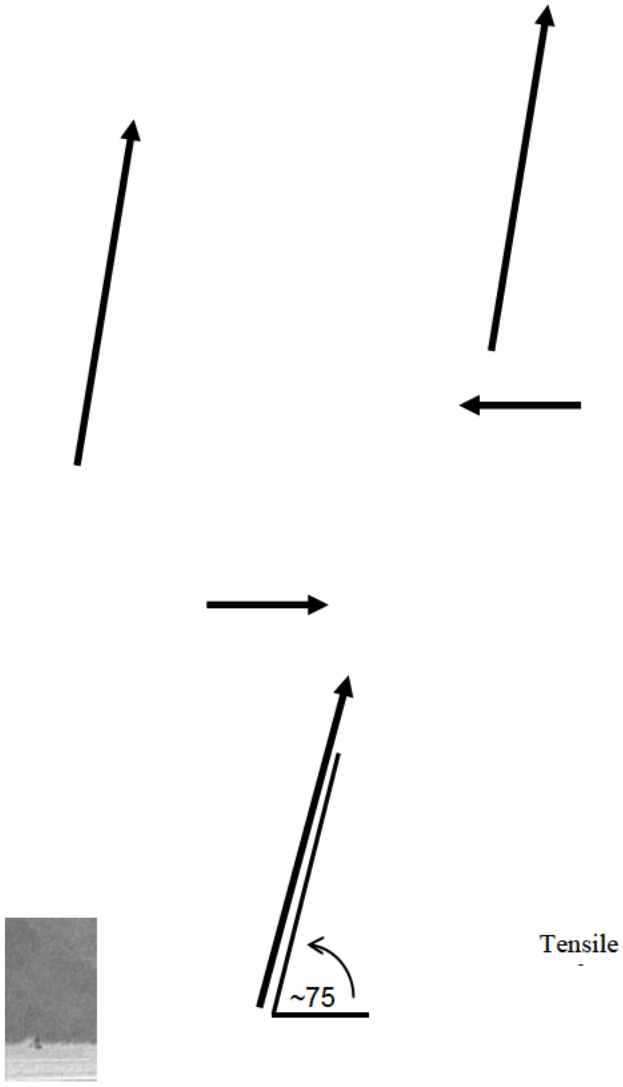

Fig. 5.79 Errant machining scratch on tensile surface of low-strength bend bar (A)

Confirmation that this was most likely the fracture initiation location is shown in Fig. 5.17, which contains a FESEM image of the 2 sides of the primary fracture location for the bend bar discussed in the previous paragraph. A broad fracture plane, shown by the dashed line, can be found on both end faces, which is indicative of low fracture strength.[11] As indicated by the arrows, texture on the surface indicates that fracture began at the tensile surface near the center of the bar. This is an agreement with the approximate location determined from the previous image.

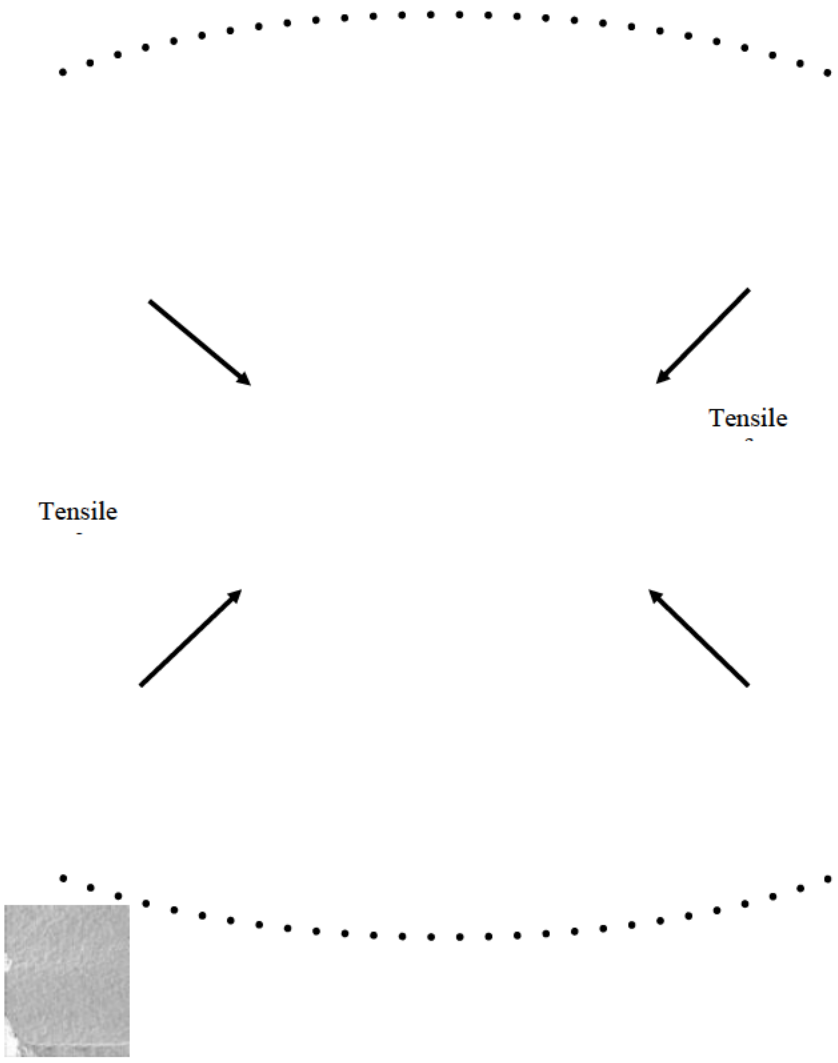

Fig. 5.80 Fracture surface, left (top) and right (bottom) faces of low-strength bend bar (A)

A second type of errant machining scratch is shown in Fig. 5.18. This figure is a FESEM image of the side of another low-strength, broken bend bar. In this case, the side of the bend bar was scratched at a perpendicular or high angle to the long axis of the bend bar, along the whole side of the bar. In this example, 2 evident scratches can be seen. A 30-μm-wide scratch runs down the side of the bend bar, the fracture path following the scratch for the first 0.5 μm of travel and then branching off. Even if this scratch was not present, there is also a 15-μm-wide scratch that would have most likely caused fracture. This damage had to be induced before the chamfering operation for the scratch to reach the tensile surface.

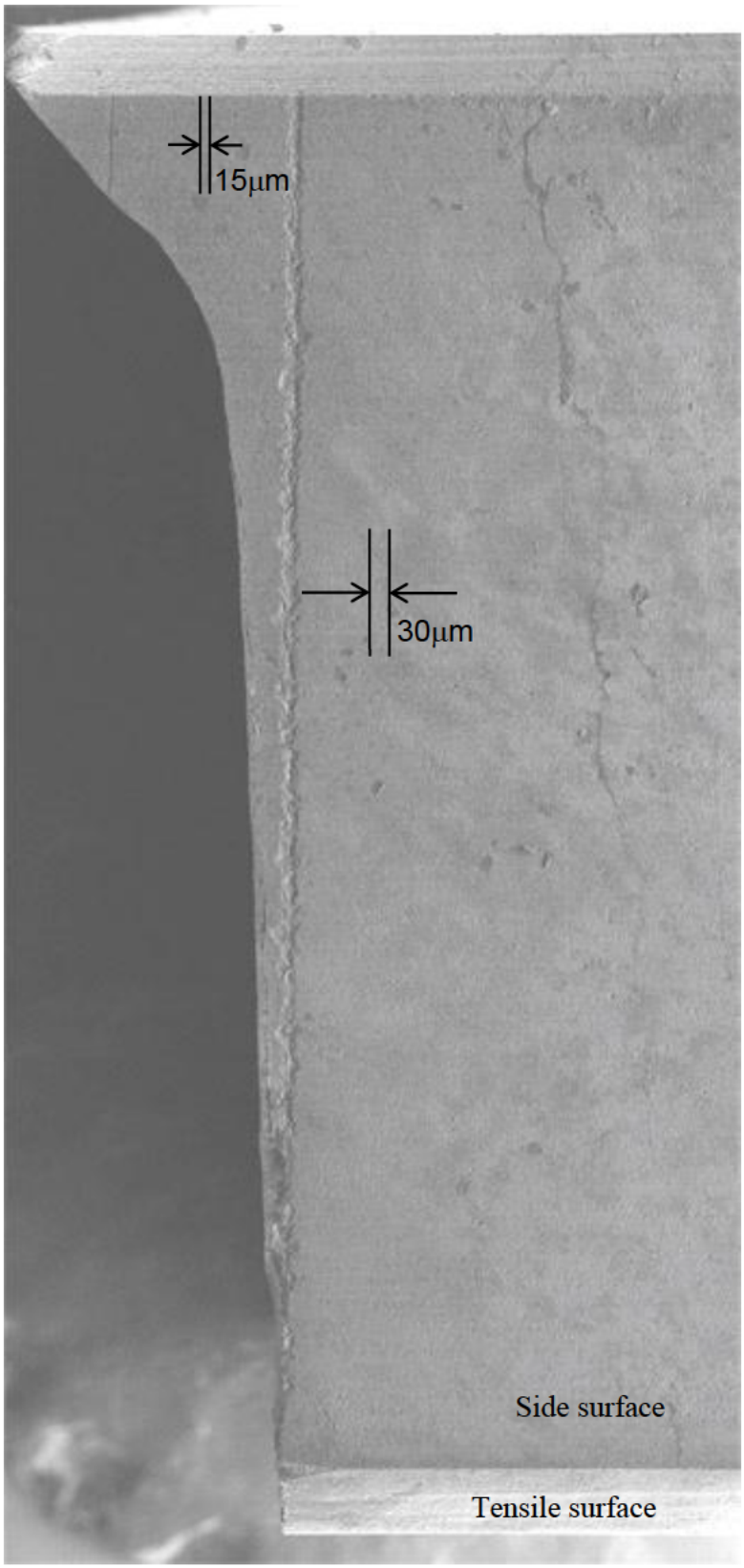

Fig. 5.81 Errant machining scratch on tensile surface of low-strength bend bar (B)

FESEM images of the left and right faces of the fracture surface of this bend bar are shown in Fig. 5.19. When the fracture surfaces for this bar were first examined, the fracture behavior was initially puzzling as the bars appeared to have fractured from the side. It is now known that this bar did in fact break from the lower corner, as shown in the previous image. As this was a low-strength bar, the fracture surface is characterized by a broad flat fracture plane, as indicated by the dashed line.

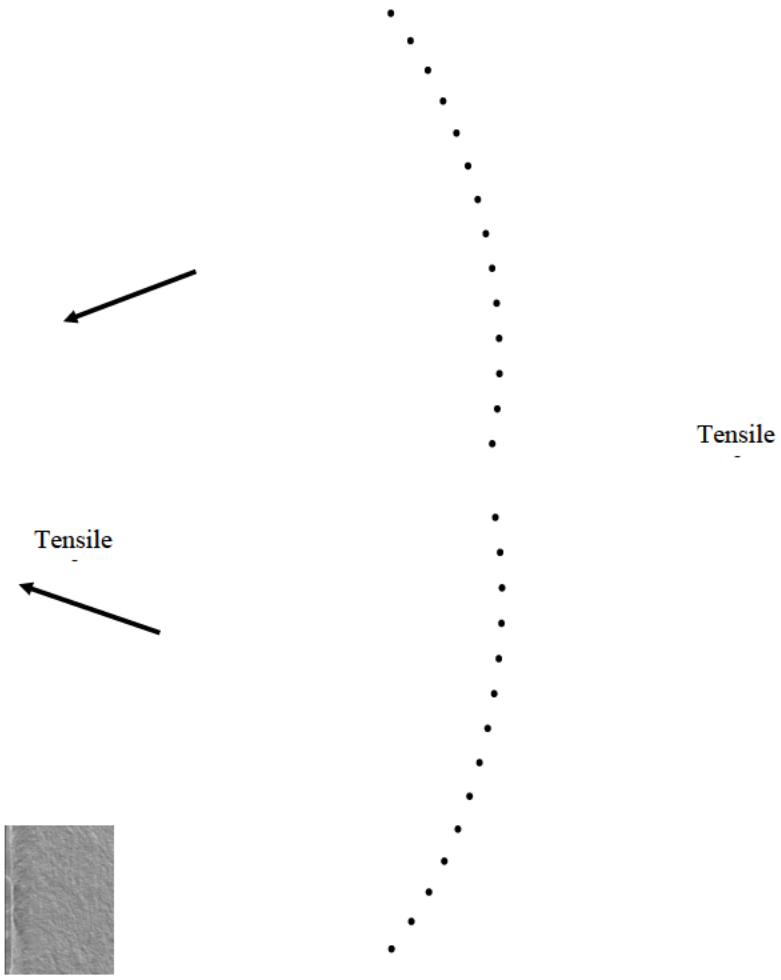

Fig. 5.82 Fracture surface, left (top) and right (bottom) faces, of low-strength bend bar (B)

As can be expected, this damage had a deleterious effect on the strength values for the different sets of bars, especially considering that the damage occurred on the tensile or lower-side surface of the bars. Seventy-seven bars where found to have fractured from either errant tensile or side surface scratches. Table 5.8 contains a breakdown of each type for the 6 groups of bend bars. For some tile groups, the number was close to 20% of the bars. In addition, 3 bend bars were found to have

a “step” machined into the side of the bar, as shown in Fig. 5.20. This resulted in a nonuniform stress distribution through the bar during the test, so these results have also been removed from the bend strength statistics.

Table 5.8 Erroneous machining damage

Type of Damage	Tile 8	Tile 11	Tile 4	Tile 31	Tile 2	Tile 19
	(no. of bars)					
Side	5	9	19	6	1	10
Tensile	7	3	1	10	4	2

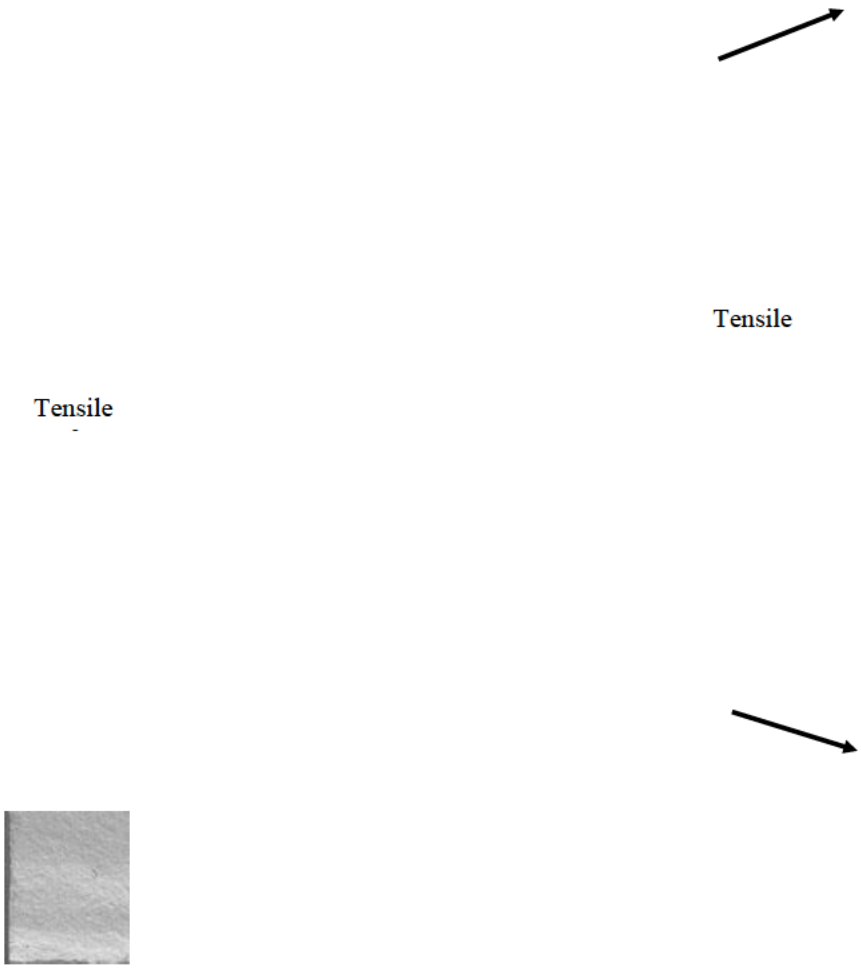

Fig. 5.83 Fracture surface, left (top) and right (bottom) faces in low-strength bend bar (C)

In total, almost 13% of the bars in the study had one of these types of damage. Removing the MOR values for these values had an effect on the Weibull statistics. The Weibull moduli increased for all tile groups, and any bimodal Weibull distributions were replaced with unimodal distributions. It should be noted that the errant machining scratches documented in this section are considered an anomaly as they are not representative of machining damage that one would expect to find in a longitudinally ground ASTM B-type MOR bend bar.

5.6 Primary Fracture Location/NDE Map Overlay Diagrams

As part of the strength testing analysis, the primary fracture position was determined for each bend bar. This is considered to be the fracture position that contains the fracture initiating feature. In this exercise, each piece of a broken bar must be examined. As a general rule, for a low-strength bar, the primary fracture position is the only fracture position. However, a proportionate amount of energy is built up in a bar as the applied stress increases before fracture. When fracture does occur, the shockwave caused by the sudden release of energy can result in the occurrence of secondary fractures, which may break the bar into many pieces.

If there are multiple fracture locations, it is necessary to determine at which location fracture began. ASTM Standard C1161[10] contains examples of fracture behaviors in a 4-point bend test that can aid in this determination. Fracture behavior may differ whether it was a high-, medium-, or low-energy fracture. The presence of cantilever curls and the relation between the fracture position and the location of the loading pins can also offer clues when determining the primary fracture position. Fracture may also occur outside of the loading pins. This may be the result of misalignment of the test setup, in which case the MOR value must be removed from the Weibull statistics or, due to the presence of a large flaw, located outside of the primary loading zone of the test. When testing a B-type bend bar, this is a volume that is approximately 20 mm long and 4.0 mm wide that experiences the full applied stress just before the initiation of fracture. In the instance where there are multiple fracture locations or fracture occurred outside of the primary loading zone, the fracture surface must be examined by either optical or electron microscopy methods for clarification.

In this analysis, scale diagrams of the bend bar layout were constructed and overlaid on top of the NDE maps for each group to determine if a correlation exists between the presence of an acoustic anomaly in the NDE maps and fracture location. Also included in these diagrams are marks indicating the fracture position for each layer of bars. Positions from the top layer are shown in black, positions from the middle

layer are shown in white, and positions from the bottom layer are shown in red. The primary loading zone of the bend test is also indicated in the diagrams by a black rectangle.

The assembled fracture overlay diagrams for the 6 tiles may be found in Figs. 5.21–5.26. Red regions are "high"-value regions while blue regions are scaled as "low"-value regions. When examining the fracture positions for each of the tiles, there does not appear to be a pattern in the primary fracture locations. In Fig. 21 there is a region of reduced attenuation coefficient toward the right side of the map that did not appear to have an effect on fracture location, as it was located outside of the primary loading zone of the flexure test. In Fig. 5.22 the values of longitudinal velocity increase when moving from the upper-left region to the lower-right region of the map. The gradient in the values did not appear to have an influence on fracture position. In Fig. 5.23 it can be seen that although the NDE tests have resulted in a consistent shear modulus map, there appears to be no discernible pattern to the location of fracture. Figures 5.24–5.26 contain fracture location diagrams overlaid on top of attenuation coefficient NDE maps. Again, there does not appear to be a pattern to fracture locations or a correlation between fracture location and NDE map features. Overall, it is challenging to make a definitive statement about the correlation between the position of the primary fracture location and any features found in the NDE maps.

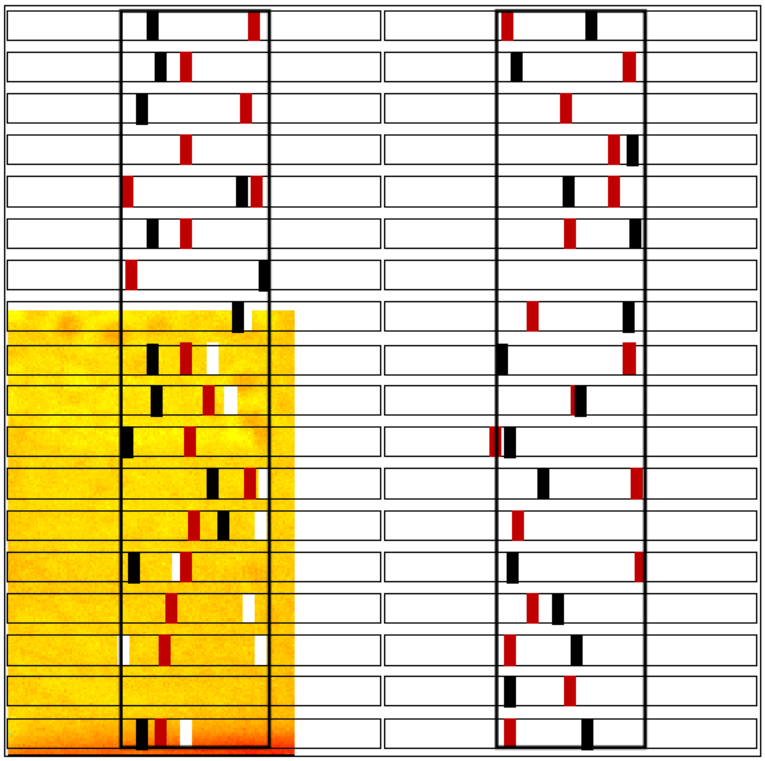

Fig. 5.84 Fracture location overlay, attenuation coefficient; Group 1, all layers

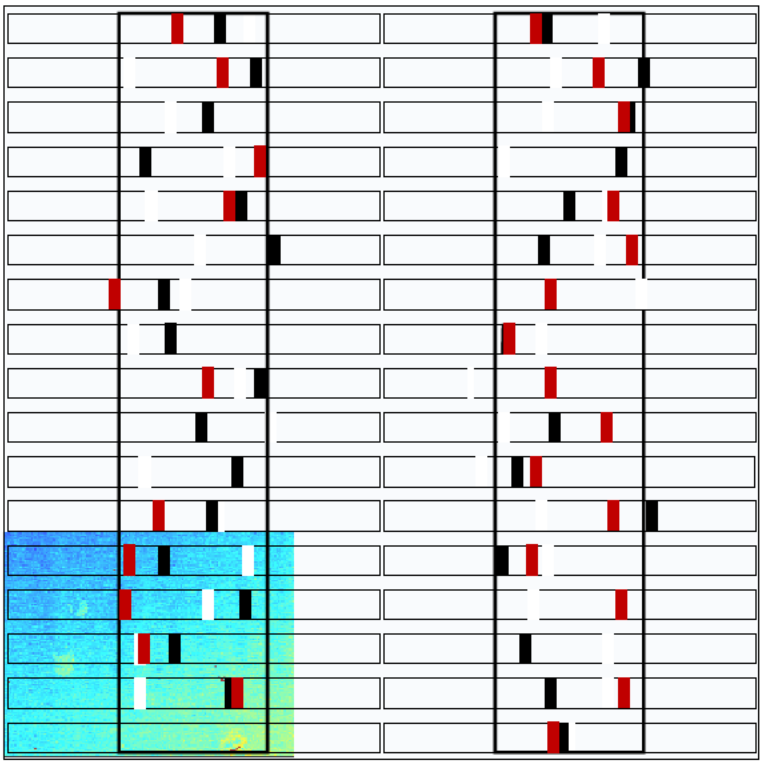

Fig. 5.85 Fracture location overlay, longitudinal velocity; Group 2, all layers

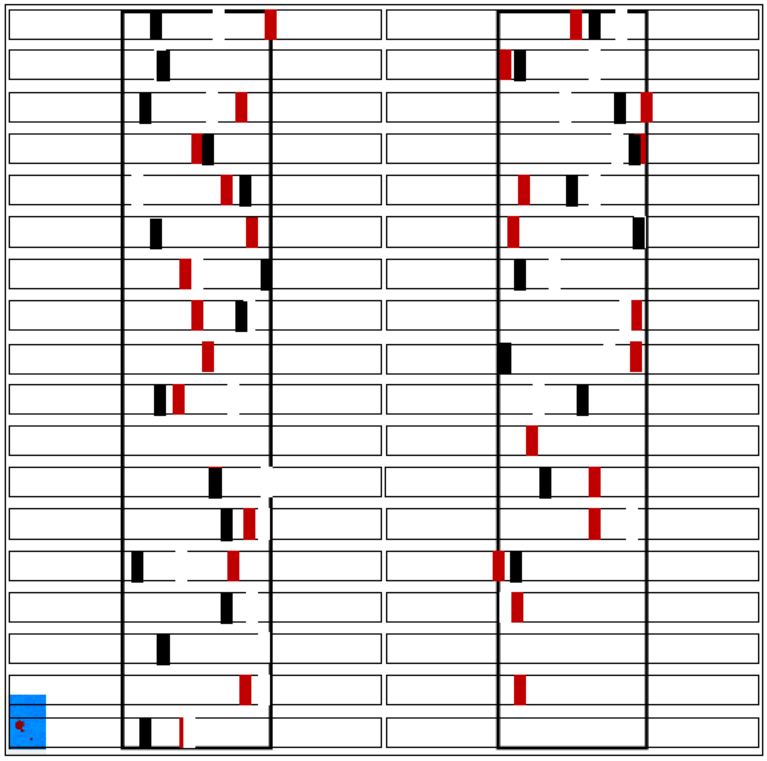

Fig. 5.86 Fracture location overlay, shear modulus; Group 3, all layers

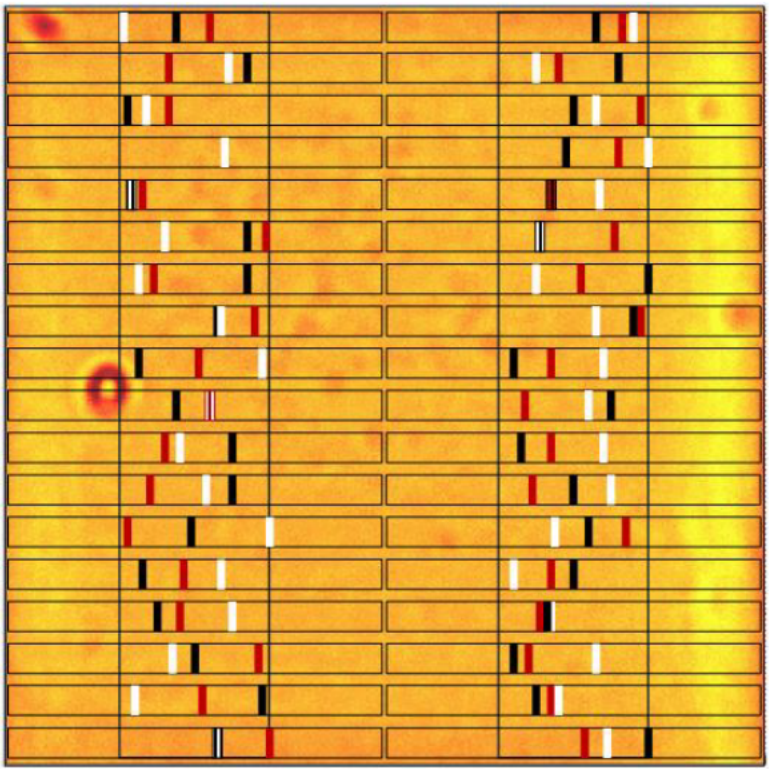

Fig. 5.87 Fracture location overlay, attenuation coefficient; Group 4, all layers

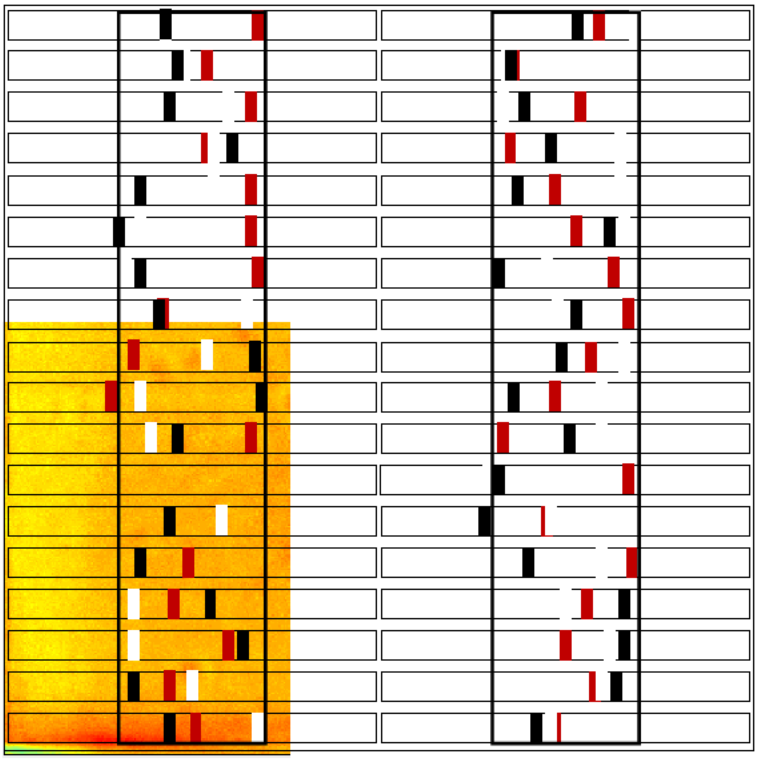

Fig. 5.88 Fracture location overlay, attenuation coefficient; Group 5, all layers

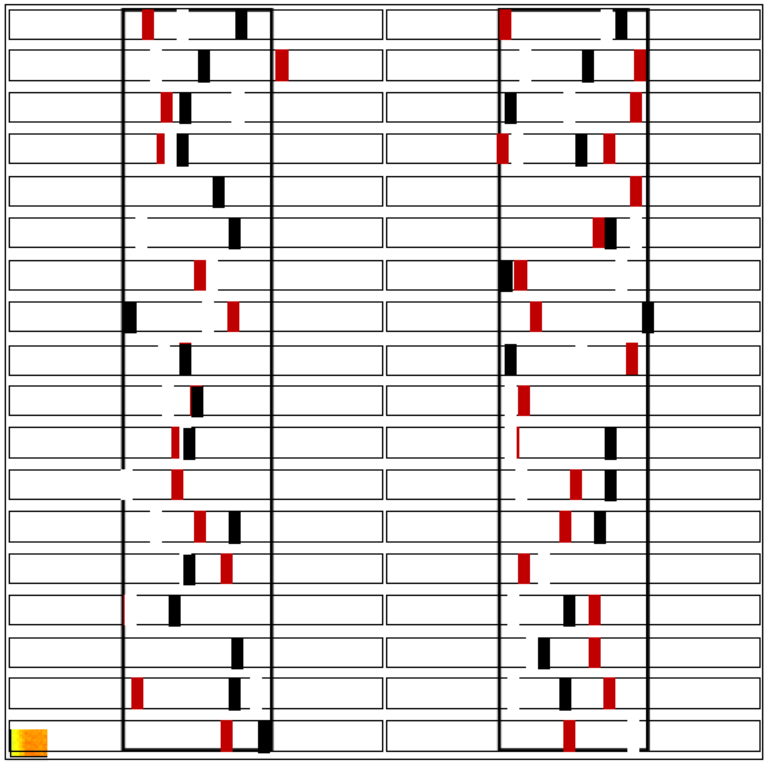

Fig. 5.89 Fracture location overlay, attenuation coefficient; Group 6, all layers

While the NDE maps are 2-dimensional, the tiles being examined are 3-dimensional. The value recorded at each scanning point contains the contributions of all Z values associated with that particular set of X,Y coordinates. Also included in the summation are contributions due to surface roughness. This can make it challenging to determine what the origin of an acoustic anomaly may have been. The 4 attenuation coefficient maps each contain acoustic anomalies. These are considered to be ring-shaped regions of increased attenuation coefficient that produce a "halo-like" affect around a center region.

At the time the original ultrasound work was completed, it was not possible to determine whether an acoustic anomaly was the result of a pit in the surface of the tile or from a feature within the bulk of the tile. A work-around for this has been employed in subsequent ultrasound evaluation testing, where an additional detection gate is defined for the region in the A-scan between the top surface and first bottom surface reflection peaks. If a feature with a high enough acoustic impedance mismatch, such as a large pore, is encountered by the ultrasound beam, it will produce a strong reflection. By determining the time of flight between the peak and the top or bottom surface reflections, it is possible to determine where in the depth of the sample the feature is located.

5.7 Fractography

Initial fractography work focused on the fracture surfaces of the bend bars to locate the fracture initiating feature. While this was done for many of the bars, work has progressed to also include features of interest on the fracture surfaces and within the microstructure of the material. In the next set of images, a series of low-strength bend bars will be discussed. The bars will be introduced in order of decreasing fracture strength.

Images that include the entire fracture surface of a bend bar are composite images. They are composed of 9–10 separate SEM micrographs that were recorded at 200× magnification in a raster pattern across the fracture surface. The images were then manually stitched together using image processing software. These composite images have proven to be very useful for analyzing overall fracture behavior by "mapping" the fracture surface for later analysis. Examples of these images are shown in Figs. 5.27–5.29. The tensile surface from the flexure tests has been indicated in the images as a frame of reference.

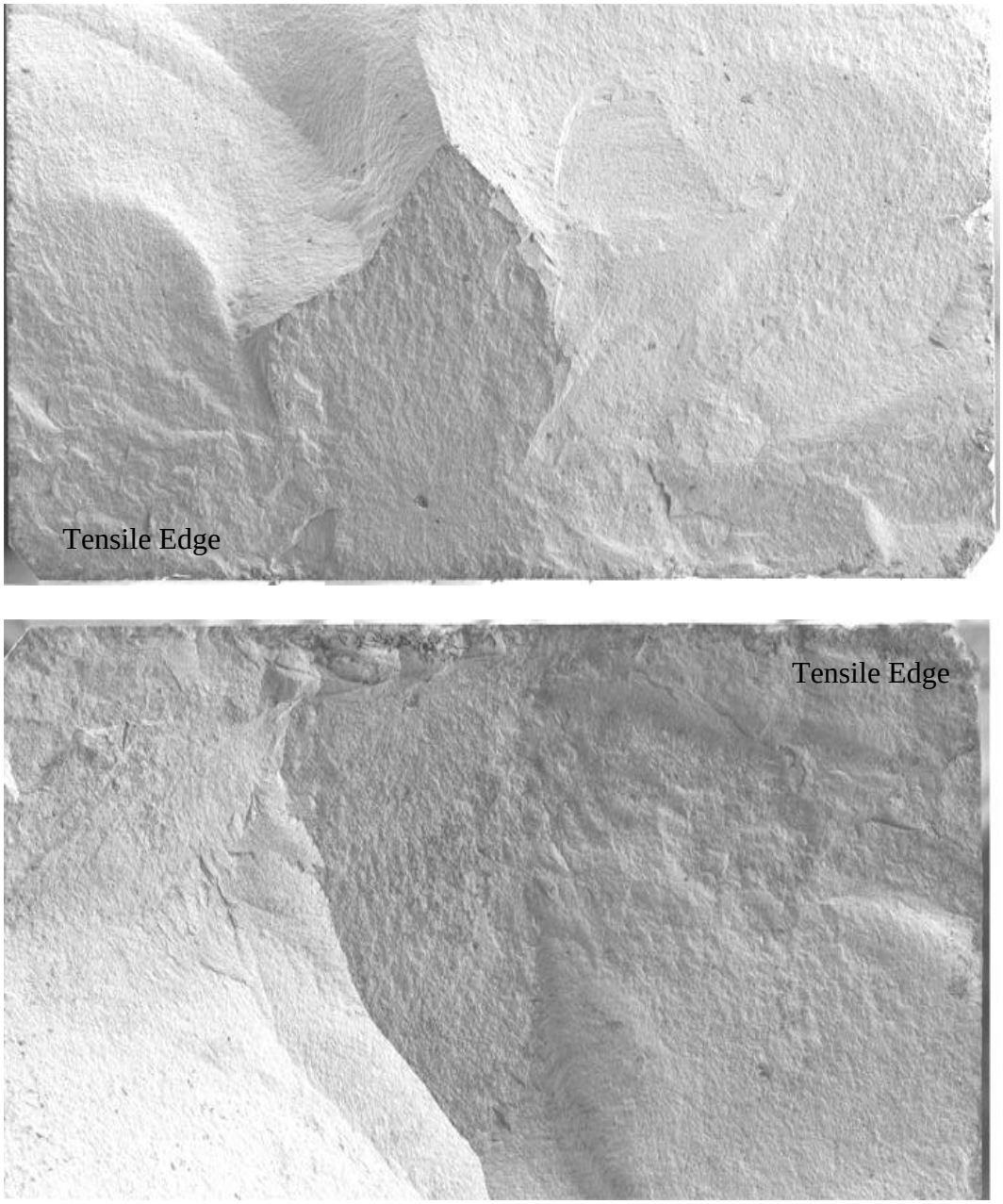

Fig. 5.90 Bar I, fracture surface end faces; composite image, 200× magnification

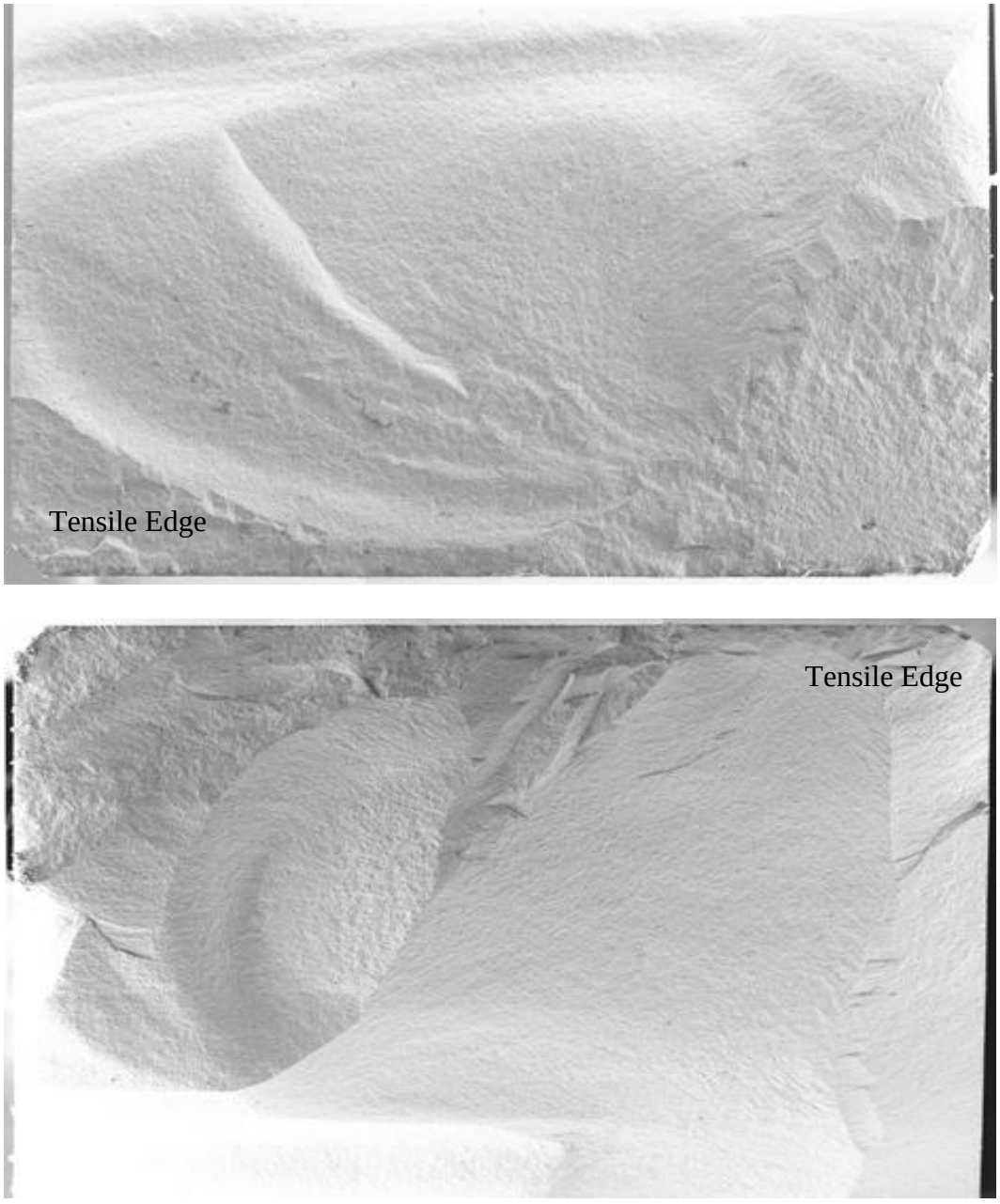

Fig. 5.91 Bar II, fracture surface end faces; composite image, 200× magnification

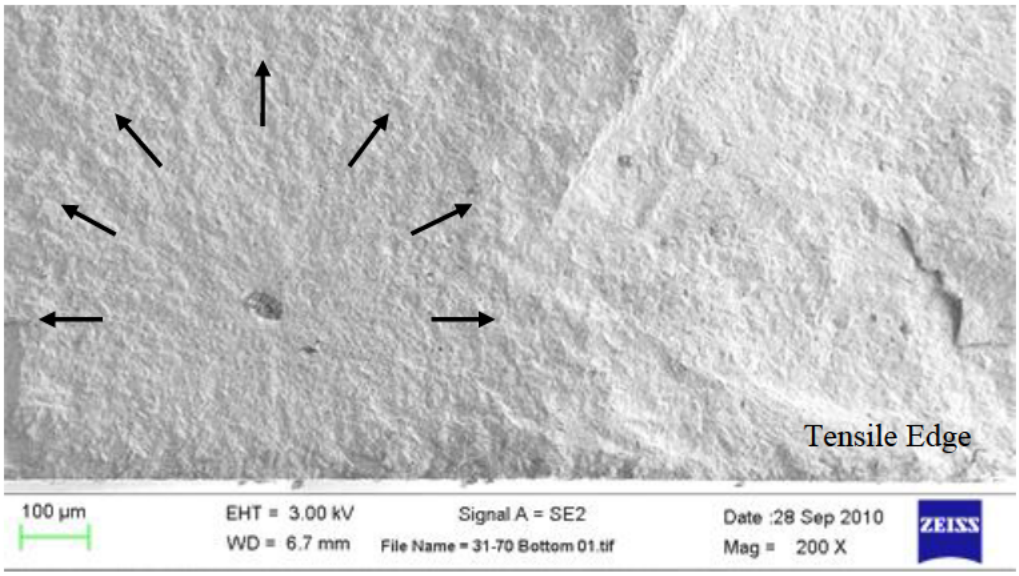

Fig. 5.92 Bar I, fracture path; 200× magnification

Figure 5.27 shows both the left and right end faces of the primary fracture surface of bar I, which was originally from the second row of the right-hand column in the middle layer of tile 31. This bar broke at a fracture stress of 383 MPa, placing it within the lower 15th percentile of strength values for this particular set of bars. Evidence of the primary fracture path and fracture initiating can be seen on both sides of the primary fracture position. This is not always the case, as secondary cracking during fracture can obliterate one or both of the sides of the primary fracture surface. It appears that fracture began near the center of the bar, close to the tensile surface.

The primary fracture surface of bar II is shown in Fig. 5.28. Bar II broke at an applied stress of 378 MPa, and was originally located in the 11th row of the right-hand column in the middle layer. Like bar I, this bar was also originally part of tile 31. In contrast to the previous example, remnants of the fracture path and what is believed to be the fracture initiating feature appear on only one side of the fracture surface. Based upon the texture of the fracture surface, it appears that fracture began in the lower-right corner of the cross section of the bar.

Images of the likely fracture-initiating features for these 2 bars are shown in Figs. 29 and 30. Arrows have been added to the images to indicate the likely path of fracture. In both cases, the fracture path appears to fan out from the feature in a relatively smooth pattern before altering direction as the stress field changed during fracture.

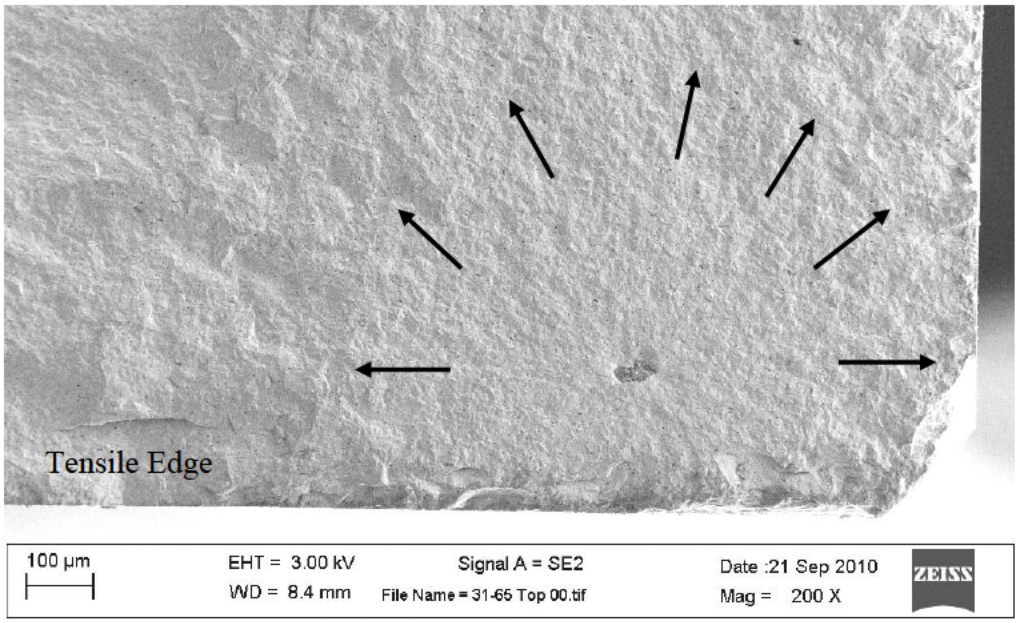

Fig. 5.93 Bar II, fracture path; 200× magnification

These features of interest can be seen in higher magnification in the next group of figures. Figure 5.31 shows images of what are believed to be the fractures initiating feature of bar I. Again, the results for this bar were quite interesting, as remnants of the likely fracture initiating feature appeared on both sides of the primary fracture surface. Dimpled and raised areas on a plate-like structure in the feature, as indicated by the arrows in the images, show a "mirror image" of themselves. This seems to indicate that this plate was split during fracture. Energy-dispersive X-ray spectroscopy (EDS) analysis was used to confirm that this feature was a B_4C inclusion; B_4C is added during the mixing process to act as a sintering aid.[12] Adding an excess of these materials or not ensuring proper mixing can result in unreacted material that forms agglomerates in the finished piece. These agglomerates can act as stress concentrators due to the elastic property mismatch with the SiC matrix.[13]

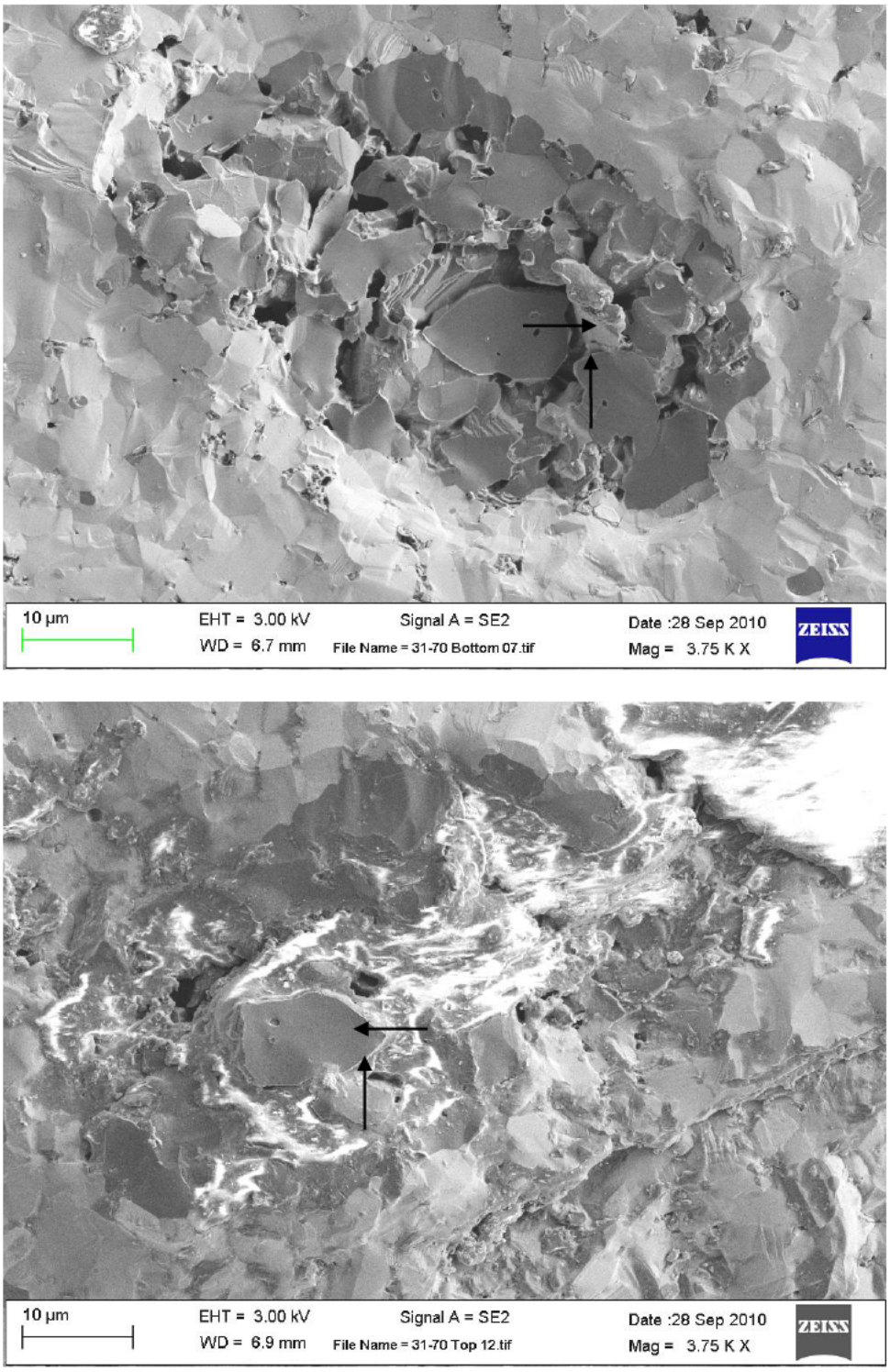

Fig. 5.94 Bar I, B_4C inclusion; 3,750× magnification

The major and minor axes of this inclusion were measured at 58.5 and 34.1 μm, respectively, while it was found that the minimum distance to the tensile surface was 235 μm. By taking these factors into account, along with the height of the bend bar, it is possible to estimate the stress applied to the feature in the instant before fracture initiated. This is done by taking a ratio of the stress at the tensile edge of the bar to the stress at the location of the feature. For this sample, this stress was estimated to be 323 MPa.

Figures 5.32 and 5.33 show higher magnification micrographs of the likely fracture initiating feature of bar II. EDS was used to confirm that this feature was also a B_4C inclusion. The major and minor axes of the visible portion of the inclusion were measured at 65.7 and 29.7 μm, respectively. By measuring the nearest distance of the inclusion to the tensile surface of the bend bar at 194 μm, the stress at the feature was calculated to be 329 MPa.

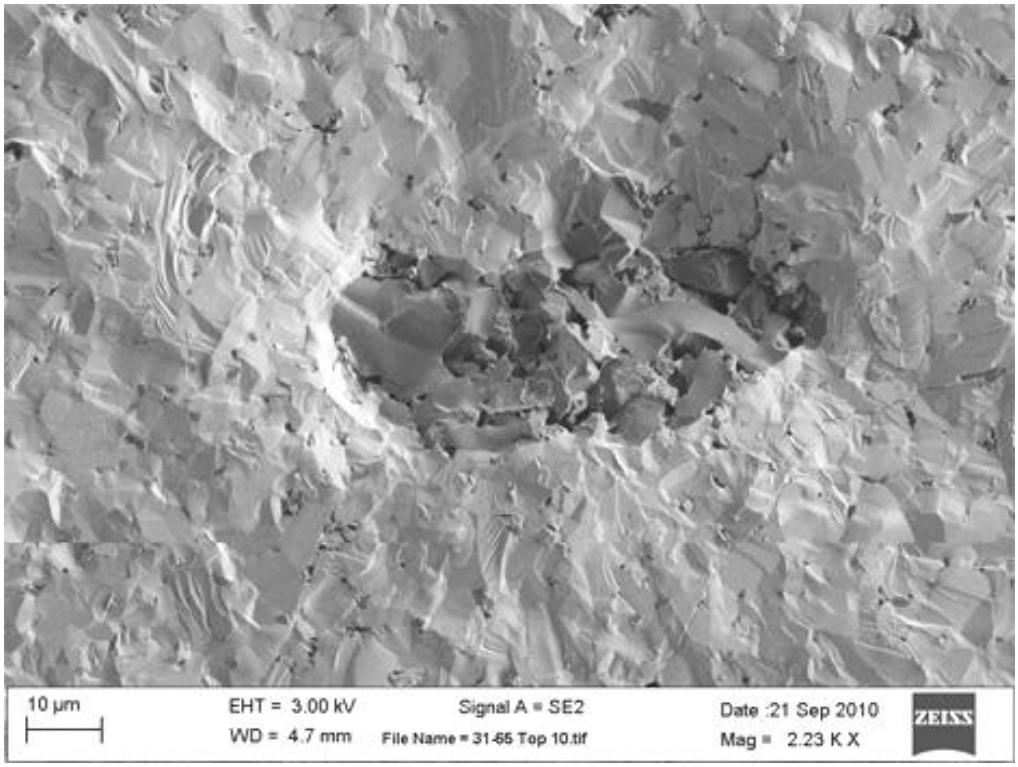

Fig. 5.95 Bar II, B_4C inclusion; 2,230× magnification

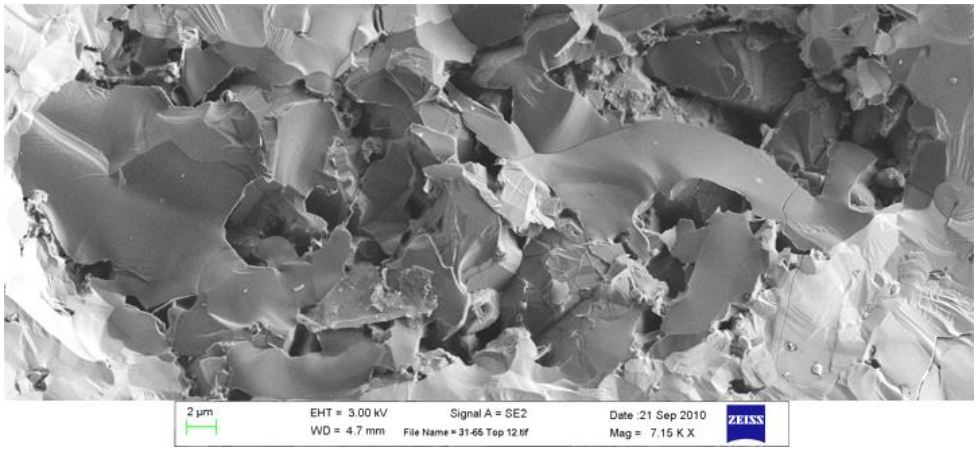

Fig. 5.96 Bar II, B_4C inclusion; 7,150× magnification

Figure 5.33 shows a composite SEM image of this B_4C inclusion recorded at 7,150× magnification. The inclusion appears to be very well integrated within the SiC matrix. The fracture path appears to radiate from the inclusion. It is interesting that this appears to be a complex, multigrained inclusion.

Beyond the determination of the fracture initiating feature, examining these images can give insight into fracture behavior and the presence and effect of microstructural features. Micron-sized C and B_4C inclusions have been observed on many of the fracture surfaces that have been investigated. These inclusions have also been imaged on polished sections of these bend bars. It is important to understand the effect that these features have on the fracture behavior of this material, both in the quasi-static and dynamic strain-rate regions. As part of the future work to be performed, the location and spatial position of these inclusions will be characterized.

After examining these images, it can be concluded that the primary mechanism of crack growth appears to be transgranular fracture. This same behavior was evidenced on all the other fracture surfaces of this material studied. Based on a study of the literature, this behavior likely comes about from a lack of an appreciable grain boundary phase. Materials with a significant grain boundary phase may experience a higher proportion of intergranular fracture, as the energy required to fracture the grain boundary is less than that required to fracture a grain. Lack of an appreciable grain boundary phase also makes this material somewhat easier to polish than other types of SiC as the amount of pullout from weakened grain boundaries is reduced.

The final bar that will be discussed is shown in Fig. 5.34. Originally located in the left column of the bottom layer of tile 11, this bar fractured at an applied stress of 200 MPa, the second-lowest strength in the entire study. The fracture surface is

characteristic of a low-strength fracture by displaying a very broad, relatively smooth fracture plane. As was the case with the bend bar that appears in Fig. 16, this bar broke due to errant machining scratches on the tensile surface of the bar. Even though the MOR value is no longer applicable to this study, there were many interesting features to be found on the fracture surface that warranted further discussion of this sample.

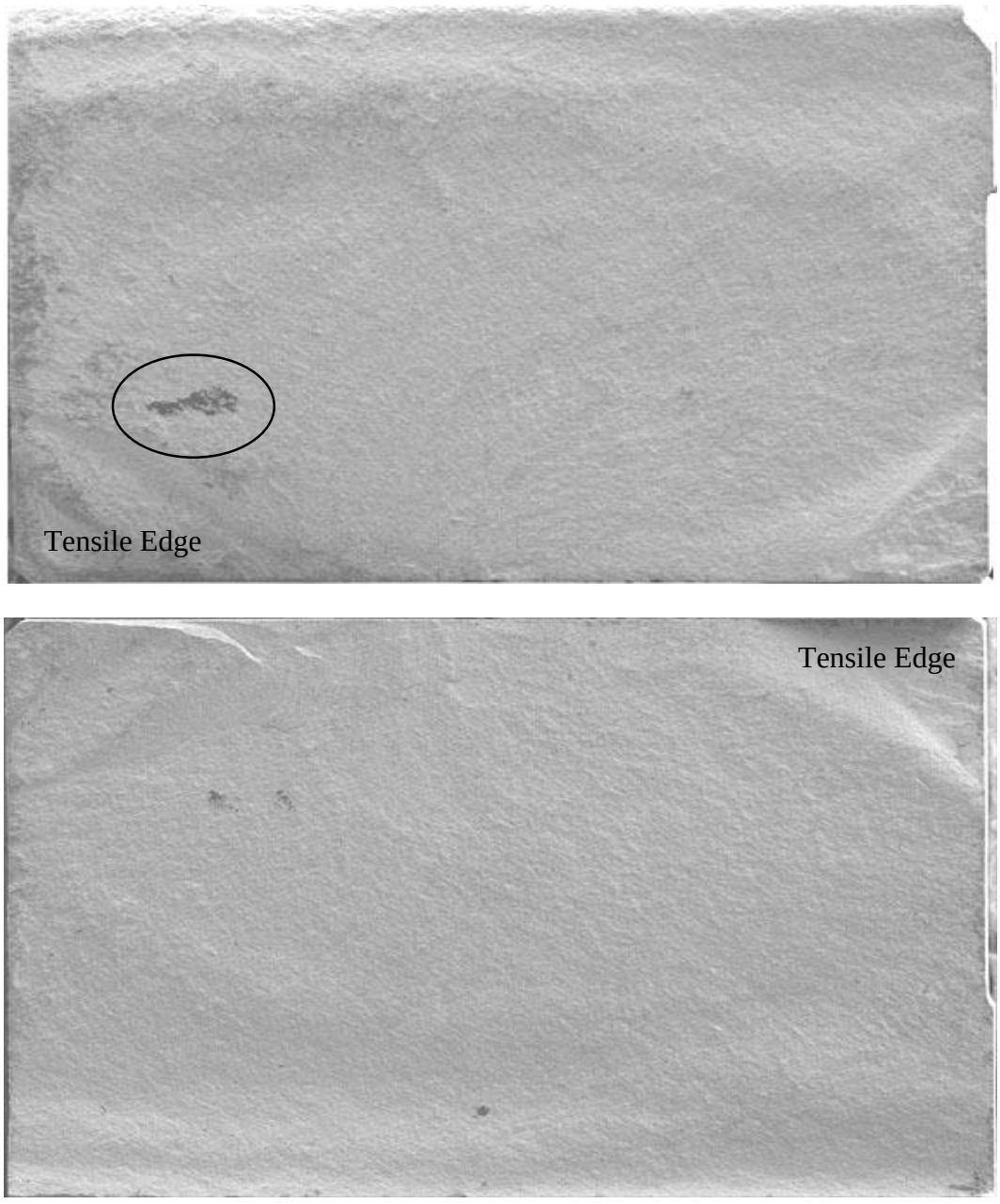

Fig. 5.97 Bar III, fracture surface end faces; composite image, 200× magnification

One of the more prominent features on the fracture surface has been indicated by a black ring, as shown in Fig. 5.34. Higher magnification views of this feature may be found in Figs. 5.35 and 5.36. What appears to be a dark, glass-like pool was characterized by EDS analysis to be C. This area has a very smooth surface and appears to be well integrated into the matrix of the bar. Surrounding this pool are a great many micron-sized Caceous inclusions. These "glassy" Caceous inclusions stretched in a vein from this large feature all the way to the tensile surface of the bar.

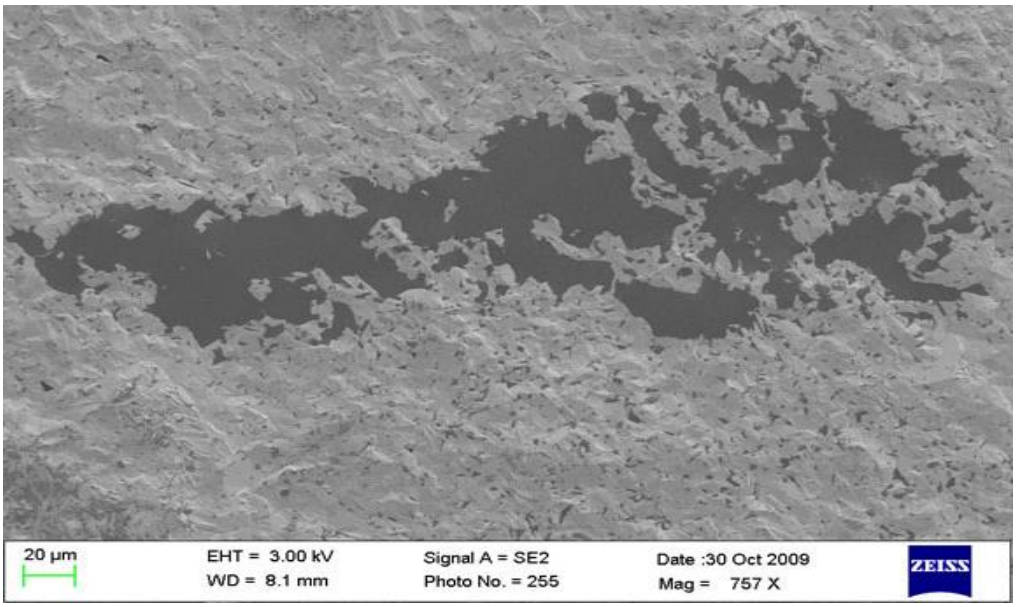

Fig. 5.98 Bar III, amorphous C region; 757× magnification

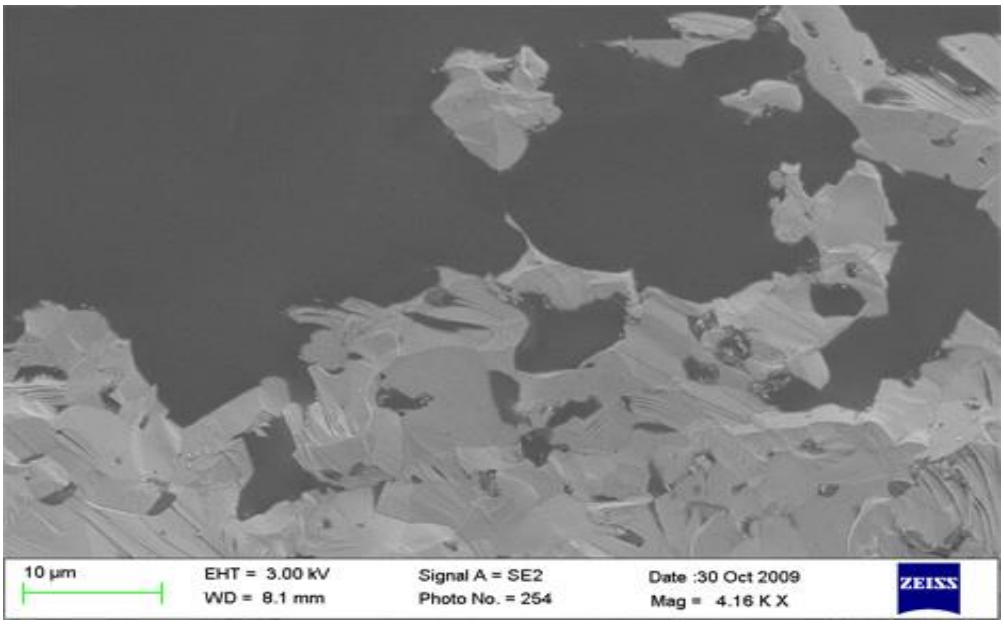

Fig. 5.99 Bar III, amorphous C region; 4,160× magnification

5.8 NDE Analysis

When the NDE data was examined qualitatively, it was found that it was difficult to determine if a correlation existed between features within the NDE maps and fracture location for the 3 layers of bars from within each tile. In follow-on analyses, a quantitative examination of the ultrasound data was made instead to look at variation within the NDE maps. Table 5.9 contains an expansion of the data found in Table 5.1. For the NDE measurements for each tile, the percentage of the standard deviation to the average value has been calculated. Values range between 0.09% and 3.9%.

Table 5.9 Ultrasound data with standard deviation as a percentage of average value

Tile No.	Type of Map	Unit	Average Value	Std. Dev.	Std. Dev. as a Percent of Average
8	Att. coefficient	dB/cm	2.31	0.09	3.9
11	Speed of sound	m/s	12,044	113	0.9
4	Shear modulus	GPa	182	3	1.6
31	Att. coefficient	dB/cm	2.15	0.05	2.3
2	Att. coefficient	dB/cm	2.21	0.07	3.2
19	Att. coefficient	dB/cm	2.17	0.05	2.3

Since these measurements were performed, a full characterization of the ultrasound test set has been performed. It was shown that the detectable variation in the attenuation coefficient measurement is 0.05 dB/cm.[5] This value was exceeded for only 2 of the tiles used in the MOR study.

As a comparison, the strength values from the different layers of each tile were looked at in the same way and can be found in Table 5.10. Tile 2 had the least amount of variation while tile 11 had the greatest. For all of the tiles, the variation in the strength data was much greater than the measured variation in the ultrasound data. One conclusion that may be drawn from this result is that the microstructural features that cause variations in the MOR values are not the same features that cause variation in attenuation coefficient, speed of sound, or elastic constant measurements, or that they cause a dissimilar degree of variation.

Table 5.10 MOR data with standard deviation as a percentage of average value

Tile Partition	Tile 8 (%)	Tile 11 (%)	Tile 4 (%)	Tile 31 (%)	Tile2 (%)	Tile 19 (%)
Top layer	10.4	14.2	14.0	10.4	10.1	11.4
Middle layer	12.9	19.7	11.5	12.3	6.6	11.7
Bottom layer	13.7	13.5	14.0	13.8	8.9	11.3
Entire tile	12.4	16.0	12.5	12.3	8.7	11.6

The quantitative NDE data was also examined using different methods. Using a program developed at Rutgers, it is possible to graphically manipulate and interpret the raw data from an ultrasound C-scan. A screenshot of this program, called Hermes, is shown in Fig. 5.37. Raw data is loaded into the program as a .txt file. As long as the data is present in the file, the user may select from multiple data sets to work with. The input boxes on the left are used to define the X,Y space for analysis as well as to set the scale in the image. By default, the program selects all of the data contained in the file, which, in the case of this study, is the full X and Y extents of a tile. Statistical information such as maximum and minimum value, the range, and the average value and standard deviation is displayed for the selected data.

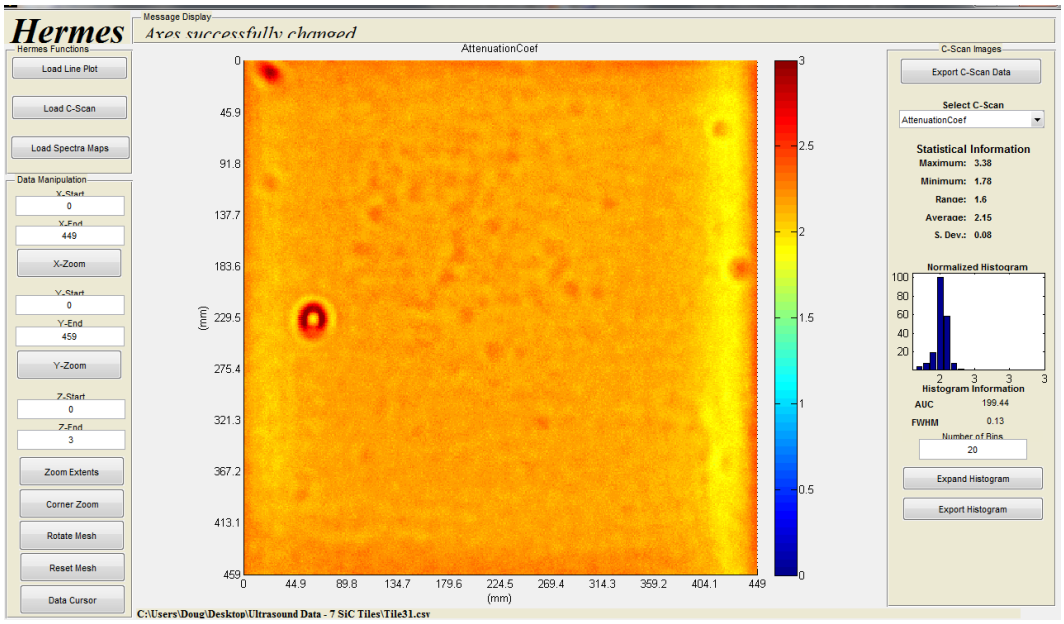

Fig. 5.100 Screenshot, Hermes NDE data analysis program

Using this program, the MOR/ultrasound data correlation was looked at in a different way. Hermes was used to determine the average value of an ultrasound produced measurement within the area of each bend bar position. This was done for all 108 bend bar positions from each tile. This data was compiled along with the MOR data and plotted, as shown in Figs. 5.38–5.43.

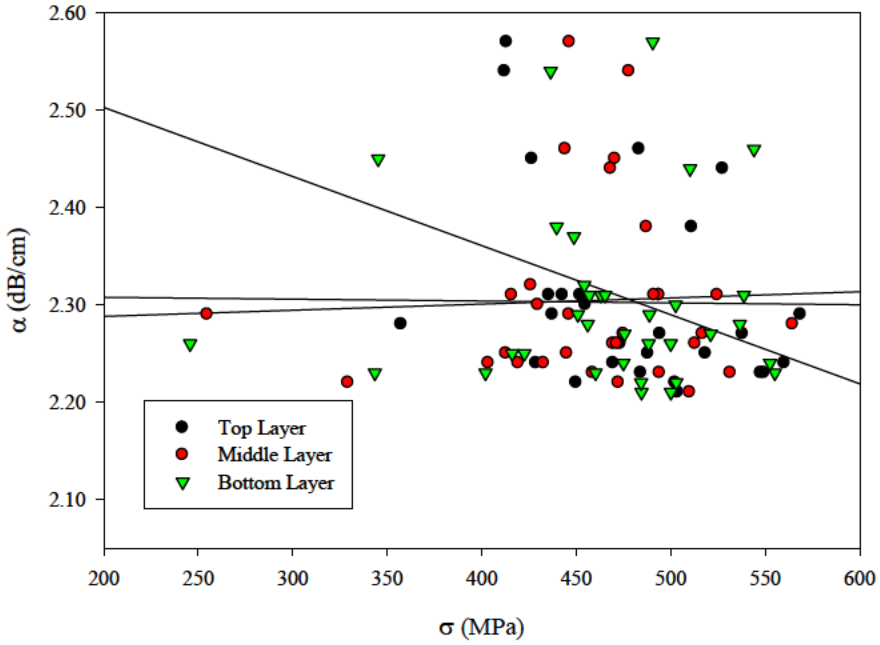

Fig. 5.101 Bend bar MOR vs. attenuation coefficient; Group 1, tile 8

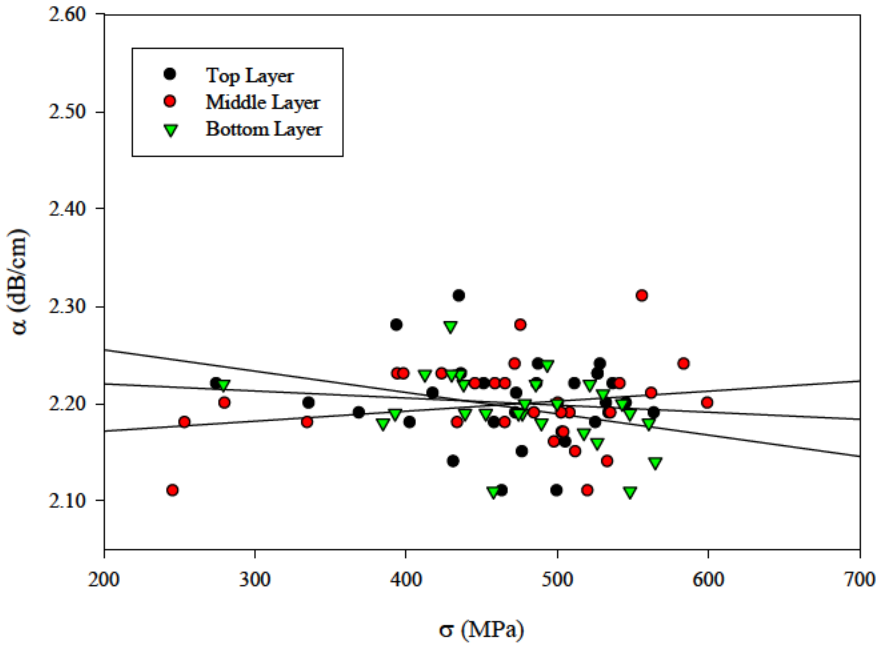

Fig. 5.102 Bend bar MOR vs. attenuation coefficient; Group 2, tile 11

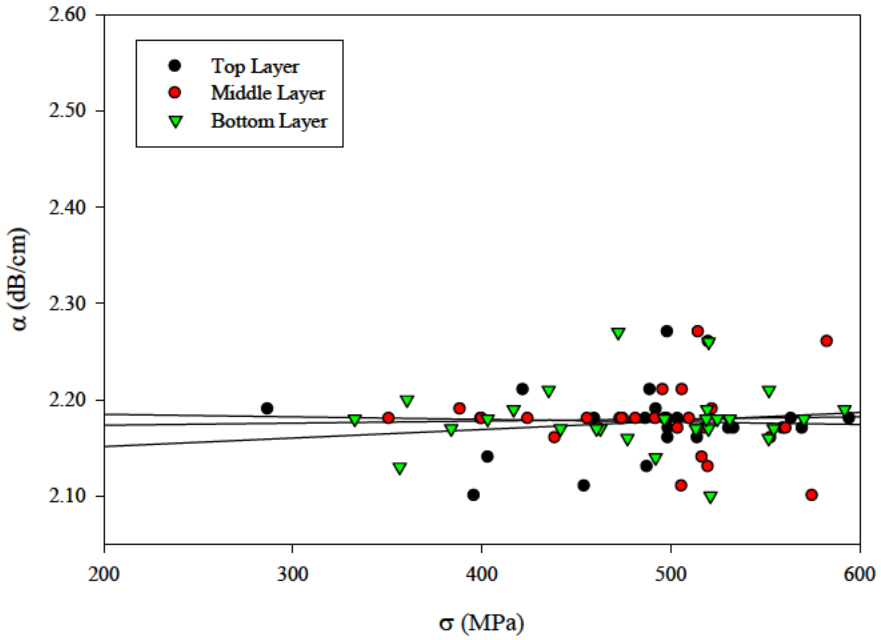

Fig. 5.103 Bend bar MOR vs. attenuation coefficient; Group 3, tile 4

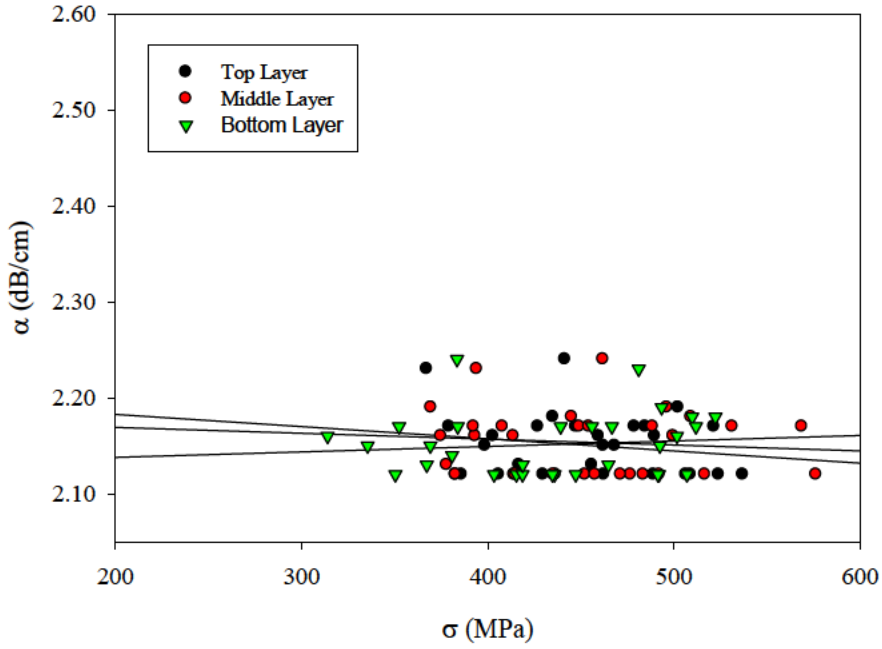

Fig. 5.104 Bend bar MOR vs. attenuation coefficient; Group 4, tile 31

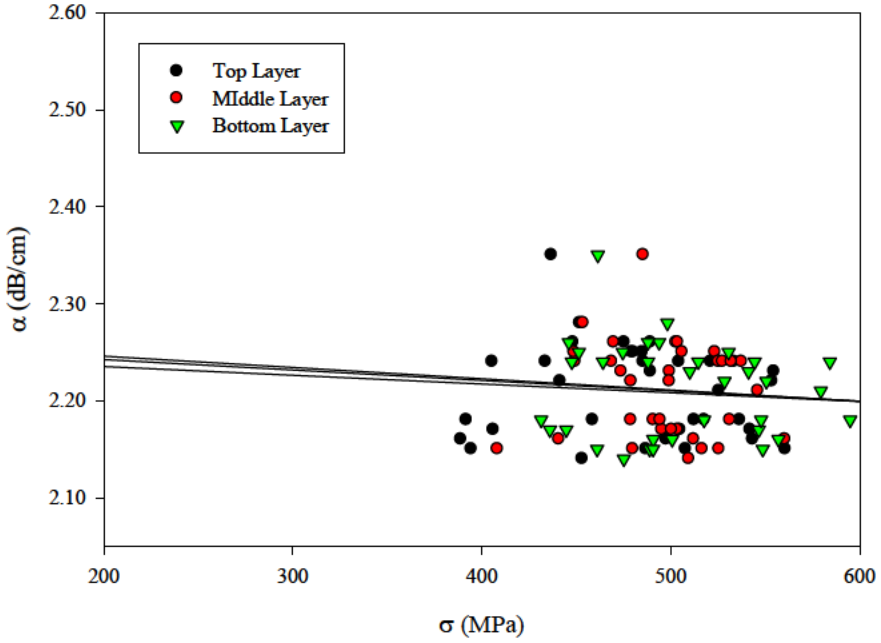

Fig. 5.105 Bend bar MOR vs. attenuation coefficient; Group 5, tile 2

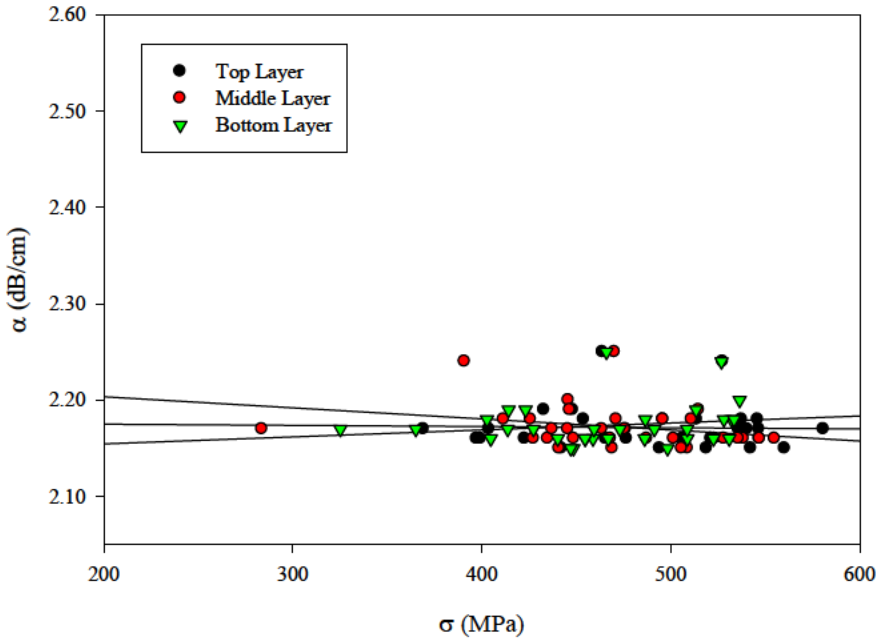

Fig. 5.106 Bend bar MOR vs. attenuation coefficient; Group 6, tile 19

Although the spread in the data was different for each group of bars, the X and Y axes were kept constant for a comparison to be made between the tiles. Within each tile group, the data has been displayed by layer. All 6 figures contain plots of average attenuation coefficient value versus MOR. Even though group breakdowns were made based upon different types of values, it was believed that it was more important to keep the plots consistent for comparison purposes. Linear regression lines have been included for the data from each layer to allow trends in the data to be more pronounced.

What is apparent when examining these figures is that there does not appear to be a pattern to the data. For 5 of the 6 tiles, the range in the Y-axis was less than 0.2 dB/cm. For the sixth tile, tile 8, bands of increased attenuation coefficient were located across the top and bottom of the tile corresponding to the upper-most left and right bend bar positions. If these 6 values are removed from the evaluation, the range in the data for this tile decreases to approximately 0.2 dB/cm. What appears to be clear is that there was not enough measured variation within these tile sets.

5.9 Targeted Samples

This study was performed on a lot of fully-dense, "good", commercial off-the-shelf tiles. It was carried out in the hope that there would be a measurable difference between the tile sets based upon the type of ultrasound scans that were performed. An alternative route would have been to manufacture or produce samples, based upon an understanding of the mechanisms involved in the interaction between the acoustic energy and the material, such that there would be a measurable difference amongst the samples.

Attenuation coefficient measurements are frequency-dependent measurements affected by the wavelength range of the ultrasound transducer along with the type and size of the microstructural feature and matrix material present in the sample. These features may include inclusions, pores, and matrix material grains. Speed of sound measurements are most highly affected by the density of the material being scanned.

5.1 Reduced Density Samples

One approach involves manufacturing SiC tiles that are produced with highly increased levels of porosity and therefore reduced density. These tiles were pressed to a lower green density and then pressurelessly sintered.

Five tiles have been produced. Three of the tiles measured 60 × 60 × 6 mm, while the other 2 tiles measured 60 × 60 × 3.5 mm. Archimedes density values of the 5 tiles can be seen in Table 5.11. The average value of the 5 tiles was 3.08 g/cm^3. The average density value for the original 41 Hexoloy tiles was 3.17 g/cm^3.

Table 5.11 Archimedes density values for reduced density targeted samples

Bulk Density (g/cm^3)	Tile 1	Tile 2	Tile 3	Tile 4	Tile 5
	3.08	3.09	3.09	3.05	3.07

Ultrasound C-scan results for these 5 tiles can be seen in Figs. 5.44–5.48. Attenuation coefficient measurements were recorded using an Olympus 20-MHz planar unfocused transducer. Figures 5.44–5.48 show the resultant C-scan maps. The results show increased levels of acoustic attenuation compared with the original 6 Hexoloy tiles that were chosen for machining into bend bars. The average attenuation value across the area of the tile was measured at 3.28 dB/cm for the 5 tiles. This represents almost a 50% increase in attenuation coefficient at 20 MHz compared with the original 6 tiles. Selected samples have been machined into ASTM B-type flexure bars.

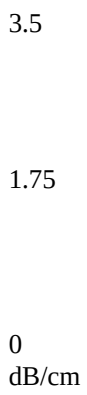

20MHz Attenuation Coefficient NDE Map

Fig. 5.107 Low-density SiC targeted samples, tile 1

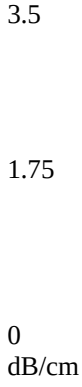

20MHz Attenuation Coefficient NDE Map

Fig. 5.108 Low-density SiC targeted samples, tile 2

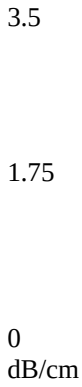

20MHz Attenuation Coefficient NDE Map

Fig. 5.109 Low-density SiC targeted samples, tile 3

3.5

1.75

0
dB/cm

20MHz Attenuation Coefficient NDE Map

Fig. 5.110 Low-density SiC targeted samples, tile 4

3.5

1.75

0
dB/cm

20MHz Attenuation Coefficient NDE Map

Fig. 5.111 Low-density SiC targeted samples, tile 5

Three bars were chosen for machining into flexure bars. As with the commercial tiles, the ASTM B-type bar was chosen to allow for comparisons with the previous samples. The machining configuration for these tiles is shown in Fig. 5.49, which depicts the actual size of the tile and flexure bars. The 4-mm dimension of the bars was machined to be parallel to the 6-mm dimension of the tile in contrast to the commercial tiles, where the 4-mm dimension was parallel to the 101.5- × 101.5-mm plane of the tile. This was done to allocate for the minimum separation of 1-mm between the bars because of the small size of the reduced-density tiles. Bars were labeled 1–10 starting at the top of the tile.

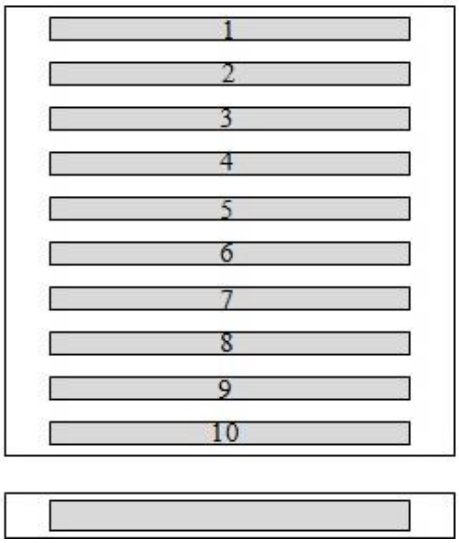

Fig. 5.112 Flexure bar machining diagram of reduced density SiC tile: one layer of bars, 10 bars per tile. Three tiles underwent machining; 3-mm dimension of bar parallel to 60- × 60-mm plane of tile.

All 30 bars survived the machining operation. Testing was carried out in accordance of the procedures in ASTM Standard C1161. The results of the flexure testing are shown in Table 5.12. The average value and standard deviation have been calculated for the 10 bars from each tile.

Table 5.12 Flexure testing results for reduced-density SiC tiles; mean value of 317 MPa

Tile No.	Average (MPa)	Std. Dev. (MPa)	*m*
Tile 1	306	17	. . .
Tile 2	324	18	. . .
Tile 3	322	18	. . .
3 tiles	317	19	20.4

The average strength value of all of the tested samples was found to be 317 MPa with a standard deviation of 19 MPa. This represented a deviation of only 6%. The range of values was 280–360 MPa. In addition, the Weibull modulus was determined to be 20.4. Weibull parameters were not calculated for the individual tiles as the calculation of a Weibull modulus requires a minimum of 30 values.[72]

The Weibull plot for the reduced density SiC flexure bars is shown in Fig. 5.50. The distribution of strength values is quite tight, as the Weibull modulus is almost twice that attributed to the commercial SiC tiles. Although there appear to be outliers at the top and bottom ends of the Weibull plot, all fractures were attributed to the same type of critical feature.

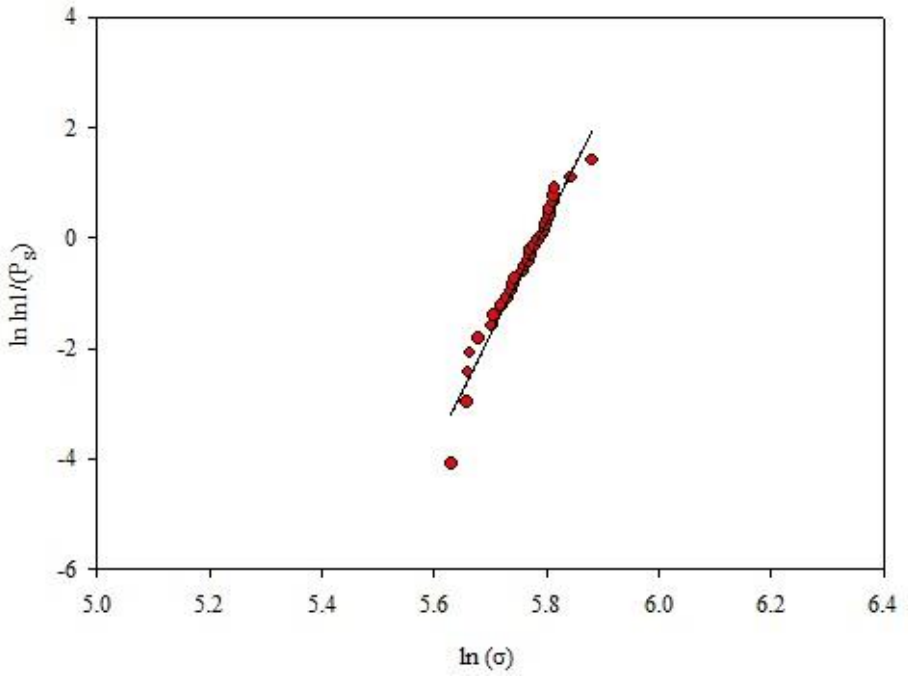

Fig. 5.113 Weibull plot of reduced-density SiC tiles, 30 bars

The fracture of all 30 bend bars was attributed to the presence of spray-dried relics that were not completely reacted, which resulted in porous regions within the microstructure of the material. Three examples will be discussed in order of increasing fracture strength. Fracture strengths have been divided into 3 regions, as shown in Table 5.13. Region A is comprised of the 5 lowest strength bars, while Region C contains the 2 highest strength bars. The balance of the bars has been grouped into Region B. Compared with the flexure bars from the commercial SiC tiles, these would be considered to be low- and low-to-medium-strength bars.

Table 5.13 Strength regions of flexure bars from reduced-density SiC tiles

$\sigma_f < 300$	Region A
$300 \leq \sigma_f < 345$	Region B
$345 \leq \sigma_f < 360$	Region C

Composite FESEM images of the primary fracture surface of bar I are shown in Fig. 5.51. Bar I broke at a strength of 287 MPa, which placed it within Region A. This was considered to be a type A fracture, with a cantilever curl (noticeable in the bottom image) and horizontal crack branching. Arrows in the images point to where fracture is believed to have initiated, while a rectangular box has been placed around the region which is thought to contain the critical feature.

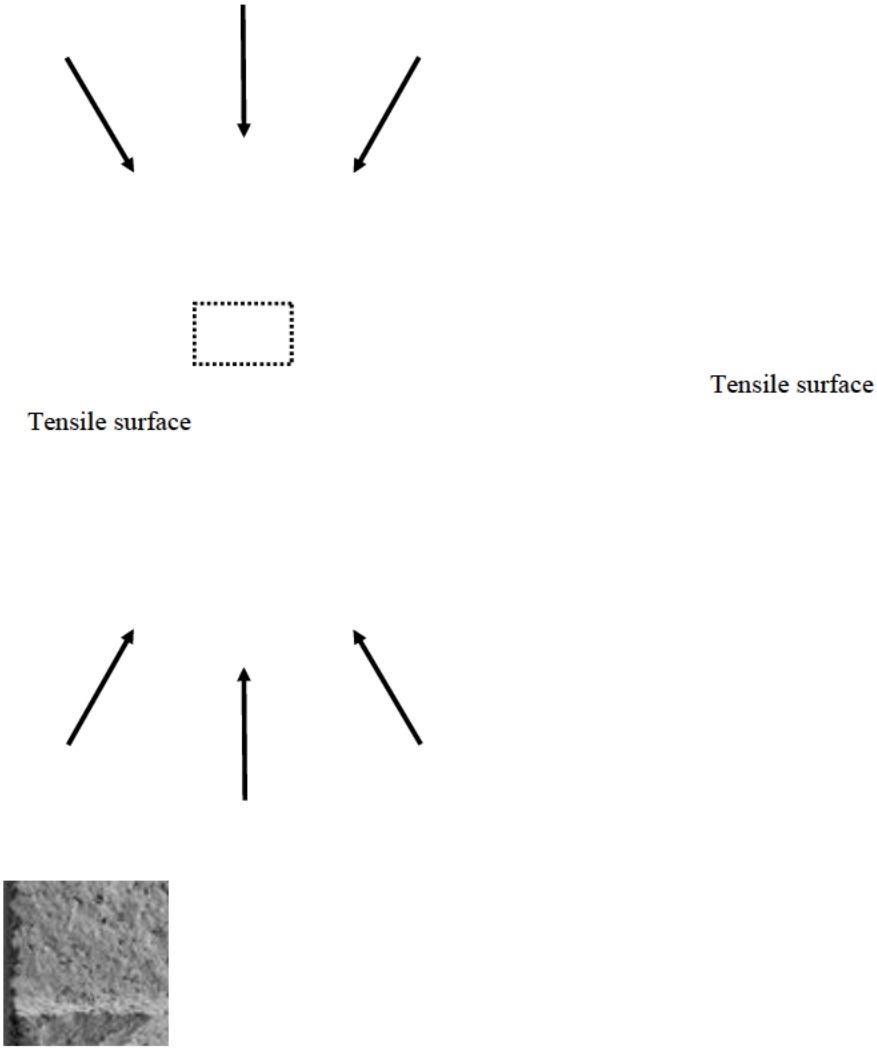

Fig. 5.114 Bar I primary fracture surface, left and right end faces, reduced-density flexure bar (σ_f = 287 MPa), region A, composite images, 200× magnification. Fracture appears to have initiated toward the left side of the bar.

Two images from this region are shown in Fig. 5.52. The upper image, recorded at 200×, approximately corresponds to the area within the rectangle in Fig. 5.51. Arrows have been added to the image to indicate the fracture path.

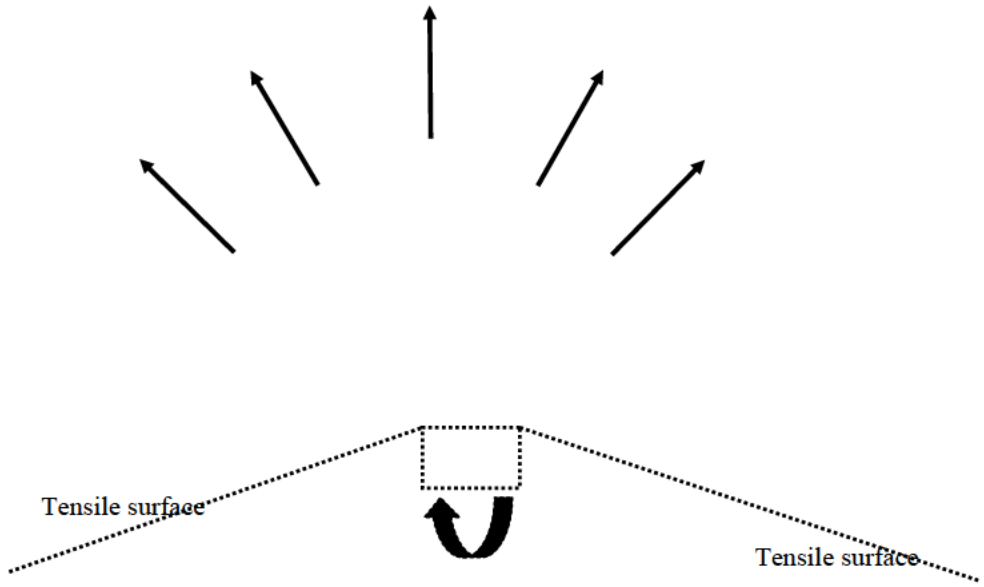

Fig. 5.115 Bar I fracture surface, reduced-density flexure bar (σ_f = 287 MPa), 200× magnification (top), 2,850× magnification (bottom). Fracture appears to have originated from the location of an unreacted spray-dried granule.

The bottom image in Fig. 5.52 contains a higher magnification (2,850×) FESEM micrograph of what is believed to be the fracture-initiating feature of this flexure bar. This orientation of this image has been rotated 180° in relation to the top image. The dominating feature in the image is believed to be a spray-dried granule.

As mentioned previously, granulation refers to the process of intentionally agglomerating fine powders into larger clusters. This granule was quite large, as the portion of it that can be seen measured over 55 μm in width and height, and is located very near to the tensile surface. The remnants of 2 smaller granules can also be seen in the image. One of these, located near the top left of the large granule, appears to still be relatively spherical. The other, located at the left of the middle of the large granule, appears to be almost completely reacted.

An image of the fracture surface on the portion of the bend bar opposite to that in Fig. 5.52 is shown in Fig. 5.53. A black circle has been placed in the image which corresponds to the location of the visible portion of the large spray dried granule. A number of voids which occur at the interaction of granules can be seen in this area.

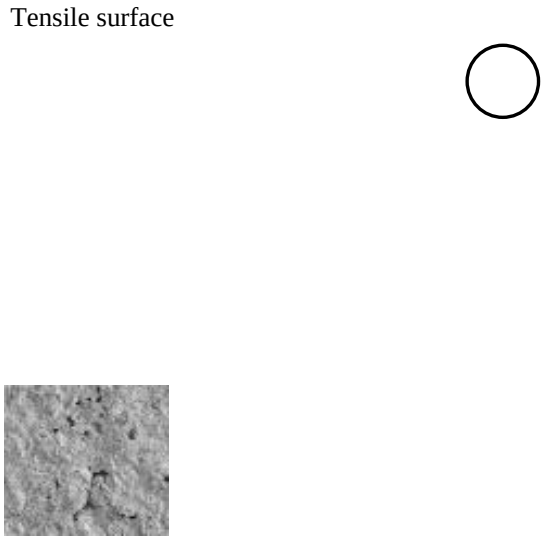

Fig. 5.116 Bar I fracture surface, reduced-density flexure bar (σ_f = 287 MPa), 200× magnification. Image of the opposite side of the primary fracture surface. Circle marks the location of the spray-dried granule seen in Fig. 6.52.

A higher magnification image of the large spray dried granule is shown in Fig. 5.54. Present in the image are what appear to be 2 tetrahedra on the surface of the large granule located near the partially reacted small granule, as indicated by the circles in the image. These corresponded to symmetrical stacking of individual SiC_4 tetrahedra.

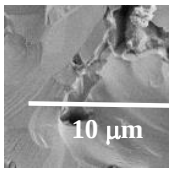

Fig. 5.117 Bar I reduced-density flexure bar (σ_f = 287 MPa), 3,680× magnification, large spray-dried granule

5.11 Increased Boron (B) Content Samples

A second approach to producing targeted samples relied upon manufacturing tiles containing an excess of B_4C sintering additives. Levels of B_4C added were between 0.3% and 0.6% in commercially available SiC. These tiles have been produced with 3.0% B_4C additives. The extra amount of B_4C comes from adding the collected "fines" from a B_4C spray-dry run. These fines were added to the powder batch. The tiles were pressed to a routing green density for commercially available SiC and then nonpressure sintered. The intention with this approach is to examine the effect of enhanced B_4C content on the mechanical and acoustic response of these samples.

Five tiles were produced by this method. The appearance of the tiles is consistent with other commercially available SiC plates. The fired density of all 5 plates was measured by immersion to be 3.14 g/cm^3. In Figs. 5.55–5.59 are 20-MHz attenuation coefficient maps of these samples, the average of which was 8.6 dB/cm. This is almost 4 times the average value for the original 6 Hexoloy commercial tiles selected for machining into flexure bars. One of the motivations

for doing this work is to determine the microstructural features that give rise to the increased acoustic attenuation. Selected samples have been sent out for machining into mechanical testing samples.

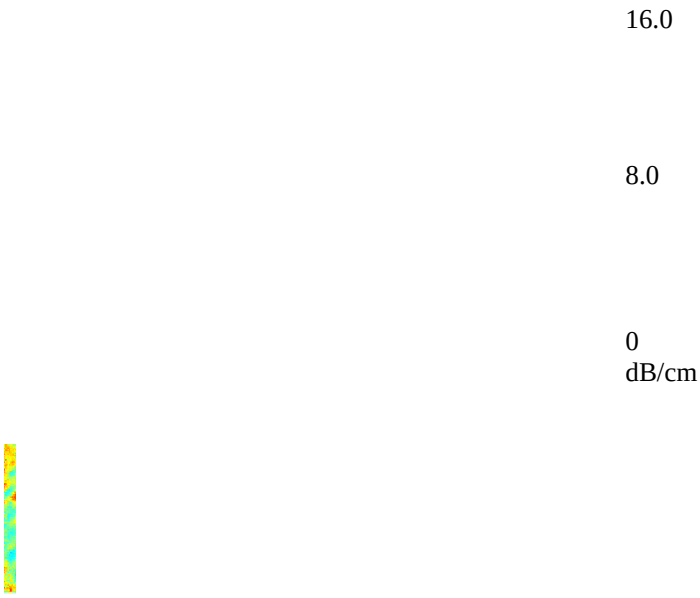

20MHz Attenuation Coefficient NDE Map

Fig. 5.118 Increased B-content SiC targeted samples, tile 1

20MHz Attenuation Coefficient NDE Map

Fig. 5.119 Increased B-content SiC targeted samples, tile 2

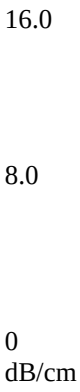

20MHz Attenuation Coefficient NDE Map

Fig. 5.120 Increased B-content SiC targeted samples, tile 3

.

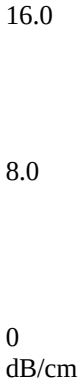

20MHz Attenuation Coefficient NDE Map

Fig. 5.121 Increased B-content SiC targeted samples, tile 4

16.0

8.0

0
dB/cm

20MHz Attenuation Coefficient NDE Map

Fig. 5.122 Increased B-content SiC targeted samples, tile 5

Archimedes density measurements were carried out on the 3 enhanced-B- content SiC tiles. The mean value for the 2 tiles was 3.14 g/cm^3. This represented a decrease in density of less than 1% when compared with the commercial SiC tiles.

Two tiles were chosen for machining into ASTM B-type flexure bars. The bend bar machining diagram for these tiles is shown in Fig. 5.60. The diagram depicts the actual size of the tiles and flexure bars. Fifteen bars were machined from each of 2 tiles for a total of 30 bars. In contrast to the commercial and reduced-density tiles, the long axis of the bars were oriented up and down as opposed to left and right in relation to the starting tile. This was done so the bar positions would coincide with the regions of the tile where the acoustic anomalies were located. Bars were numbered 1–15 starting at the left side of the tile.

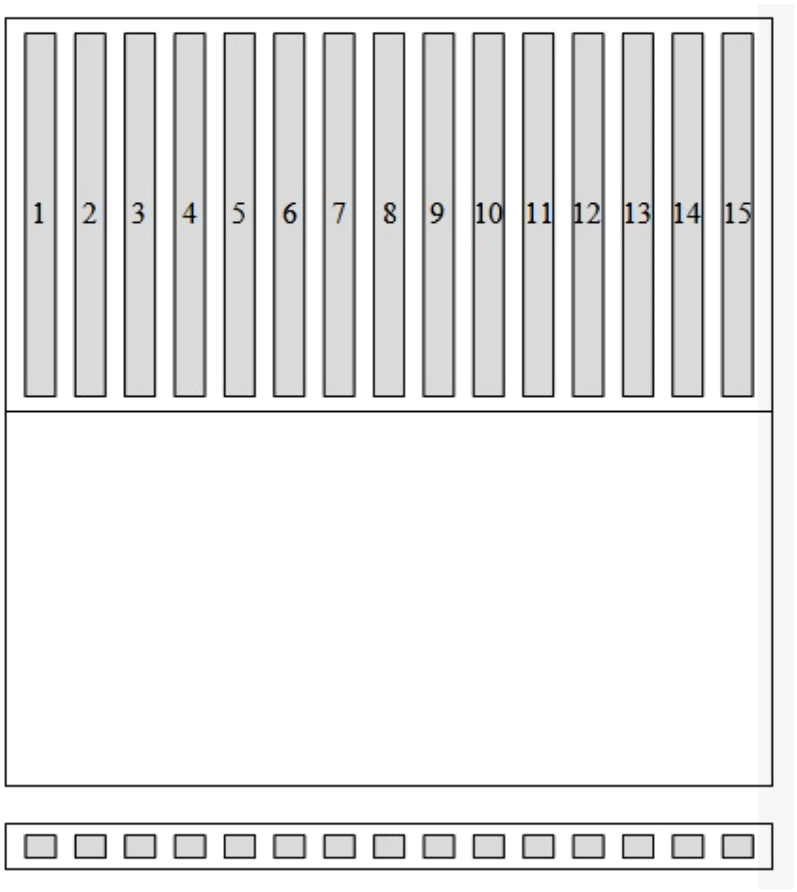

Fig. 5.123 Flexure bar machining diagram of enhanced-B-content SiC tile. One layer of bars, 15 bars per tile, 2 tiles machined, 4-mm dimension of bar parallel to 100- × 100-mm plane of tile. Lower portion of each tile returned from machinist for further evaluation (if needed).

All 30 bars were returned from the machinist. Testing was performed in accordance with the procedures set forth in ASTM Standard C1161. One bar was broken without result during the flexure testing.

The Weibull plot that corresponds to the strength testing results of the environmental-barrier-coating flexure bars is shown in Fig. 5.61. There appear to be 3 regions of strength values within the results. These have been designated I, II, and III. Overall, fracture strength varied between 86 and 175 MPa. The fracture behavior of all bars was considered to be type A fractures. The strength statistics and Weibull modulus will be presented after the examination of strength limiting features.

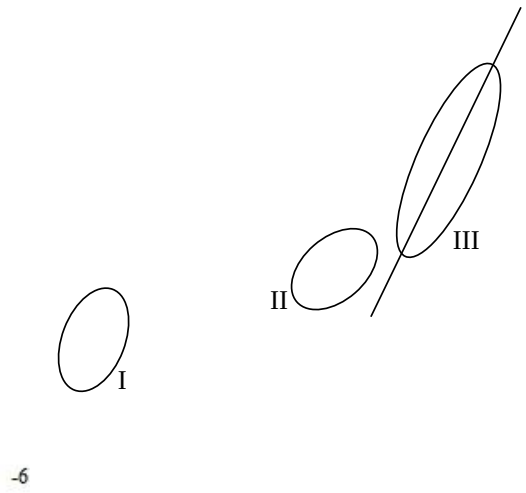

Fig. 5.124 Weibull plot, enhanced-B-content tiles, 29 bars

The composite images of the primary fracture position of bar M are shown in Fig. 5.62. This was a below-average-strength enhanced-B-content flexure bar (σ_f = 130 MPa) that was categorized within region II. As with the previous example, the fracture plane appears to be almost completely vertical, without horizontal crack branching.

Tensile surface

Tensile surface

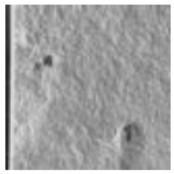

Fig. 5.125 Bar M primary fracture surface, left and right end faces, enhanced-B-content flexure bar (σ_f = 130 MPa), region II, below-average-strength bar, composite images, 200× magnification

Increased magnification images of the likely fracture-initiating feature are shown in Fig. 5.63. These appear to be a cluster of interconnected B_4C inclusions. While fractures of the flexure bars from region I were attributed to large masses of porous B_4C, these types of features where considered to be separate inclusions that were located in close proximity to one another. The largest of these inclusions measures approximately 400 μm in length.

Tensile surface

Tensile surface

Fig. 5.126 Bar M fracture surface, enhanced-B-content flexure bar (σ_f =130 MPa), region II, cluster of connected B_4C inclusions, 500× magnification

In the images corresponding to this example, it is possible to discern the oval-like shape of the individual B_4C inclusions, which are similar in appearance to the examples provided in previous sections. However, the cross sections of the porous B_4C inclusions that were found in the commercial samples were between one-half to one-quarter the size of the inclusions found here. It appears that a dome-shaped section of the fracture surface broke away from the bottom of the largest inclusion. This section contained portions of the multiple inclusions in the cluster.

5.12 Summary

Multiple sample sets of sintered SiC tiles were examined to determine the extent of microstructural and acoustic and mechanical property variability. These included both commercially available SiC tiles as well as specially prepared sample sets. A number of analysis tools were employed to examine the variability of these properties within each sample set and between each sample set.

The correlation between mechanical and acoustic properties was examined for all 3 sample sets. In the analysis of the commercial samples, it was found that ultrasound C-scans performed at 20 MHz were unable to detect local-scale differences, on the scale of a fracture-inducing defect, in acoustic properties in sintered SiC materials. There was much greater variability in the strength results than what was detected in the acoustic testing within each tile.

Ultrasonic testing showed that there were differences between the measured values between the different sample sets. The least squares regression analysis of the 20-MHz attenuation coefficient and average strength value returned a correlation coefficient of $R^2 = 0.86$. It can be concluded that while localized differences in strength or microstructure are not manifested in the ultrasound measurements, bulk changes in the microstructure are resolved in the average value of the 20-MHz attenuation coefficient between the 3 sample sets.

Within the context of these 3 sample sets, there does not appear to be a correlation between the measured bulk density of a tile and the average strength of a flexure bar machined from this tile. A least squares regression analysis of the bulk density and average strength values resulted in a correlation factor of $R^2 = 0.06$. The fracture of a bend bar depends upon the presence of a single strength-limiting feature, such as an inclusion or compaction relic, in the primary loading zone of the flexure test. A single strength-limiting feature within the volume attributed to each flexure bar is unlikely to alter the measured density of the tile.

5.13 References

1. Demirbas MV, Haber RA. Microstructural property relationship in silicon carbide armor ceramic. [thesis]. [New Brunswick (NJ)]: Rutgers University; 2008.

2. Demirbas MV, Haber RA. Defining microstructual tolerance limits of defects for SiC armor. Ceramic Armor and Armor Systems II. Ceramic Transactions. 2005;178:109–122.

3. Demirbas MV, Haber RA. Microstructure-property relationship for armor materials. Presented at the 30th International Conference on Advanced Ceramics and Composites; 2005, Coca Beach, FL.

4. Demirbas MV, Haber RA, Brennan RE. Spatial distribution of defects in silicon carbide and its correlation with localized property measurements. Presented at the 32nd International Conference on Advanced Composites; 2007, Daytona Beach, FL.

5. Portune AR. Nondestructive ultrasonic characterization of armor grade silicon carbide [Dissertation]. [New Brunswick (NJ)]: Rutgers University; 2010.

6. Brennan R, Haber R, Niesz D, Sigel G, McCauley J. Elastic property mapping using ultrasonic imaging. Ceramic Engineering and Science Proceedings. 2008;28(5):213–222.

7. Bottiglieri S, Haber RA. Corrective techniques for the ultrasonic nondestructive evaluation of ceramic materials. Advances in Ceramics Armor VI: Ceramic Engineering and Science Proceedings. 2010;31:57–67.

8. Krautkramer J, Krautkramer H. Ultrasonic testing of materials. Berlin: Springer-Verlag; 1990; fourth fully revised edition.

9. Portune AR, Bottiglieri S, Niesz D, Haber RA. Non-destructive evaluation of armor grade ceramics. Aberdeen (MD): Army Research Laboratory (US); Annual Program Plan Review; 2008 Nov.

10. ASTM C1161. Standard test method for flexural strength of advanced ceramics at ambient temperature. West Conshohocken (PA): ASTM International; 2001.

11. Quinn GD. Guide to practice for fractography of ceramics and glasses. Washington (DC): Government Printing Office (US); 2007. p. 5–7. NIST Special Publication No.: SP 960-16.

12. Stobierski L, Gubernat A. Sintering of silicon carbide I. effect of carbon. Ceramics International. 2003;29:287–292.

13. Bakas MP. Analysis of inclusion distributions in silicon carbide armor ceramics [Dissertation]. [New Brunswick (NJ)]: Rutgers University; 2006.

6. Task 5: Nondestructive Ultrasound Characterization (NDC) of High-Density, High-Hardness Ceramics: MoD Mod-Shared with the Ceramic, Composite and Optical Materials Center (CCOMC)

Primary Investigator: RA Haber, Rutgers University

Researcher: V DeLucca

6.1 Long-Range Goals

The primary objective of this research is to use nondestructive ultrasonic testing in armor ceramic materials to characterize bulk properties, understand microstructural parameters, and predict material performance. Ultrasound nondestructive evaluation (NDE) is used to image homogeneity variations and locate anomalous defects within dense materials. Examination of these materials includes analysis of their frequency-dependant acoustic attenuation, elastic properties, and acoustic velocities. Ultrasound nondestructive characterization (NDC) makes use of frequency-dependent attenuation to measure microstructural compositions, concentrations, and size distributions.

The long-range goals of this work are to form quantitative links between ultrasonic data, microstructural constituents, and material performance. Correlations between microstructural properties such as average grain size and volumetric hardness with ultrasonic response will also be investigated. Methods for determining the size and number of inhomogeneous inclusions within the sample bulk will be developed using frequency-dependant attenuation behavior. Mechanical testing and microscopy will correlate microstructural characteristics with ultrasound data in order to form a predictive model. Characterization of multiple material systems will extend conclusions and allow for broader generalizations to be made from ultrasonic nondestructive testing.

6.2 Background

NDE of materials is an improvement over destructive methods, as it leaves the sample intact and ready for application. This ensures that virtually every piece can be tested for quality assurance before use. Ultrasound has previously been shown to have the capability to detect anomalous defects in ceramic armor that could lead to reduced strength and toughness and ultimately to failure. Testing using a broad range of frequencies is critical, as different acoustic loss mechanisms such as absorption and scattering show wavelength-dependent behavior. By characterizing

the material at both high and low frequencies, it becomes possible to visualize the effect of small property variations and determine the density of minute inhomogeneous features. Such features are believed to reduce the performance of the material in its application. In structural ceramics, heterogeneities act as stress concentrators, causing failure to occur at lower than expected stresses. Both reflected peak amplitude attenuation and top to bottom surface time-of-flight measurements can be used to locate different kinds of anomalies, including density variations, inhomogeneous inclusions, and secondary phases. NDE using ultrasound allows for interaction with density variations within the sample, enabling a quantitative analysis of the effect of these inhomogeneities on the acoustic and elastic properties of the material. These in turn can be used to form an understanding of the sample's microstructure, which can be used to predict the performance of the material.

6.3 Research Results/Accomplishments

6.3.1 Equipment Upgrades: TRS Transducers, by V DeLucca

Two TRS Ceramics, Inc., single-element ultrasonic transducers, designated 1100103 and 1100105, were received at Rutgers for evaluation. Transducer 1100103 was labeled as a 10-MHz single-element PMN-PT composite transducer and transducer 1100105 was labeled as a 35-MHz single-element PMN-PT composite transducer. The central frequency, bandwidth, signal strength, and attenuation coefficient spectrum of both transducers were measured using a standard SiC sample.

The 35-MHz 1100105 transducer was used to examine our standard SiC sample, which is a 4.05-mm-thick, 50-mm-diameter circular disc of chemical vapor deposition SiC. Measurements were made using a JSR DPR500 dual pulser/receiver with a JSR RP-L2 remote pulser. The settings used are shown in Fig. 6.1.

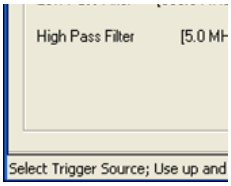

Fig. 6.1 JSR control panel settings using RP-L2 remote pulser

A screenshot showing the top surface reflection and several subsequent bottom surface reflections was taken of the digital oscilloscope view in the Legacy software used for ultrasonic measurement at Rutgers and is shown in Fig. 6.2. Included in Fig. 6.2 for comparison is a screenshot taken of another TRS 40-MHz central frequency transducer previously tested at Rutgers. Both were taken using the same 25-dB receiver gain and the same settings in the JSR control panel. The peaks seen with transducer 1100101 are much clearer than those seen in 1100105, but 1100105 appears to have slightly higher signal strength as indicated by the slightly higher bottom surface reflection peaks. Other settings were used in the JSR control panel to try to improve the quality of the signal, but they either had no effect or made it worse.

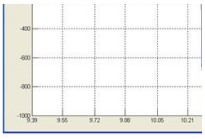

Fig. 6.2 Oscilloscope views of 1100105 (left) and 1100101 (right)

To determine the central frequency and bandwidth of the transducer, a fast Fourier transform (FFT) was taken on the top surface peak. A screenshot showing the FFT is shown in Fig. 6.3. The transducer was found to be most intense at a frequency of 31 MHz with a bandwidth of 13 MHz (–6 dB range from 24.5 to 37.5 MHz). However, some other smaller peaks were seen at lower and higher frequencies.

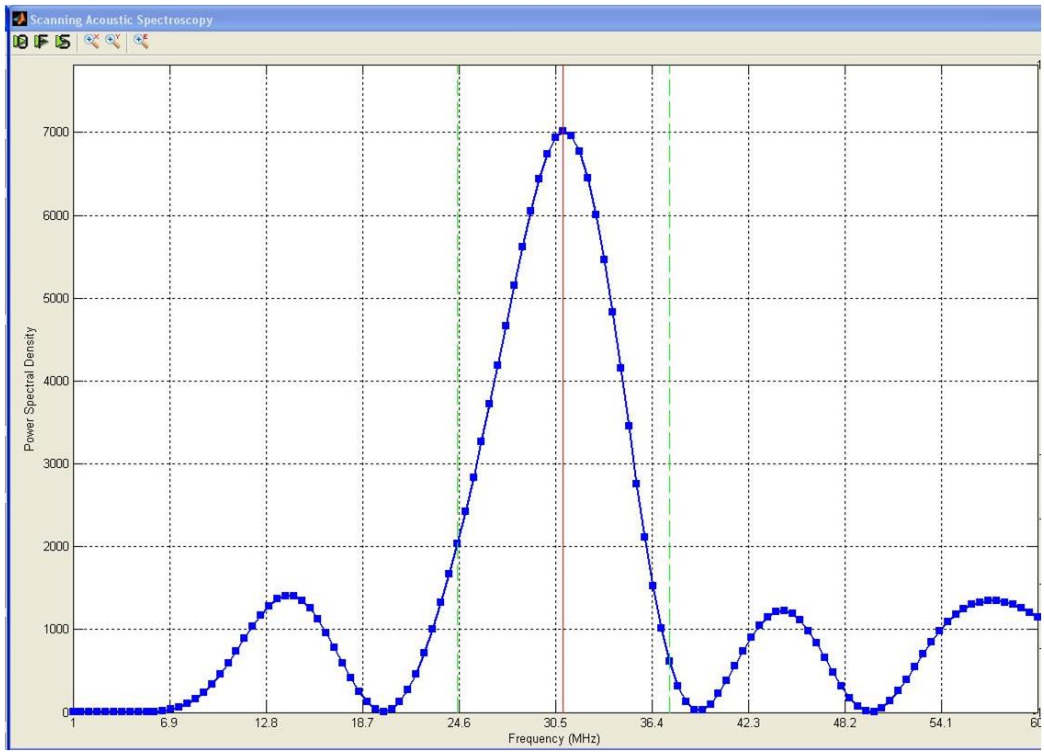

Fig. 6.3 Transducer 1100105 top surface peak FFT

Attenuation spectra measurements were not attempted with this transducer using these settings, as the width of the peaks and noise seen with transducer 1100105 make any quantitative analysis nearly impossible.

Measurements were also taken with transducer 1100105 using a JSR RP-H2 remote pulser. We typically use this remote pulser when working with higher frequency transducers with central frequency of 60 MHz or higher. The settings used are shown in Fig. 6.4.

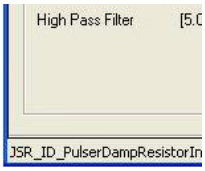

Fig. 6.4 JSR control panel settings using RP-H2 remote pulser

Figure 6.5 show a screenshot of the oscilloscope view using the RP-H2 remote pulser with transducer 1100105. The peaks seen are much clearer than those measured using the RP-L2 remote pulser but the signal strength is also much lower. There is also a considerable amount of noise seen between the peaks. An FFT taken of the top surface reflection peak was similar in apearance to the one shown in Fig. 6.3. However, the higher frequencies were attenuated so much in the bottom surface reflection peaks that only the lower frequency mode at about 15 MHz was present, making attenuation coefficient measurements in the desired frequency range impossible.

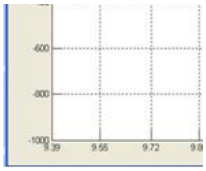

Fig. 6.5 Oscilloscope view of transducer 1100105 using RP-H2

The 10-MHz 1100103 transducer was also used to examine our standard SiC sample. For the initial testing, the high pass filter in the JSR control panel was set to 5 MHz rather than 30 MHz, and the damping was set to 330 ohms rather than 104 ohms, as these settings resulted in the strongest signal from the transducer. The signal was strong enough that the gain had to be reduced to only 10 dB to keep the bottom surface peak from saturating. A screenshot of the oscilloscope view using these settings is shown in Fig. 6.6.

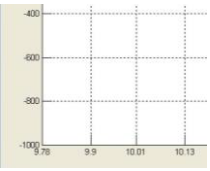

Fig. 6.6 Oscilloscope view of transducer 1100103 using 5-MHz high pass filter

To determine the central frequency and bandwidth of the transducer, an FFT was taken on the top surface peak. A screenshot of the FFT is shown in Fig. 6.7. The transducer was found to be most intense at a frequency of 32.5 MHz with a bandwidth of 22 MHz (–6 dB range from 19 to 41 MHz). There was also another smaller peak at about 8 MHz.

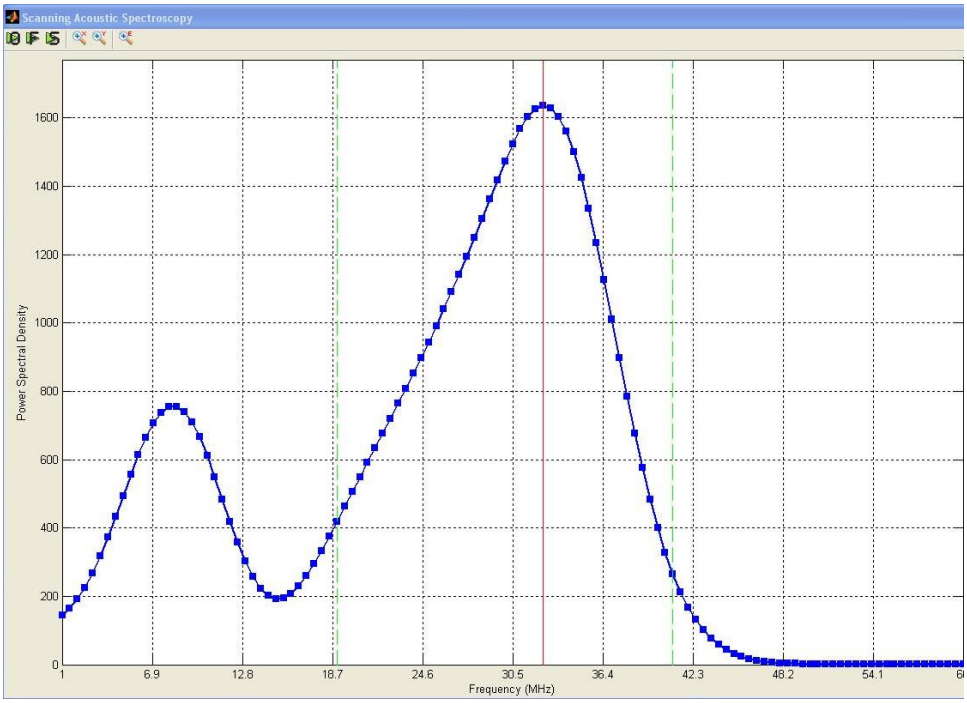

Fig. 6.7 Transducer 1100103 top surface peak FFT using 5-MHz high pass filter

Although the transducer was labeled as being a 10-MHz central frequency transducer, it was clearly much stronger at higher frequencies. To focus on the high-frequency output of 1100103, the high pass filter was raised to 30 MHz, where 44-ohm damping provided the best signal. The reciever gain also had to be increased to 22 dB. A screenshot of the oscilloscope view using these settings is shown in Fig. 6.8. Using these settings resulted in clearer, narrower peaks and significantly less noise between peaks.

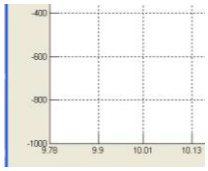

Fig. 6.8 Oscilloscope view of transducer 1100103 using 30-MHz high pass filter

An FFT of the top surface peak is shown in Fig. 6.9. As expected, the lower frequency mode is eliminated by the high pass filter. Using these settings, the transducer was found to be most intense at a frequency of 32.5 MHz with a bandwidth of 16.5 MHz (–6 dB range from 25 to 41.5 MHz).

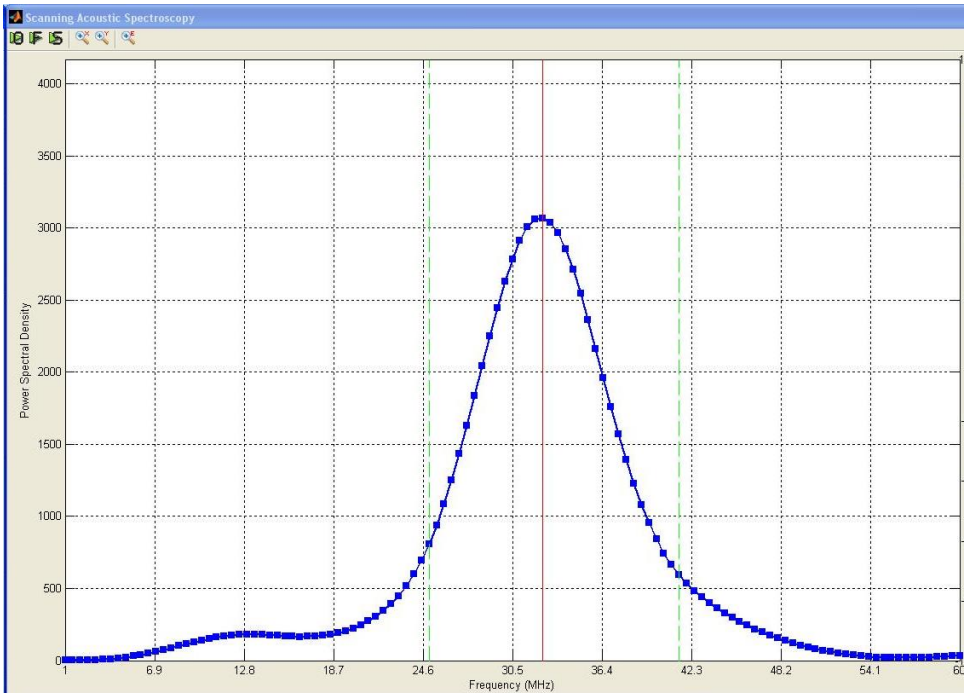

Fig. 6.9 Transducer 1100103 top surface peak FFT using 30-MHz high pass filter

A measurement of the attenuation coefficient spectrum over the center of the standard SiC sample was made using transducer 1100103 with the high pass filter set to 30 MHz. The attenuation coefficient spectrum measured with 1100103 in the range from 30 to 40 MHz is shown in blue in Fig. 6.10. Also shown for comparison are the attenuation coefficient spectra of the commercial 20- and 75-MHz transducers that are routinely used for attenuation coefficient measurements at Rutgers. The measurement made with 1100103 appears to show the same behavior as the other transducers but with a much higher attenuation coefficient. The pink line shows the attenuation coefficient measured with 1100103 reduced by 8.3 dB/cm at all frequencies. This adjusted curve fits quite well the expected behavior in this frequency range. It is possible that there is some correction factor (perhaps involving the geometry or materials used in the construction of the transducer) that would justify this adjustment, but more work would need to be done to derive it.

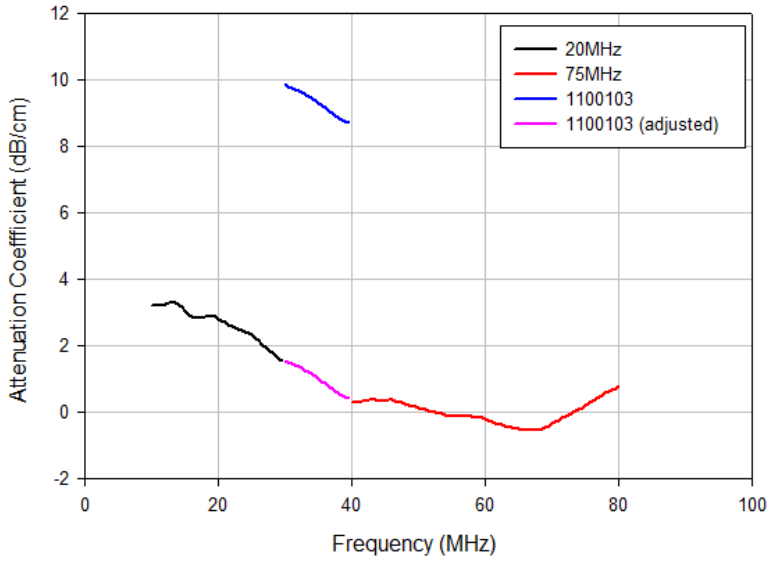

Fig. 6.10 Attenuation spectra for standard SiC sample

After contacting the transducer manufacturer, transducer 1100105 was sent back to determine if the poor performance was caused by damage that may have occurred during shipment. It was then revealed that the transducers had been mislabeled and that transducer 1100105 had the 10-MHz central frequency and 1100103 had the 35-MHz central frequency. This explained the poor high-frequency performance of 1100105 and the better high-frequency performance of 1100103. Because 1100103 behaves very well in the 30- to 40-MHz range, it may be useful if we can find a justifiable correction factor for the attenuation spectra. Another issue with the 2 transducers is that the faces are quite large. Transducer 1100105 has a 19-mm-diameter face and 1100103 has a 12-mm-diameter face. For larger specimens this is not a problem, but for smaller specimens the beam may be larger than the actual sample, which could result in signal degradation.

6.3.2 Custom Engineered SiC: Varying B_4C Additive Size and Morphology, by V DeLucca

To study the effects of BB_4C additive size and morphology on SiC prepared using spark plasma sintering (SPS), a set of 8 samples were made using 4 different B_4C powders. These powders are commercially available in a wide variety of sizes over a range of prices, but due to the nature of the processing methods used to make them, they often consist of sharp, irregularly shaped fragments. They can also be synthesized as small, equiaxed crystallites by using a rapid carbothermal reduction process as is now being done at Rutgers. The samples made were examined using ultrasound nondestructive evaluation (NDE) techniques to determine elastic properties and attempt to predict microstructural features. Both conventional

ultrasound NDE methods and ultrasound acoustic spectroscopy methods were used. Field emission scanning electron microscopy (FESEM) imaging was also conducted on polished surfaces, etched samples, and fracture surfaces to characterize the sample microstructures. By comparing the NDE predictions with the FESEM observations, the relationship between B_4C additive size and morphology and SiC microstructure and properties was examined.

To study the effect of differences in the B_4C additive size and morphology on SPS SiC, several different B_4C powders were used as additives. These included 3 commercial powders, ESK Tetrabor 3000F, ESK Tetrabor 1250 mesh, and H.C. Starck HD20, as well as a powder produced at Rutgers by rapid carbothermal reduction designated SF5. The ESK Tetrabor 1250 mesh had the largest particle size (d50: ~6 µm) followed by the ESK Tetrabor 3000F (d50: ~1 µm), Rutgers SF5 (d50: 0.59 µm), and the H.C. Starck HD20 (d50: 0.3–0.6 µm). The particle size of the commercial powders are as specified by the manufacturers. The particle size of the Rutgers SF5 powder was determined using a Malvern Mastersizer 2000. The morphology of the commercial powders tended to be sharp, irregularly shaped fragments while the Rutgers powder consisted of equiaxed, faceted particles. FESEM images of the B_4C powders used are shown in Fig. 6.11.

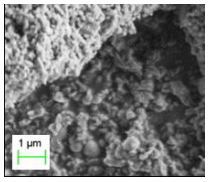

Fig. 6.11 FESEM images of B_4C powders: (A) ESK Tetrabor 1250 Mesh, (B) ESK Tetrabor 3000F, (C) H.C. Starck HD20, and (D) Rutgers SF5; scale bar is 1 µm

The 8 SiC samples were made using B_4C and C additives. The samples were made using H.C. Starck UF-25 alpha SiC powder, one of the B_4C powders, and Fisher lampblack as a C source. Each sample was made with 1.5-wt% C and 0.5- or 1.0-wt% B_4C, as shown in Table 6.1. The samples were prepared by mixing the powders in a Nalgene bottle with 3-mm SiC ball-mill media and ethanol for 3 h. The samples were then sieved to remove the media, heated to boil off the excess ethanol, and dried in an oven at 100 °C overnight.

Table 6.1 Sample compositions

Sample	B_4C additive	B_4C (wt%)	C (wt%)
1a	ESK Tetrabor 3000F	0.5	1.5
1b	ESK Tetrabor 3000F	1.0	1.5
2a	ESK Tetrabor 1250 mesh	0.5	1.5
2b	ESK Tetrabor 1250 mesh	1.0	1.5
3a	H.C. Starck HD20	0.5	1.5
3b	H.C. Starck HD20	1.0	1.5
4a	Rutgers SF5	0.5	1.5
4b	Rutgers SF5	1.0	1.5

The samples were sintered using a Thermal Technology Model SPS 10-4 SPS unit. Five grams of each sample powder were loaded into a 20-mm-inner-diameter graphite die lined with graphite foil. The samples were sintered in an argon atmosphere by first applying 5 MPa of uniaxial pressure to ensure a good conductive path through the sample. The samples were then heated at 200 °C/min to 1,400 °C while pressure was increased to 50 MPa. After holding for 1 min, the samples were again heated at 200 °C/min to 1,850 °C. After holding for 5 min at this temperature, the samples were heated at 200 °C/min to 1,950 °C. After 13 min at this temperature, the unit was shut off and the samples were allowed to cool to ambient temperature. The temperatures were measured using an optical pyrometer aimed at a small hole bored halfway through the wall of the graphite die.

After sintering, the samples were removed from the graphite die and sand-blasted to remove any residual graphite from the surfaces, and the faces were ground flat using a 125-µm diamond-embedded pad. The resulting samples were small disks approximately 20 mm in diameter and approximately 5 mm thick. The density of each sample was then measured using the Archimedes method. The density of each sample is shown with other elastic properties in Table 6.2. Immersion-based ultrasonic testing was performed on each sample using an Olympus 20-MHz planar transducer and an Ultran 75-MHz planar transducer in water. The ultrasound tests were performed in pulse/echo configuration, where the same transducer both emits

and receives the ultrasound energy. For each of the samples, a point measurement was taken over the center of the sample. Measurements to determine the elastic properties were taken using the 20-MHz transducer.

Table 6.2 Elastic properties

Sample	c_L (m/s)	c_S (m/s)	Poisson	Density (g/cc)	E (GPa)	G (GPa)	K (GPa)
1a	12,293	7,496	0.20	3.20	433	180	244
1b	12,211	7,484	0.20	3.19	429	179	237
2a	12,324	7,475	0.21	3.20	432	179	248
2b	11,974	7,376	0.19	3.19	415	174	226
3a	12,184	7,590	0.18	3.20	436	184	229
3b	12,384	7,471	0.21	3.20	434	179	253
4a	12,295	7,478	0.21	3.20	432	179	245
4b	12,270	7,443	0.21	3.20	429	177	245

The values measured for these samples are comparable to commercially sintered SiC materials with B_4C and C additions. While there is some variation in elastic property values between the samples, there is no clear relationship between the type of B_4C additive and the measured elastic properties.

Ultrasonic testing was also conducted to measure the frequency-dependent acoustic attenuation coefficient using both the 20- and 75-MHz transducers. The 10- to 80-MHz attenuation spectra for each sample are shown in Fig. 6.12. At lower frequencies measured, the primary attenuation mechanism is expected to be thermoelastic absorption by secondary phase particles, while at higher frequencies the primary attenuation mechanism is expected to be scattering by the SiC grains. Thermoelastic absorption attenuation is expected to show peak-like behavior where the peak frequency is determined by the size and thermal properties of the absorbing particles. Scattering attenuation is expected to show power law behavior based on the size of the scattering particle and the frequency.

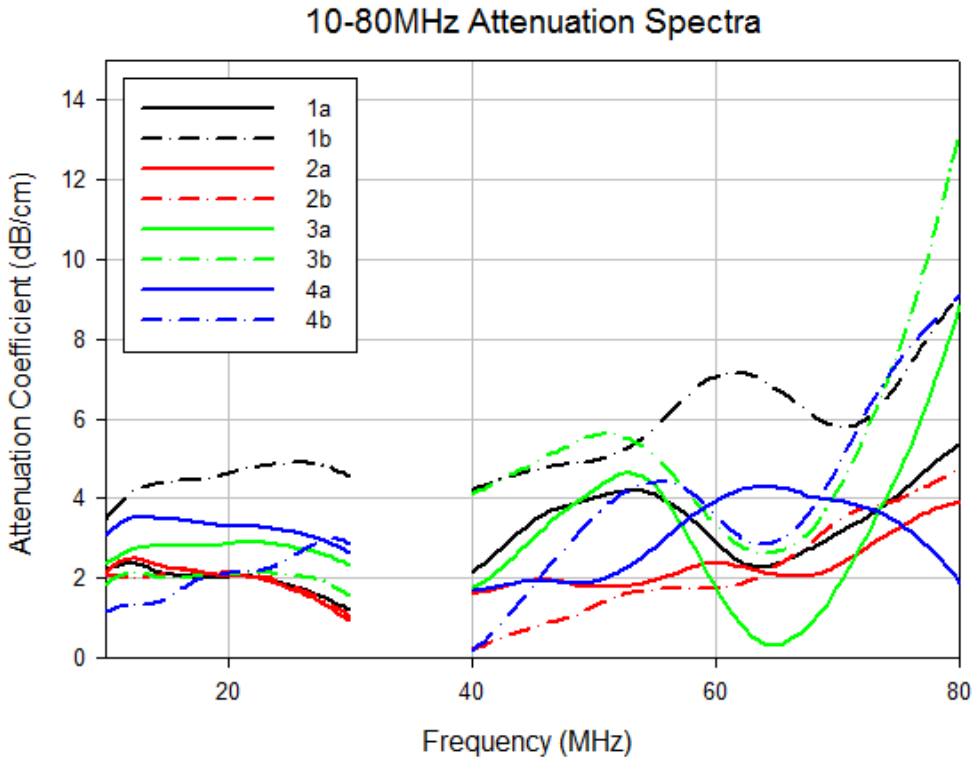

Fig. 6.12 Attenuation spectra, 10–80 MHz

In each of the samples, the attenuation spectra are relatively flat and show no clear peaks at lower frequencies. This could be indicative of a broad inclusion size distribution or that the inclusions are too large or too small to show peaks in the measured frequency range. The spectra also show anomalous behavior at higher frequencies, deviating from simple power law behavior. This could be indicative of nonuniform grain size distributions or could be caused by surface effects due to surface roughness or nonparallel sample faces. Because of this anomalous behavior, quantitative estimates of inclusion and grain size could not be made. Both the absorption and scattering theories assume that the interrogated particles are spherical. Subsequent FESEM examination showed that these assumptions are not valid in these samples and may explain the anomalous behavior seen in the attenuation spectra.

After the ultrasound measurements were taken, the samples were prepared for FESEM imaging. The samples were sectioned using a diamond saw into several pieces. Two pieces from the center of each sample were mounted in thermoset resin and polished to a 0.25-μm finish. One polished piece from each sample was etched in boiling Murakami's reagent (22 g NaOH and 16 g $K_3Fe(CN)_6$ in 120 mL H_2O) for 15 min. Unpolished pieces from each sample were broken to view the fracture surface.

FESEM micrographs of the polished sections of each sample are shown in Fig. 6.13. All of the samples are almost fully dense with little if any visible porosity. The size of the secondary phase inclusions is fairly consistent between samples, even with the different starting sizes of the B_4C additives. When the amount of B_4C additive is increased from 0.5% in set “a” (left column) to 1.0% in set “b” (right column), the number and size of secondary phase inclusions increase but still remain fairly consistent between samples within set “b”.

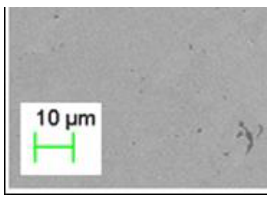

Fig. 6.13 FESEM images of polished sample surfaces

FESEM micrographs of the etched sections of each sample are shown in Fig. 6.14. All of the samples show large, elongated SiC grains. Samples 2a and 2b, which were made with the largest B_4C additive, show smaller average grain size and fewer very large grains than the other samples. As the amount of B_4C additive is increased from set a to set b, the average grain size also increases.

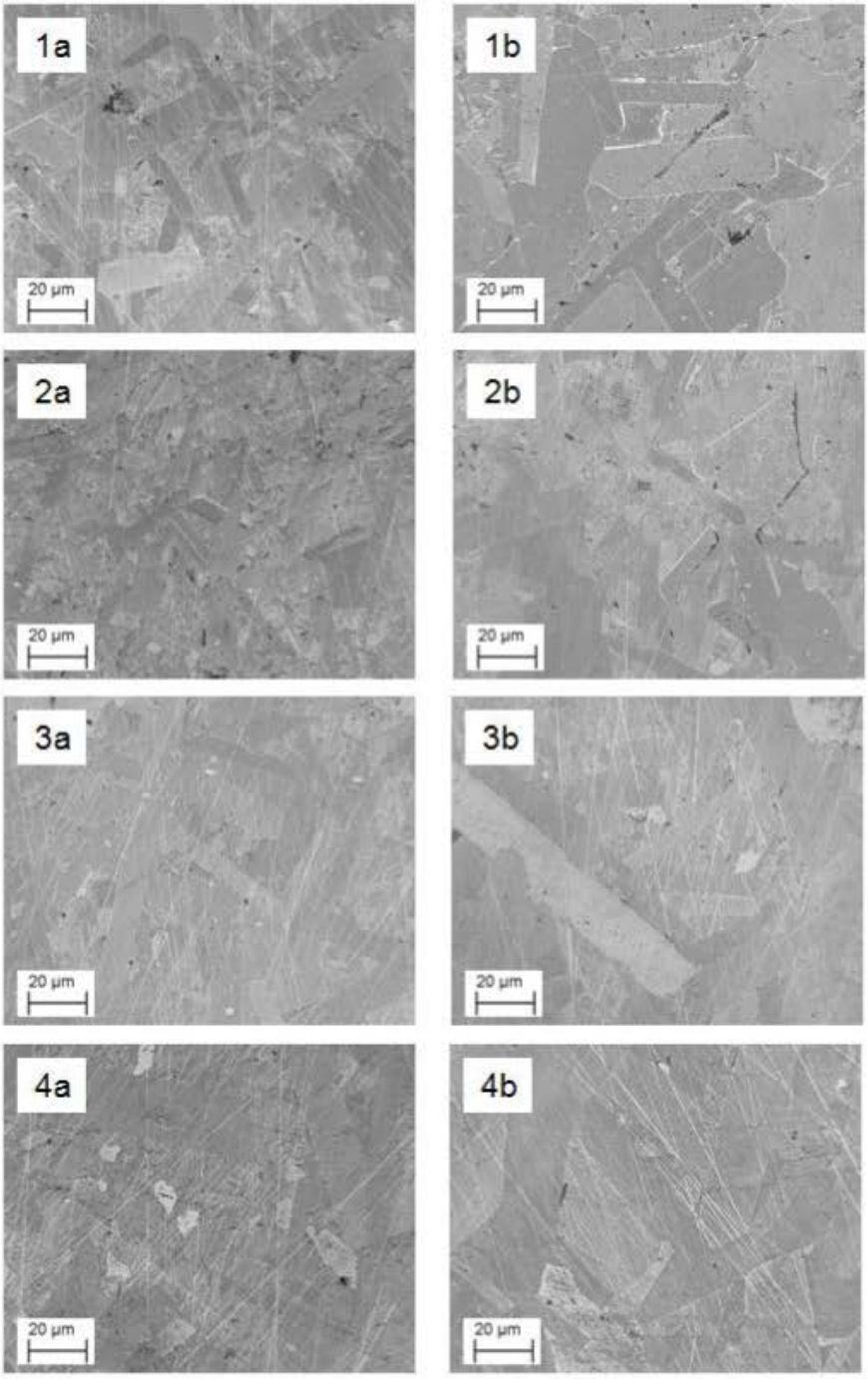

Fig. 6.14 FESEM images of etched samples

FESEM micrographs of the fracture surface for each sample are shown in Fig. 6.15. In all cases, the samples exhibit mainly intergranular fracture. Each of the fracture surfaces shows a number of large flat regions that are indicative of the large grains in the samples.

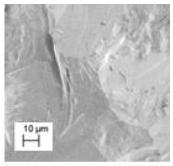

Fig. 6.15 FESEM images of sample fracture surfaces

FESEM imaging showed predominantly large high-aspect-ratio grains and irregularly shaped secondary phase inclusions that are likely the cause of the anomalous behavior seen in the attenuation coefficient spectra. From the FESEM

imaging, it appears that the size of the B_4C additives has an effect on the SiC grain size, with the larger additives reducing the average grain size. The samples made with larger additive particles (2a and 2b) appear to have smaller average grain size than those made with smaller additive particles (3 and 4). The morphology of the additives does not appear to have a noticeable effect on the microstructure at the scale investigated in this study. One direction in which this work could be taken in the future would be to adjust the sintering cycle such that the SiC grains remain small and equiaxed. This would validate the assumption of spherical particles and allow a quantitative evaluation of the microstructure using ultrasound techniques.

6.3.3 Custom Engineered SiC: Varying Processing Methodology, by V DeLucca

In addition to studying the effect of different additives on SPS SiC microstructure, SiC samples were made to examine the effect of different processing methods on the microstructure and properties. As with the previous study, both conventional ultrasound methods and acoustic spectroscopy techniques were used nondestructively characterize the materials. FESEM was also used to characterize the microstructure, and observations using the different methods were compared.

A number of different processing methods were used to make this sample set including dry mixing of powders, wet mixing of powders, ball milling, and filter pressing. For the dry-mixed samples, the starting powders used were H.C. Starck UF-25 SiC, 0.5-wt% ESK Tetrabor 3000F B_4C, and 1.0-wt% Fisher lampblack as a C source. The powders were dry mixed in a SpectroMill for 5 min in a polystyrene container. For the wet-mixed samples, the starting powders used were H.C. Starck UF-25 SiC, 0.5-wt% ESK Tetrabor 3000F B_4C, and 1.5-wt% Cabot Cab-O-Jet 200, a modified aqueous C black dispersion, as a C source. The powders were mixed in water and pan dried. For the ball-milled samples, the starting powders used were H.C. Starck UF-25 SiC, 0.5-wt% ESK Tetrabor 3000F B_4C, and 1.5-wt% Fisher lampblack as a C source. The powders were ball milled in ethanol with SiC ball-mill media for 3 h and pan dried. For the filter-pressed samples, the starting powders used were H.C. Starck UF-25 SiC, 0.5-wt% Rutgers SF5 B_4C, and 1.5-wt% Fisher lampblack as a C source. The powders were ball milled in ethanol with SiC ball-mill media for 24 h and filter pressed at 15 psi to remove the excess ethanol and form a green body to be sintered. All samples were dried in an oven at 100 °C prior to sintering. The compositions and processing methods for each sample are shown in Table 6.3.

Table 6.3 Sample compositions

Sample	B_4C additive	B_4C (wt%)	C additive	C (wt%)	Processing
Mark I	ESK Tetrabor 3000F	0.5	Lampblack	1.0	Dry mixed
Mark 1.5a	ESK Tetrabor 3000F	0.5	Lampblack	1.5	Ball milled
Mark 1.5b	ESK Tetrabor 3000F	0.5	Cab-O-Jet 200	1.5	Wet mixed
Mark II	Rutgers SF5	0.5	Lampblack	1.5	Filter pressed

The samples were then densified in a Thermal Technology SPS 10-4 SPS unit in argon atmosphere using a graphite die lined with graphite foil. The samples were sintered by first heating to 1,400 °C under 50-MPa uniaxial pressure and holding for 30 min. The system was then allowed to cool for 30 min while still under 50-MPa pressure. The sample was then heated to 2,000 °C under 50-MPa pressure and held for 15 min. The temperature was determined by an optical pyrometer aimed at a hole drilled into the side of the graphite die. After the sintering cycle was complete, the pressure was released, the system was allowed to cool, and the samples were removed.

After densification, the samples were sand-blasted to remove the graphite foil and the faces were ground flat using a 125-μm diamond polishing wheel. The samples are approximately 20 mm in diameter and 5- to 7-mm thick. The densities of the samples were determined using the Archimedes method. The samples were then examined using nondestructive ultrasound techniques to measure elastic properties and collect attenuation coefficient spectra using 20- and 75-MHz central frequency transducers. The densities and elastic properties of the samples are shown in Table 6.4. The properties listed for the Mark I and Mark II samples are averaged over 3 samples.

Table 6.4 Elastic properties

Sample	c_L (m/s)	c_S (m/s)	Poisson	Density (g/cm^3)	E (GPa)	G (GPa)	K (GPa)
Mark I	12,107	7,511	0.187	3.20	429	181	229
Mark 1.5a	11,980	7,420	0.189	3.19	418	176	224
Mark 1.5b	12,120	7,500	0.189	3.19	427	179	229
Mark II	12,069	7,477	0.188	3.19	425	179	227

Fig. 6.16 shows the attenuation coefficient spectrum for samples from each set in the 10- to 80-MHz range. The samples all exhibit very similar behavior in the 10- to 30-MHz range, showing a fairly flat spectrum with no clear peaks. At higher frequencies, the samples also show similar behavior, generally showing power law behavior but with a peak or shoulder at around 55 MHz. This could be indicative of a nonuniform grain size distribution or caused by surface effects. As with the previous SiC samples, quantitative estimates of inclusion and grain size could not

be made, as both the absorption and scattering theories assume that the interrogated particles are spherical. Subsequent FESEM examination again showed that these assumptions are not valid.

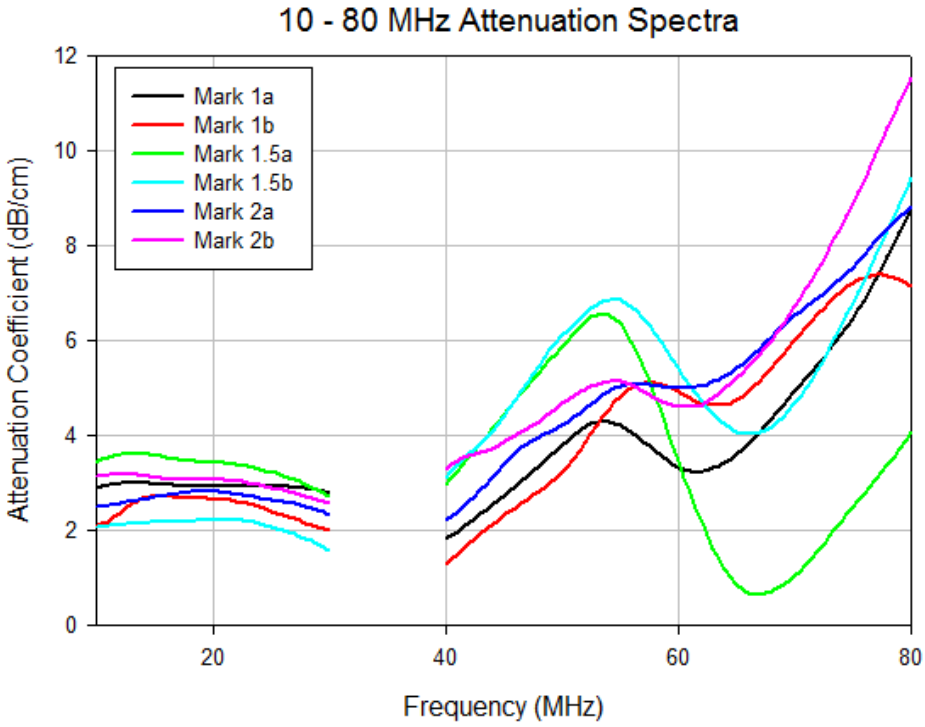

Fig. 6.16 Attenuation spectra, 10–80 MHz

After ultrasonic evaluation, the samples were sectioned and polished to a 0.25-µm finish for FESEM imaging. A polished piece from each sample was etched in boiling Murakami's reagent (22 g NaOH and 16 g $K_3Fe(CN)_6$ in 120 mL H_2O) and unpolished pieces from each sample were broken to view the fracture surfaces.

FESEM images of a representative sample of each of Mark I and Mark II are shown in Fig. 6.17, and both appear to have a bimodal grain size distribution with both small grains less than 10 µm in length as well as large grains that are several tens of microns long. The grains also tend to be elongated with a high aspect ratio. However, the Mark I sample has mainly smaller grains with few large grains while the larger grains are more predominant in the Mark II sample. The fracture surfaces of both the Mark I and II samples show predominantly transgranular fracture.

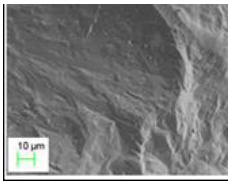

Fig. 6.17 FESEM images of etched surfaces of Mark I (A) and Mark II (B) and fracture surfaces of Mark I (C) and Mark II (D)

6.4 Creation of Custom-Engineered SiC Samples

In the work previously described, SiC samples were made to study the effects of different additives and processing methods and their effects on the acoustic properties of the material. However, the samples that were produced tended to have large, nonspherical grains and irregularly shaped second phase inclusions. Because of the assumption of spherical particles in the determination of attenuation caused by both the thermoelastic absorption and scattering mechanisms, the samples produced were not well suited for this type of analysis. To facilitate further investigation of the attenuation mechanisms in the SiC-B_4C-C system, samples should be made with more equiaxed grains and a better-controlled distribution of secondary phase inclusions. The first step in accomplishing this would be adjusting the sintering cycles used. By adjusting the sintering parameters, the grain size and shape can be controlled to provide a more uniform grain size distribution with more equiaxed grains so that the assumption of spherical particles is more valid. Samples made in this way could be used as standards with which to compare other SiC materials to estimate grain and secondary phase size distributions.

6.5 New Transducer Integration

With the 20- and 75-MHz central frequency transducers currently used for ultrasonic evaluation of ceramic materials, there is a "gap" in the 30- to 40-MHz frequency range that is not covered by these transducers. While a new transducer was obtained that covers this frequency range, the spectra obtained shows somewhat different behavior compared with those obtained by the transducers currently used. To integrate this transducer, work must be done to find some correction factor that would be physically justified to bring the attenuation values obtained from the new transducer in line with the others. There should also be efforts to integrate lower frequency transducers into the existing ultrasound system since they would be able to interrogate a larger size range of secondary phase inclusions through the thermoelastic absorption mechanism.

1 (PDF) DEFENSE TECHNICAL INFORMATION CTR DTIC OCA

2 (PDF) DIRECTOR US ARMY RESEARCH LAB RDRL CIO LL IMAL HRA MAIL & RECORDS MGMT

1 (PDF) GOVT PRINTG OFC A MALHOTRA

1 (PDF) DIR USARL RDRL WM J MCCAULEY

46 (7 HC, 39 PDF) DIR USARL
RDRL CIH C
D GROVE
J KNAP
RDRL WM
P BAKER
B FORCH
J MCCAULEY (6 HC)
P PLOSTINS
RDRL WML B
I BATYREV
B RICE
D TAYLOR
N WEINGARTEN
RDRL WML H
B SCHUSTER
RDRL WMM
J BEATTY
R DOWDING
J ZABINSKI
RDRL WMM B
G GAZONAS
RDRL WMM E
S KILCZEWSKI
J LASALVIA
P PATEL
J SINGH
J SWAB
RDRL WMP
S SCHOENFELD
RDRL WMP A
S BILYK
RDRL WMP B
C HOPPEL
S SATAPATHY
M SCHEIDLER
T WEERASOORIYA
RDRL WMP C
R BECKER
T BJERKE
D CASEM
J CLAYTON (1 HC)
D DANDEKAR
M GREENFIELD
R LEAVY
S SEGLETES
C WILLIAMS
RDRL WMP D
R DONEY
RDRL WMP E
S BARTUS
RDRL WMP F
N GNIAZDOWSKI
RDRL WMS
M VANLANDINGHAM

INTENTIONALLY LEFT BLANK.